This is to certify that the
dissertation entitled

NOVEL TRIBOLOGICAL SYSTEMS USING SHAPE-MEMORY ALLOYS AND THIN FILMS

presented by

YIJUN ZHANG

has been accepted towards fulfillment
of the requirements for the

Ph.D degree in Materials Science and Engineering

Major Professor's Signature

11/7/06

Date

MSU is an Affirmative Action/Equal Opportunity Institution

MICHIGAN STATE UNIVERSITY

NOVEL TRIBOLOGICAL SYSTEMS USING SHAPE-MEMORY ALLOYS AND THIN FILMS

By

Yijun Zhang

A DISSERTATION

Submitted to
Michigan State University
in partial fulfillment of the requirements
for the degree of

DOCTOR OF PHILOSOPHY

Department of Chemical Engineering and Materials Science

2006

ABSTRACT

NOVEL TRIBOLOGICAL SYSTEMS USING SHAPE-MEMORY ALLOYS AND THIN FILMS

By

Yijun Zhang

Shape memory alloys and thin films are shown to have robust indentation-induced shape memory and superelastic effects. Loading conditions that are similar to indentations are very common in tribological systems. Therefore novel tribological systems that have better wear resistance and stronger coating to substrate adhesion can be engineered using indentation-induced shape memory and superelastic effects.

By incorporating superelastic NiTi thin films as interlayers between chromium nitride (CrN) and diamond-like carbon (DLC) hard coatings and aluminum substrates, it is shown that the superelasticity can improve tribological performance and increase interfacial adhesion. The NiTi interlayers were sputter deposited onto 6061 T6 aluminum and M2 steel substrates. CrN and DLC coatings were deposited by unbalanced magnetron sputter deposition. Temperature scanning X-ray diffraction and nanoindentation were used to characterize NiTi interlayers. Temperature scanning wear and scratch tests showed that superelastic NiTi interlayers improved tribological performance on aluminum substrates significantly.

The two-way shape memory effect under contact loading conditions is demonstrated for the first time, which could be used to make novel tribological systems. Spherical

for the first time, which could be used to make novel tribological systems. Spherical indents in NiTi shape memory alloys and thin films had reversible depth changes that were driven by temperature cycling, after thermomechanical cycling, or one-cycle slip-plasticity deformation training. Reversible surface topography was realized after the indents were planarized. Micro- and nano- scale circular surface protrusions arose from planarized spherical indents in bulk and thin film NiTi alloy; line surface protrusions appeared from planarized scratch tracks. Functional surfaces with reversible surface topography can potentially result in novel tribological systems with reversible friction coefficient.

A three dimensional constitutive model was developed to describe shape memory effects with slip-plasticity. After implementing the model in a commercial finite element program (ABAQUS), spherical indentation-induced superelasticity in NiTi was simulated and the results were compared to the results of experiments, including measurement of load-displacement curves and recovery ratios. Shallow indents were shown to have complete recovery upon unloading; deep indents had partial recovery. Stress-strain distributions, and the extent of the indentation-induced phase transformation region were also analyzed.

Acknowledgement

I am much obliged to Prof. David.S.Grummon at Michigan State University and Dr. Yang-Tse Cheng at General Motors Corp. for their advice, help, encouragement and inspiration in the art and practice of scientific research, which are truly invaluable to me. It would have been impossible for me to complete even a minute piece of this work without their support.

I give sincere appreciation to my committee members: Dr. Carl Boehlert, Dr. Martin A. Crimp, Dr. John Shaw and Dr. Thomas Pence for their teachings, expertise, suggestions and generous help.

I am also grateful for the help received from : Anita Weiner, Mike Luktich, Erkan Konca, Jihui Yang, and Yue Qi at General Motors Corp.; Dr. Thomas R. Bieler, Dr. Yuchen Lan, Hairong Jiang, Fei Ren, John Foltz, Kebin Low, and Jiaming Zhang at Michigan State University

Table of Contents

List of Tables

List of Figures

Images in this dissertation are presented in color.

Chapter 1

Introduction

Shape memory alloys and thin films have been shown to have robust indentation-induced shape memory effect and superelasticity. Experimental and theoretical work was undertaken to explore potential novel tribological systems utilizing indentation-induced superelasticity and shape memory effects:

(1) Using superelastic NiTi thin films as interlayers between hard coatings and soft substrates as a method to enhance tribological performance of hard coatings/soft substrates systems;

(2) Demonstration of the indentation-induced two-way shape memory effect, which can lead to future tribological systems with friction coefficient that changes with temperature.

(3) Finite element modeling of spherical indentation on superelastic NiTi alloy to understand stress-strain and phase transformation evolution in indentation-induced superelasticity.

Wear of machine components made from the lightweight alloys such as aluminum and magnesium is an important issue in the automobile and aerospace industries. The past two decades have seen rapid development of hard coatings produced by various physical and chemical vapor deposition methods. The successful application of hard

coatings to hard substrates like machine tools and cast dies has stimulated research efforts towards deploying hard coatings on soft metal substrates. However, one of the most difficult obstacles is that soft substrates are prone to plastic deformation before the failure of the hard coating. The following question is addressed: What is the best 'foundation' (interlayer) to support a stiff, hard, wear resistant coating for substrate materials that have arbitrarily poor elastic-plastic support characteristics and a high CTE mismatch? Such an interlayer must be capable of shielding the substrate from plastic damage while accommodating large displacements in the hard coating, all without allowing cyclic damage accumulation (fatigue failure) in either the interlayer or the substrate. This interlayer must also manage thermal mismatch strains to allow use of thicker coatings to limit σ_x (the stress component parallel to the coating surface). What is needed is an elastically compliant material with very high effective resilience - one in which fully reversible strains beyond 1-2% can occur at moderate stress without causing unacceptable lattice damage. An interlayer with such properties must be made sufficiently thick to disperse the strain field associated with contact loading, to a degree sufficient to shield the substrate material from cyclic plastic strain.

A superelastic NiTi interlayer can potentially meet the above requirements. Preliminary studies have shown that a superelastic NiTi interlayer can improve tribological performance [*1-3*], but there is no systematic information on how the evolution of martensite-austenite phase transformations affects tribological performance. This knowledge can only be obtained from wear and scratch tests carried out over the

complete transformation temperature range. Another key problem is how the coating:interlayer thickness ratio affects tribological performance. The residual stresses in a CrN coating and a NiTi interlayer interact with each other, and also with the contact stress during tribological testing. Residual stresses also increase with coating and interlayer thickness. Detailed knowledge of this problem can be obtained from tribological tests over a matrix of coating:interlayer thickness ratios and over a temperature range that covers the phase transformation temperatures.

The two-way shape memory effect (TWSME) under contact loading conditions, which can be utilized to make novel tribological systems, has been demonstrated for the first time in this work. Spherical indents in NiTi shape memory alloys and thin films, after thermomechanical cycling or one-cycle slip-plasticity deformation training, displayed a reversible depth change that was driven by temperature cycling.

Polymer thin films that exhibit photonic-controlled reversible surface relief gratings can be utilized in optical data storage and diffractive optical elements. Metals with similar ability can find optical and mechanical applications for their greater load bearing ability and often better durability than polymers. This idea has been realized in a NiTi SMA by indentation-induced two-way shape memory effect. Micro and nano scale circular surface protrusions arose from planarized spherical indents in bulk and thin film NiTi alloys. Line surface protrusions appeared from planarized scratch tracks. This reversible surface topography was driven by martensite↔austenite phase transformations. This interesting phenomenon raises many intriguing questions as to the basic mechanism

driving the indentation-induced two-way effect. The results point to novel applications, from self-healing of wear damage, to creation of surfaces with thermally-variable coefficient of friction. Furthermore, the ease with which large numbers of regularly spaced features can be produced by this method may lead to highly robust optically-functional surfaces, and the ability to create the effect at very small length scales may enable new kinds of high-energy actuators for micro-electro-mechanical systems.

Finite element modeling of indentation in superelastic NiTi alloy is helpful to better understand the novel tribological systems using shape memory alloys and thin films. A three-dimensional constitutive model was developed to describe shape memory effects with plasticity. After implementing the model in a commercial finite element program (ABAQUS), spherical indentation-induced superelasticity in NiTi was simulated and compared to results from experiments, including measurement of load-displacement curves and recovery ratios. Shallow indents were shown to have complete recovery upon unloading; deep indents had partial recovery. The stress-strain distribution and the extent of the indentation-induced phase transformation region were also modeled.

Chapter 2 briefly reviews recent work in the various research areas involved: shape memory alloys and thin films, superelastic effects, the two-way shape memory effect, contact mechanics, hard coatings on soft substrates, and finite element modeling.

Chapter 3 contains the details of materials and methods, including descriptions of experimental materials, equipment, and test parameters. The formulation of

three-dimensional constitutive model of shape memory material and its finite element implementation is also included in this chapter, along with the validation of the model by comparison with experimental results.

Chapter 4 discusses the experimental and computational results. The first section addresses the novel tribological systems with NiTi interlayers. The phase transformational stress in NiTi thin films on aluminum substrates, and these covered by a hard coating is strong evidence of phase transformations occur in the NiTi interlayer. Tribological test results on hard coating on aluminum and steel substrates with NiTi interlayers are presented and discussed, along with finite element modeling of the tribological systems. The second part concerns the indentation-induced two-way shape memory effect. Two-way shape memory effects from two different training methods are presented. Reversible surface topography can be realized from the two-way shape memory effect by planarization. Possible mechanisms of this two-way shape memory effect are then discussed.

Chapter 5 summarizes the dissertation and gives suggestions for future work.

Chapter 2

Literature Review

2.1 NiTi Shape Memory Alloys

2.1.1 Historical Development of Shape Memory Alloys

The discovery of thermoelastic martensite phase transformation preceded the discovery of the shape memory effect. According to Otsuka and Wayman [*4*], A. Ölander [*5*] discovered the pseudoelastic behavior of the Au-Cd alloy in 1932. Greninger & Mooradian [*6*] observed the formation and disappearance of a martensitic phase by decreasing and increasing the temperature of a Cu-Zn alloy in 1938. The first attempts to clarify the basic mechanisms of thermoelastic martensite phase transformations was made a decade later by Kurdjumov & Khandros (1949) [*7*] and also by Chang & Read [*8*].

In the early 1960s, Buehler and his co-workers at the U.S. Naval Ordnance Laboratory discovered the functionality of the thermoelastic martensite phase transformation in equiatomic NiTi and termed it "the shape memory effect", which has attracted academic and industrial interest ever since. This alloy was named Nitinol (*Nickel-Titanium Naval Ordnance Laboratory*). Intensive investigations have been made to elucidate the metallurgy and mechanics of various kinds of shape memory alloys, which also have been used in a wide range of structures for actuation purposes [*9-11*].

Due to NiTi's biocompatibility and excellent mechanical properties, shape memory alloys have recently been used to make implantable medical devices, like cardiovascular stents [*12-18*].

2.1.2 Phases in NiTi Alloy

The near-equiatomic NiTi alloy system has a high temperature parent phase (austenite phase) that transforms displacively to a daughter phase (martensite phase) at lower temperatures. The high-temperature austenite phase has a B2 CsCl type ordered structure, with lattice parameter of 0.3015nm [*19*]. The low temperature martensite phase was determined to be monoclinic B19' type lattice after a series of electron microscopy studies [*20-22*]. The ultra-fine size of NiTi martensite twins and variants made its characterization difficult. The lattice parameters are slightly different in different reports (Table 1). The austenite phase has a higher symmetry than the martensite phase.

There also exists an R-phase transformation at intermediate temperatures between austenite-martensite phase transformations, characterized by a sharp increase of electrical resistivity and a small hysteresis (1-2K). The R-phase has a trigonal P3 type lattice [*23, 24*]. It was initially considered a precursor effect, or pre-martensitic behavior, but is now established as martensitic transformation itself, which precedes the B19' martensite

transformation.

NiTiCu with Cu content above 8-10 at.% has a B19 orthorhombic type martensite with lattice parameters a_0=0.2881 nm, b_0=0.4279 nm, c_0=0.4514 nm [*25-27*]

The phase diagram for the binary NiTi system is shown in Figure 1. The 50-50 at.% NiTi matrix has almost no solubility of extra Ti at temperatures below 773K; solubility of extra Ni decreases rapidly as temperature cools below 1373K.

Various precipitate phases, Ti_3Ni_4, Ti_2Ni_3, $TiNi_3$, form under certain heat-treatment conditions. Their lattice structures are listed in Table 2. The size and distribution of the precipitates are determined by composition and heat treatment. Figure 2 shows how aging temperature and time affects the size and distribution of Ti_3Ni_4 precipitates in 51.3at%NiTi thin films. At aging temperatures around 773K to 1073K, the precipitates form by diffusion controlled phase transformations. Generally, at lower aging temperature and for a shorter aging time, Ti_3Ni_4 appears; at higher aging temperature and longer aging time, $TiNi_3$ appears; intermediate aging time and temperature, Ti_2Ni_3 appears. Prolonged aging also decomposes Ti_3Ni_4, and Ti_2Ni_3 into $TiNi_3$. These transformations are summarized in the TTT (isothermal time-temperature-transformation) diagram [*28*]. The precipitates are important to the phase transformation temperatures, mechanical properties and phase transformation characteristics.

2.1.3 The Shape Memory Effect

Thermoelastic martensite-austenite phase transformations and the unique twinning deformation mechanism of NiTi martensite phase are the two main pillars of the shape memory and superelastic effects [*29*]. "Thermoelastic" means that the martensite-austenite phase transformations are reversible with heating and cooling within a relatively narrow hysteresis, and the boundary between the austenite phase and the martensite phase is thermally reversible [*30*]. During the martensite phase transformation, each higher-symmetry austenite grain is transformed into self-accommodating lower-symmetry martensite twins with mobile twin boundaries. Subjected to external stresses, twins that align with the shear components of the external stress become energetically favorable and grow at the expenses of other twins. Finally the grain may become a single crystal of the most favorable martensite variant under stress. In this way the deformation strain is accommodated by the growth and alignment of martensite twins. Slip plasticity is not involved until this deformation mechanism is exhausted. Because of the lattice correspondence between two phases, the deformation strain is cancelled when the martensite variants are transformed back to the original austenite grains, and the shape memory alloys "remember" the original macroscopical shape.

The WLR theory is a phenomenological crystallographic theory of martensitic transformation, named after its developers Wechsler, Lieberman and Read [*31, 32*]. The deformation and rotation of a parent lattice is represented by matrices as operators, which act on an arbitrary vector. The habit plane between parent and martensite is considered

to be an invariant plane, which is undistorted and un-rotated, since the invariant plane minimizes the interfacial strain energy. This situation is shown schematically in Figure 3 for the case where the lattice invariant shear is twinning. The lattice invariant shear is an inhomogeneous shear occurring without changing the martensite structure.

The martensite plate, which consists of martensite matrix and its twin, is called the habit plane variant (h.p.v.). The twins in the martensite are the smallest scale martensite variants. Each has a specific lattice correspondence with the parent phase, which is called lattice correspondence variants. For $<01\bar{1}>$ type II twinning (a lattice invariant shear), phenomenological crystallographic calculation gives 24 h.p.v. which are shown in a stereographic projection in Figure 4.

The elastic strains associated with martensitic transformations are reduced by the invariant plain strain condition across the austenite/martensite interface. However, this condition cannot eliminate the transformation strains completely, because out-of-plane shear components are not eliminated under this condition, but if two habit plane variants with opposite shearing directions are formed side by side, the shear strains are eliminated macroscopically. The hierarchy in reducing elastic strain energy upon transformation by the combination of multiple variants is called self accommodation of martensite. The mechanism of self-accommodation in most of the β-phase alloys such as Cu–Al–Ni, Ag–Cd were successfully analyzed using phenomenological crystallographic theory [*33*]. According to the mechanism, four or two clusters of habit plane variants (h.p.v.) around

$[01\bar{1}]$ poles self-accommodate, and the averaged shape strain matrix becomes close to the identity matrix, which represents the strain free state.

2.1.4 Phase Transformation Temperatures

There are four phase transformation temperatures: M_S, M_f (martensite start and finish temperatures) and A_S, A_f (austenite start and finish temperatures). M_S and M_f are the temperatures that the martensitic phase starts to form (M_S) and completes the phase transformation (M_f), respectively. The A_S and A_f temperatures, the austenite start and finish temperatures, are defined in the same way. If M_S and M_f are close to A_S and A_f, then the shape memory alloy has a narrow phase transformation hysteresis and vice versa. One way to define hysteresis, Δ, is:

$$\Delta = \frac{A_S + A_f}{2} - \frac{M_S + M_f}{2}.$$

Transformation temperatures determine the temperature range in which shape memory effect (SME) or superelastic effect (SE) can be observed, which is important for practical applications. Experimentally it is known that the martensite transformation temperatures are strongly dependent on composition. For example, one percent change in Ni content above 50 at.% can change transformation temperature by more than 100 K. Figure 5 shows the phase transformation temperature dependency on the Ni content in NiTi alloy [*34*]. Therefore, the most effective way of obtaining desired transformation

temperature is by tuning composition.

Ternary alloying elements are added to the binary NiTi system to alter transformation temperatures. Most alloying elements lower transformation temperatures, but Pd [*35*], Pt [*36*], Zr [*37, 38*] and Hf [*39-41*] increase transformation temperatures. Pd and Hf are used in making shape memory alloys with high phase transformation temperatures. The addition of Cu changes the lattice structure of martensite from B19' to B19 when the Cu content exceeds 8-10 at.%. Compared to the B2-B19' phase transformation, the B2-B19 transformation has a narrower temperature hysteresis. The size and distribution of precipitates in the ternary NiTiX system has strong influence on mechanical properties and shape memory characteristics [*40, 42*].

Aging processes can also influence phase transformation temperatures, especially the M_S temperature, in binary NiTi alloy. The solubility of Ni in the B2 matrix is shown in the phase diagram in Figure 1. Quenching from solution temperature around 1173K can prevent excess Ni from precipitating. It enables the study of transformation temperatures vs. Ni content. Ni_4Ti_3 and other precipitates are formed in the aging treatment, which lower the Ni content in matrix and elevate *Ms* temperatures [*43-45*]. Since excess Ni can dissolve into the matrix while Ti cannot, the transformation temperatures of bulk Ti-rich NiTi are more stable [*46*].

2.2 Sputter-Deposited NiTi Thin Films

Development of NiTi thin films was driven by the prospect for microactuators in micro-electrical-mechanical system (MEMS) [*9*]. Magnetron sputter deposition, among other physical vapor deposition (PVD) methods, like evaporation and laser ablation [*47*], is the most effective method of making NiTi thin films with strong SE and SME [*48-50*]. Sputter-deposited NiTi thin films have grain size ranging from 0.5μm to several microns, almost ten times smaller than that of bulk NiTi [*51, 52*]. The fine grain sizes give good mechanical properties such as higher yield stress, which is another reason for using NiTi thin films for actuation.

2.2.1 Fabrication of NiTi Thin Films

Magnetron sputter deposition is a complex process. During the magnetron sputter deposition process, inert gas ions are accelerated by an electric field and bombard the cathode surface. Atoms of the cathode are dislodged by this energetic process and are deposited on the substrate.

Many factors influence the resulting thin films' composition, mechanical properties and SME characteristics. The most important parameters are target chemical composition, deposition power and voltage, Ar pressure, and deposition temperature. They are discussed briefly here:

(1) At steady state, deposition flux matches the target composition even though

different elements have different sputter yield, because the target surface composition is altered by the differential sputter rate. Differential sputtering only affects the growing film because it too suffers sputter ejection and doesn't reach a steady state. As a result, the sputter-deposited NiTi thin films usually have different chemical composition compared to the target composition.

(2) Deposition power determines the deposition rate of thin films. Higher deposition power gives more substrate heating and affects trapping times.

(3) Higher Ar pressure may produce thin films with a columnar structures while lower Ar pressure gives a featureless structure [*51*]. Because the kinetic energy of sputtered atoms may be reduced by collision with Ar ions and the absorbed Ar atoms may impede the diffusion of Ni and Ti atoms by reducing the kinetic energy driving surface diffusion [*51*].

(4) The deposition temperature determines whether NiTi thin films are amorphous or crystalline. The thin films are heated by the kinetic energy of deposited atoms, normally around 100K above from room temperature. Extra substrate heating is needed to elevate the temperature of thin films above around 650K so that Ni and Ti atoms have enough kinetic energy to crystallize [*50, 53*].

2.2.2 Effect of Stress on Transformation: the Clausius-Clapeyron Equation

The Clausius-Clapeyron equation is used widely to describe the pressure dependence

of the equilibrium temperature in the reversible first order phase transformation between gas-liquid, gas-solid, and solid-solid phases. Let the Gibbs free energy of phase A and B be G_A and G_B. For first order phase transformation, the Gibbs free energy is continuous but its derivative is not.

$$dG_A = dG_B, \quad \text{(eq. 2.1)}$$

$$dG = Vdp - SdT, \quad \text{(eq. 2.2)}$$

For each phase, V is the molar volume, p is the hydrostatic (tri-axial) pressure, T is the temperature and S is the entropy. Use (eq. 2.2) in (eq. 2.1) to give:

$$V_A dp - S_A dT = V_B dp - S_B dT, \text{ (eq. 2.3).}$$

If the phase transformation direction is from phase A to phase B, then

$$\begin{aligned} \Delta S_A^B &= S_B - S_A \\ \Delta V_A^B &= V_B - V_A \end{aligned}, \quad \text{(eq. 2.4)}$$

where ΔH_A^B is the enthalpy change from phase A to phase B

Rearrange (eq. 2.3) to give

$$\frac{dp}{dT_{EQ}} = \frac{\Delta S_A^B}{\Delta V_A^B}, \quad \text{(eq. 2.5)}$$

(eq. 2.5) is the basic form of the Clausius-Clapeyron equation. The dT_{EQ} is the change in the equilibrium phase transformation temperature due to the pressure. Under the conditions of constant pressure and constant temperature, and no external work except from volume change from pressure, an entropy change can be expressed in terms of an enthalpy change:

$$\Delta S_A^B = \frac{\Delta H_A^B}{T_{EQ}}, \text{ (eq. 2.6).}$$

Thus (eq .2.5) can be expressed as

$$\frac{dp}{dT_{EQ}} = \frac{\Delta H_A^B}{T_{EQ} \cdot \Delta V_A^B}, \qquad \text{(eq. 2.7).}$$

For shape memory alloys, uniaxial tension and compression are the more common loading conditions than hydrostatic pressure. The uniaxial loading also changes phase transformation temperatures. This phenomenon can be explained by a modification of the Clausius-Clapeyron equation. If the pressure is replaced by uniaxial stress:

$$dG = \varepsilon d\sigma - SdT \ , \quad \text{(eq. 2.8).}$$

(eq. 2.5) becomes

$$\frac{d\sigma}{dT_{EQ}} = \frac{\Delta S_A^B}{\Delta \varepsilon_A^B} = \frac{\Delta H_A^B}{T_{EQ} \cdot \Delta \varepsilon_A^B}, \qquad \text{(eq. 2.9)}$$

The shift of phase transformation temperatures due to external stress can be estimated for NiTi SMA. Consider uniaxially loading of a 1m× 1m× 1m NiTi sample cooled from austenite phase to martensite phase. Typical material properties are:

transformation enthalpy: $\Delta H_A^M = 20J/g$,

equilibrium temperature: $T=333K$,

density: 6.45 g/cm^3,

Ni atomic number: 58.7, Ti atomic number: 47.8,

transformation strain: $\Delta \varepsilon_A^M = 0.05$

$$\frac{d\sigma}{dT}=\frac{\Delta S_A^B}{\Delta\varepsilon_A^B}=\frac{\Delta H_A^B}{T\cdot\Delta\varepsilon_A^B}=\frac{20J/g\times6.45\times10^6 g/m^3\times1m^3}{333K\times0.05}=7.74\times10^6\ \text{J/K}=7.74\ \text{MPa/K}$$

Experimental value shows $\frac{d\sigma}{dT}=(7\pm1)MPa/K$ [*4, 54-56*]. It is close to the theoretical prediction because enthalpy change and transformation strain may be different for different materials. [*57*]

2.3 Superelastic Effect of NiTi Shape Memory Alloy

2.3.1 Residual Stress in NiTi Thin Films

The residual stress in NiTi thin films comes from two origins: the intrinsic stress from the deposition process, and the thermal stress from mismatch of the coefficient of thermal expansion (CTE) between the substrate and the thin film [*58-62*]. The residual stress in a thin film can be measured by the wafer-curvature method using the well-known Stoney equation [*63, 64*], assuming the curvature change is elastic.

The intrinsic residual stress is the result of the non-equilibrium characteristics of the sputter deposition process, which involves rapid thermal energy dissipation and simultaneous energetic particle bombardment during film growth. It is natural that the intrinsic residual stress is affected by deposition parameters such as Ar pressure, deposition temperature, and whether the thin films are crystalline or amorphous. The intrinsic residual stress can be relaxed by post annealing. Grummon *et al.* proposed a general stress model (Figure 6) describing the stress relaxation processes of NiTi thin

films [*58*]. Stress relaxation path of isochronal and isothermal annealing of NiTi thin films are given for different deposition conditions. The intrinsic stress in a NiTi thin film is completely relaxed at crystallization temperature around 753K. Cooling from that temperature, the coefficient of thermal expansion (CTE) mismatch between silicon substrates and NiTi gives rise to thermal stress. For instance, the CTE mismatch between NiTi and Silicon substrates gives -1.0 MPa/K thermal stress rate, which is derived as:

$$\begin{aligned} &\alpha_{NiTi} = 11.4\times10^{-6}, \alpha_{Si} = 3\times10^{-6} \\ &E_{NiTi} = 83GPa, \upsilon = 0.33 \\ &\frac{d\sigma_T}{dT} = \frac{E_f}{1-\upsilon}\cdot(\alpha_S - \alpha_f) = \frac{83\times10^3}{1-0.33}(-8.4\times10^{-6}) \approx -1.01MPa/K \end{aligned} ,$$

where α_{NiTi}, α_{Si} are CTE of NiTi thin films and silicon substrates, E_{NiTi} and υ are elastic modulus and Poisson's ratio of NiTi thin films.

The thermal stress can be relaxed by martensite transformation partly or completely, and restored by the reverse phase transformation. The transformational stress relaxation rate is governed by the thermodynamics of martensite phase transformation. It can be expressed in the form of Clausius-Clapeyron equation, which was discussed in 2.2.2.

This transformational stress relaxation and restoration cause a quite significant but reversible wafer curvature /displacement change within a relatively small temperature hysteresis of about 80K. This is the basis of some NiTi thin film micro-actuators for MEMS applications [*60, 65, 66*].

2.3.2 Temperature Dependence of Superelasticity

Superelasticity originates from the stress-induced phase transformations upon loading, and the subsequent reverse transformations upon unloading. The external stress changes the free energy and induces phase transformations according to the Clausius-Clapeyron equation discussed in section 2.2.2:

For instance, tensile loading an austenitic NiTi specimen at temperature 50K above M_S requires $\sigma = 7.74MPa/K \times 50K = 387MPa$ tensile stress to induce the martensitic phase transformation at that temperature.

Superelasticity is therefore closely dependant on testing temperatures. The highest temperature at which martensite can no longer be stress induced is called M_d. Above M_d NiTi alloy deforms like ordinary metals by slip-plasticity. Below the A_S temperature, martensite can be stress induced but does not completely revert to austenite. Thus, superelasticity appears in a temperature range from near A_f and up to M_d. The greatest ability to recover occurs just above A_f [4]. Figure 7 shows the stress-strain curves for uniaxial loading of a NiTi specimen at different temperatures. The critical stress to initiate the plateau region where stress-induced martensites begin to form, increases with increasing temperature, which is seen in Figure 8, where open circles represent the critical stresses upon loading, and closed ones are critical stresses upon unloading.

The dependence of the shape memory effect and superelasticity on test temperatures can be further presented in the schematic diagram of Figure 9. The line with a positive slope represents the critical stress to induce martensite, which is similar to the one with

open circles in Figure 8. The lines with negative slopes represent the critical stress for slip-plasticity. If the critical stress to introduce plasticity is very low (line B), complete superelasticity can not be expected, because slip is an irreversible process and has a detrimental effect on the thermoelastic phase transformations. If the critical stress for slip is high enough (line (A)), superelasticity can appear at temperatures above A_f within the shaded region. Reverse transformation occurs upon unloading, since the martensite is unstable at temperatures above A_f in the absence of stress. Similarly, at temperatures below A_s the deformed martensites are stable, and the strain can recover only by reverse transformation on subsequent re-heating. In the temperature regime between A_s and A_f the martensites are partly unstable. The M_d temperature is the maximum temperature that martensite phase can be stress induced. Above the M_d temperature slip plasticity is the only inelastic deformation mechanism in austenitic NiTi.

2.3.3 Superelasticity and Phase Transformations

Superelasticity stems from the stress-induced phase transformations. Although the parent phase is invariably the B2 austenite, there are three low-temperature phases that can emerge after phase transformations, depending on chemical composition and thermal-mechanical history. The superelasticity associated with each low temperature phase is discussed briefly here.

B2-B19' Transformations Stress induced B2-B19' phase transformation is the most important to the superelasticity of NiTi. The mechanism of superelasticity is the stress-induced martensite phase transformation upon loading and reverse phase transformation upon unloading. There is direct experimental evidence in Cu-Al-Ni single crystals to support this mechanism [*67*]. In uniaxial loading of a Cu-Al-Ni single crystal, a particular variant of martensite was stress-induced with the habit plane that was most favorable under the applied external stress. The parent single crystal changed into a single crystal of that martensite variant at the end of the stress plateau. Upon unloading the reverse transformation occurred with the same habit plane and the strain recovered completely upon unloading [*67*]. The recoverable strain also agreed with crystallographic predictions.

The verification of the mechanism of superelasticity in NiTi has some complications. Solution-treated single crystal NiTi has low critical stress for plastic slip, which is the case of line B discussed in the section 2.3.2 and Figure 9. When such a specimen is subjected to external stress at temperature above A_f, plastic flow started before the onset of stress-induced phase transformations and thus excluded superelasticity. However aged single crystal Ni-rich NiTi had higher critical stress for plastic slip due to precipitation strengthening. Superelasticity was achieved for aged NiTi single crystals, which are shown in Figure 10. But the aged single crystals did not give full recovery strain because untransformed regions were left due to the presence of precipitates. As a result, the recoverable strain was smaller than theoretical value [*68*].

How superelasticity from B2-B19' martensite phase transformation is affected by thermomechanical treatments is discussed in 2.3.5.

B2-R Transformation The B2-R transformation is an independent martensite phase transformation between B2-R-B19' transformations. However if the martensite phase start temperature M_s is higher than R phase start temperature R_s, the R-B19' phase transformation is suppressed. Superelasticity is also attainable with R-phase transformation, although the recoverable strain is about 0.5%. Ling and Kaplov studied the shape memory effect from R-phase transformation in bending tests coupled with X-ray diffraction measurements [*69, 70*]. More systematic work on superelasticity and shape memory effects were done by Miyazaki et al. by tensile tests on both 50 at.% Ti- 47 Ni-3 Fe polycrystals [*71*] and aged 50.5at.%NiTi single crystals [*72*]. The stress-strain curves of aged single crystal NiTi specimens at different temperatures are shown in Figure 11.

R-phase transformation temperatures are different from that of B2-B19' transformations. It is interesting to note that the recoverable strain increases with decreasing temperature. The reason is that the rhombohedra angle of R-phases changes with temperature. Figure 12 shows the critical stress for stress-induced R-phase transformation increased quite rapidly with increasing temperature, because the recoverable strains is so small that the slope of $d\sigma / dT$ in the Clausius-Clapeyron equation (discussed in 2.2.2) becomes very large. The available shape memory or

recoverable strain of R-phase transformation is small (less than 1% in polycrystals). But the small transformation strain may contribute to the small temperature hysteresis of R-phase transformation (1-2K), which is a very useful property for actuator applications [*4*].

B2-B19 Transformations B2-B19 (cubic to orthorhombic) transformation exists in NiTiCu SMAs, when the Cu content exceeds more than 8%-10%. The theoretical recovery strain associated with B2–B19 transformation was calculated for 40 at.% Ni-10Cu-50Ti alloy as a function of orientation by Nam *et al.* [*73*]. The maximum recoverable strain of 5.3% is obtained at $<110>_p$ orientation, which is much smaller than the maximum 10.5% strain in B2–B19' transformation. But there is no supporting data from single crystal NiTiCu experiments.

Polycrystal NiTiCu SMAs have smaller temperature hysteresis in superelasticity, compared to binary NiTi (Figure 13). The temperature hysteresis decreases with increasing Cu content, the minimum being 4K for 20at% Cu. It was suggested that volume change in B2-B19 phase transformation decreases with increasing Cu content up to 12.5 at.% Cu [*73*]. Further addition of Cu would increase the volume change. The small volume change may be one factor for the small temperature hysteresis but that alone cannot explain all the experimental data. Another mechanism proposed is the parent phase strengthening by solution of Cu atoms [*74*]. The frictional stress for twin boundary movement is suppressed if the introduction of dislocations is avoided.

2.3.4 Mechanical and Microstructural Behaviors in Superelasticity

The loading and unloading of a superelastic NiTi sample involves complicated changes in microstructure and multiple stages. In stress-strain curves, the loading stage has a plateau region, after stress has reached a critical level. The plateau region involves stress-induced martensite phase transformation that is triggered by a resolved shear stress over the most favorably oriented martensite habit plane. An internally twinned structure is formed within a single martensite plate. Such a martensite plate can be called a correspondence variant pair (CVP) because two related martensite single crystal variants develop. This is the first stage of superelastic loading that is well-understood.

The second stage is characterized by the strain hardening with slightly increasing superelastic strain, which was noticed by Miyazaki in multistage loading of superelastic NiTi alloy (Figure 14) [*68*]. It is suggested the detwinning process may explain this behavior [*75-77*]. The detwinning is that one martensite variant of the CVP grows at the expense of the other and finally saturates the whole martensite plate. The detwinning process has been observed in TEM of loaded martensitic NiTi alloy (Figure 15 and [*78*]), which occurred after the alignment of martensite twins (CVPs) with external stress was complete. Finally the martensite plate consists of only one variant instead of twins. Dislocations are generated in the late stage or after the detwinning process has finished (Figure 15). From then on slip-plasticity is the main deformation mechanism [*75, 78*], which is the third stage. In-situ TEM observation of stress-induced martensite

transformation and plastic deformation was carried out by Jiang *et al.* [*79*]. However they did not intend to study the detwinning in NiTi alloy, although the TEM micrographs showed some evidence of detwinning (Figure 16).

Tension-compression asymmetry was found present in single crystal and textured polycrystalline NiTi SMA [*76, 77, 80-82*]. The reason is that the CVP with the largest resolved shear stress component is induced preferentially than the rest 23 CVPs, which can be described by the Schmid law [*76*]. The tension-compression asymmetry arises from the different Schmid factors between tensile and compressive directions. Figure 17 shows the tension-compression asymmetry of [211] orientated single crystal NiTi alloy [*76*]

In polycrystal NiTi samples without texture, the stress induced martensite transformation plateau is found to be inhomogeneous, like Lüders deformation, that involves nucleation at some point within the specimen and the subsequent propagation, according to direct observation with an infrared imaging radiometer by Kyriakides and Shaw (Figure 18, [*83*]).

2.3.5 Effects of Thermo-Mechanical Treatments on Superelasticity

Thermomechanical treatments, mainly by slip-plastic deformation and aging treatments, are important to the superelasticity and shape memory effects. Thermoelastic phase transformations are reversible but thermomechanical treatments

introduce irreversible changes to the microstructure. Their main purpose is to increase the critical stress for plastic slip by strengthening the parent phase. As discussed in 2.3.2, low critical stress for slip in solutionized single crystal NiTi makes the realization of superelasticity impossible. Higher critical stress for slip means that superelasticity can be obtained over a wider temperature range and with larger recoverable strain. The full potential of NiTi SMA can only be brought out after suitable thermomechanical treatments.

Cold-working followed by annealing enhances superelasticity. Cold work introduces dislocations into the specimen; post annealing is a recovery process during which dislocations relax and rearrange. The critical stress for plastic slip is increased after this process. As a result, the plateau stress of superelastic loading can also be increased by loading at higher temperature. The temperature and stress range for superelasticity is thus increased. Figure 19 shows a series of stress-strain curves from solution-treated 49.8at.% NiTi wires. There is only partial superelasticity at temperature above A_f. After uniaxial cold drawing and post annealing at 673K for 1h, good superelasticity was achieved (Figure 20). Figure 21 shows the TEM images of specimens at different stages of thermomechanical treatments. NiTi alloy was in a recovered but not recrystallized state after annealing at 673K, and led to the best superelasticity. Increasing the annealing temperature to 773K resulted in recrystallization, which again lead to lowered critical stress of slip and decreased superelasticity.

Aging treatment enhances superelasticity by precipitation strengthening in the parent phase. Figure 22 shows the stress-strain curves of 50.6at.% NiTi wire that were solutionized and aged at 673K for 1h. Superelasticity was achievable only in a narrow temperature range. Figure 23 shows that after solution treatment and aging at 773K for 1h, much better superelasticity was obtained. TEM study (Figure 24) showed that precipitates were small but densely distributed in the matrix after aging at 673K; precipitates were larger and less densely distributed after aging at 773K. Small and densely distributed precipitates were more effective to strengthen the parent phase, which results in improved superelasticity.

Combined effects of cold-working and aging enhance superelasticity. Combined use of work-hardening and age-hardening is more effective to increase the critical stress for slip, which is presented in Figure 25. Solutionized 50.6at.%NiTi wires were cold drawn and aged at 673K for 1h. Compared to Figure 22, complete superelasticity was available at higher stress level. Besides, the combined treatment was useful for increasing cyclic stability of superelasticity [*84*].

2.4 The Two-way Shape memory Effect

2.4.1. Introduction

The two-way shape memory effects (TWSME) is the reversible shape change during martensite and reverse phase transformations, without the stimulus of external stress. In

conventional one-way shape memory effect, the martensite transformation does not result in any macroscopic shape change because the martensite variants are self-accommodated to minimize elastic and transformation strain.

The two-way shape memory effect is not an intrinsic effect but can only be obtained by certain thermomechanical treatments, termed as "training". It was first noted in 1965 by Wang *et al* [*85*]. In 1974 Nagasawa *et al.* did the first detailed research on this "reversible shape memory effect" in NiTi and CuZn SMA[*86*]. After the training procedures, microstructural and mechanical anisotropies are introduced into the material. The martensite variant formation follows these structural anisotropies during phase transformations to minimize internal energy. Macroscopic strain would appear because martensite variants form that have preferential alignment. Reverse austenite transformation cancels the shape change. More details about the TWSME mechanism will be discussed in 2.4.2.

2.4.2. Training Methods and Mechanisms of TWSME

Various training methods have been developed to realize TWSME: (1) constrained aging, (2) thermomechanical cycling, (3) plastic deformation by slip. There are variations in configurations of each category. The mechanism associated with each of these training methods is discussed below.

Constrained Aging Training Figure 26 illustrates the process of an constrained aging training of NiTi springs [*87*]. The spring was aging at 773K under constraint, which was an over stretched position. After aging, the spring was deformed in martensite phase to a crushed position. The reverse transformation expanded the spring while the martensite transformation shortened the spring, completing the two-way cycle. However the authors did not propose any possible precipitates that might be induce the TWSME.

Isalgue reported that the aging process under external stress created the oriented growth of γ precipitates in Cu-Zn-Al SMA [*88*]. Zhang further found that oriented strain field around these γ precipitates were distributed along one direction in austenite, regardless of the grain orientation [*89*]. But the γ precipitates are embedded in the austenite phase coherently. While in the martensite phase, γ precipitates did not result in any strain fields. The reversible strain fields around precipitates that were produced by constrained aging may explain the TWSME.

Fukuda *et al.* aged a single crystal 51.at% NiTi under compressive stress along [111] [*90*]. Ni_4Ti_3 precipitates were formed coherently to the matrix along [111]. They explained the resulting TWSME from an energy approach: the volume fraction of precipitates was about 9%, based on TEM study of the size, shape and distribution of the precipitates. The matrix was expanded elastically about 0.2% on average along the [111] direction. The elastic energy accumulated in the matrix was estimated to be about 0.3 MJ/m^3; it was about 1.5% of the latent heat of the B2 --> R transformation. The

thermally induced R-phase was composed of a single variant and the spontaneous strain along the [111] direction was about 0.8% of expansion. The maximum work from the spontaneous shape change was estimated to be about 0.17 MJ/m^3. Chang *et al.* reported constrained aging at room temperature [*91*], where NiTi wires were first solutionized and aged at elevated temperature and then bended in round shape in room temperature for 24 h. This, however, is more likely to be the deformation training method.

Precipitates formed in constrain aging training can be observed using TEM [*89, 90*]. It has been shown that the oriented strain fields around precipitates in NiTi can cause martensite variants to align in preferential directions. The stress fields around the precipitates can be recovered again after the reverse austenite phase transformation [*89*]. Molecular dynamics simulation indicated that oriented tension stress fields in the middle line of the dislocation band are favorable sites for the martensite nucleation and growth of preferred variants [*89*].

Thermomechanical Training Thermomechanical training methods have different variations, depending on the researcher's interpretation of mechanisms of TWSME. The most common setup was cycling between temperatures above A_f and below M_f when the specimen was subjected to external tension, compression or bending stress [*92-95*]. Pons *et al.* used the following training cycles: cooling down below the M_f temperature under a constant tensile uniaxial stress of 35 MPa, and then unload and heat up to A_f with zero stress [*96*]. This low stress was used to train a Cu-based shape

memory alloy. Prader *et al.* kept the tensile strain constant while thermal cycling between M_f and M_d temperatures. There is no consensus about the optimal training method.

Explanations of the development of the TWSME often involve either the presence after training of a low proportion of locally stabilized martensites in the parent phase, or the presence after training of an internal stress field in the material. Stalmans [*92*] *et al.* carried out a well-cited research about thermomechanical cycling on Cu-Zn-Al SMA and discussed the mechanism of TWSME. They disproved these two previous explanations. Following their study, the most important effect of the dislocation arrays which are introduced during the training is not to develop internal stresses but rather to give rise to a microstructural anisotropy inducing a thermodynamic anisotropy. The thermodynamic anisotropy means that after training, the crystallographically equivalent martensite variants are no longer thermodynamically equivalent: the trained martensite variants are thermodynamically preferred to the non-trained variants. The authors argued that this thermodynamic anisotropy must have come from certain changes in microstructures as the result of training. The microstructural basis of the thermodynamic anisotropy was termed microstructural anisotropy. However, the exact nature of the microstructural anisotropy was not explained clearly. The authors speculated that dislocations arrays generated during the training should contribute to it. Manach *et al.* carried out a similar thermomechanical training procedure but in the pure shear loading conditions [*97*]. They supported Stalmans conclusion that internal stress field had only a weak influence

on the development of TWSME, and dislocation arrays introduced by training created not only internal stresses but also a thermodynamic anisotropy. They further suggested the anisotropy is due to the friction energy which is after training no longer equal for all martensite variants.

One cycle slip-plasticity deformation training The slip-plastic deformation training was actually the training method used in the original discovery [*85*] and initial study of TWSME [*86*]. The specimens were deformed in the martensite phase to introduce a certain level of dislocations [*98-103*]. Slip-plasticity training has the advantage of requiring fewer training cycles. Figure 27 shows the TWSME obtained from the uniaxial tensile deformation training. As discussed previously, the mechanism of TWSME from slip-plasticity training is believed to be that the microstructural anisotropies (oriented precipitates, dislocations, residual martensites) and their associated mechanical anisotropies would select martensite variants in specific orientations that are energetically favorable.

Although dislocations can be observed in transmission electron microscopy (TEM), they look like densely tangled black lines. Although possible, it is difficult to get information such as strains and strain gradient from direct TEM observation of dislocations. The localized stress fields can not be observed in TEM directly. because these obstacles, the mechanism of TWSME has not been clarified using TEM.

The one-to-one correspondence between TWSME and microstructure "memory

effect" was found in Au-Cd alloy, where the specimen exhibited same variant configuration upon heating and cooling (Figure 28) under optical microscope [*104*]. Similar results are more difficult to get from NiTi alloy due to the fine size of martensite variants.

2.4.3 Phase Transformation Temperatures of TWSME

The phase transformation temperatures are affected by the presence of TWSME. Thermomechanical training of NiTi wires lowered the A_s and A_f temperatures significantly but had a less influence on M_s and M_f temperatures [*105*]. Stalmans *et al.* showed that external stress opposing the direction of TWSME shifted all transformation temperatures downwards [*106*].

If a NiTi bar was trained by slip-plasticity method using uniaxial tensile stress, the resulting TWSME would be: shrinkage during heating and elongation during the cooling. Assume there is a tensile residual stress field in the NiTi bar that is responsible for inducing the TWSME (Figure 29). Applying external compressive stress to NiTi bar decreases the internal tensile stress, if the level of the external compressive stress is not higher than that of the internal tensile stress. A schematic diagram is shown Figure 30. The actual stress inside the specimen is decreased by the external stress. According to the Clausius-Clapeyron equation, lowered stress also lowers the phase transformation temperatures.

However, the external compressive stress is in the opposite direction of the TWSME. During cooling the external compressive stress impedes the shrinkage of NiTi bar. If large enough, the compressive stress can suppress the TWSME completely.

In experiments, both lowering phase transformation temperatures and suppressing of TWSME were observed when applying external stress in the opposite direction of TWSME (Figure 31) [*106*]. In Figure 31, strain change vs. temperature is presented for the cooling (a) and heating (b) direction, for various external stress levels. The TWSME with zero external stress is also shown. Note in Figure 31 the compressive stress is in the opposite direction of TWSME, which suppresses completely the TWSME at -52.1MPa. The phase transformation temperatures are elevated by the tensile stress and lowered by the compressive stress in the opposite direction of TWSME.

Stalmans et al. also proposed a thermodynamic explanation for this interesting phenomenon [*106*]. The Clausius-Clapeyron equation derived in 2.2.2 can be expressed as

$$\frac{\Delta\sigma}{\Delta T} = \frac{\Delta H_A^B}{T\Delta\varepsilon_A^B}, \text{(eq. 1.10).}$$

The enthalpy change from austenite phase to martensite phase is positive (heat flows into NiTi): $\Delta H_A^M > 0$, which is why heat flow jumps in the cooling DSC curves when phase transformation occurs (Figure 32). The left hand side of the C-C equation $\frac{\Delta\sigma}{\Delta T}$ must has the same sign as the right hand side $\frac{\Delta H_A^M}{T\Delta\varepsilon_A^M}$. If a normal SMA specimen was loaded by tensile stress and cooled from austenite to martensite phase, the phase

transformation strain was also tensile. Since $\Delta H_A^M > 0, \Delta \varepsilon_A^M > 0$ and $\frac{\Delta H_A^M}{T \Delta \varepsilon_A^M} > 0$, the phase transformation temperatures were shifted upwards ($\Delta T > 0$) compared to free standing specimen, because the tensile stress $\Delta\sigma > 0$.

When heating from martensite to austenite phase, the $\Delta H_M^A < 0$. The recovery of phase transformation strain is in the opposite direction of tensile strain: $\Delta \varepsilon_M^A < 0$. As a result $\Delta H_M^A < 0, \Delta \varepsilon_M^A < 0 \rightarrow \frac{\Delta H_M^A}{T \Delta \varepsilon_M^A} > 0$. There was no change to the tensile stress, so the phase transformation temperatures were still increased ($\Delta T > 0$).

In TWSME, however, the situation is different depending on the direction of external stress. Consider a specimen that was trained to possess TWSME giving elongation during austenite-martensite transformation on cooling ($\Delta \varepsilon_A^M > 0$) and shrinkage during martensite-austenite transformation on heating ($\Delta \varepsilon_M^A < 0$). Tensile stress still elevates phase transformation temperatures as described in the previous case. But compressive stress lowered the phase transformation temperatures becomes: for cooling from austenite to martensite phase, $\Delta H_A^M > 0, \Delta \varepsilon_A^M > 0$ and $\frac{\Delta H_A^M}{T \Delta \varepsilon_A^M} > 0$. Since $\Delta\sigma < 0$ (compressive), so $\Delta T < 0$ that the left hand side of (eq. 1.10) was positive as the right hand side; $\frac{\Delta H_M^A}{T \Delta \varepsilon_M^A}$ is still positive when heating from martensite to austenite phase, because $\Delta H_M^A < 0$, $\Delta \varepsilon_M^A < 0$. Since $\Delta\sigma < 0$ (compressive), $\Delta T < 0$. The key point is that the external stress was in opposite direction against strain change in TWSME as compared to the case in SME, which caused the negative temperature shift. Figure 31

shows the strain-temperature curves in Stalmans' study that exhibited the lowering phase transformation temperatures.

2.5 Contact Mechanics and Tribological Study

The subject of contact mechanics may be said to have started in 1882 with the publication by Heinrich Hertz of his classic paper *On the contact of elastic solids* [*107*]. His interest in the problem was aroused by the question whether the force of holding glass lenses could have a significant influence on the pattern of optical interference fringes. However, developments in the theory did not appear in the literature until the early 20th century, stimulated by engineering developments on the railways, in marine reduction gears, and in the rolling contact bearing industry.

Now contact mechanics are used widely in science and engineering disciplines like geology, astronomy, defense, materials and mechanical engineering, where impact and contact is investigated. Most importantly contact mechanics serves as the theoretical basis to tribological testing methods like indentation, wear and scratch tests.

2.5.1 Elastic Contact Problems

Analytical solutions are given for many elastic contact problems. The elastic contact problems of spherical and sharp indenters into a half space are especially

important because they are directly related to the measurement of hardness. The mean contact pressure P_m is simply normal load P on the indenter over contact area πa^2 :

$$p_m = \frac{P}{\pi a^2}$$

In the elastic spherical indentation, the contact radius a can be calculated:

$$a = \left(\frac{3PR}{4E^*}\right)^{1/3},$$

where R is the radius of indenter, and E^* is the reduced modulus, a function of the modulus of the indenter and the substrate:

$$\frac{1}{E^*} = \frac{1}{E_{indenter}} + \frac{1}{E_{substrate}}.$$

On the contact surface the contact pressure is not uniformly distributed. The maximum contact pressure p_0 is expressed as

$$p_0 = \frac{3P}{2\pi a^2} = \left(\frac{6PE^{*2}}{\pi^3 R^2}\right)^{1/3}$$

The vertical displacement of the surface within the contact radius, measured with respect to the original specimen free surface, is given by:

$$u_z(r) = -\frac{1-\upsilon_{substrate}^{\ 2}}{E_{substrate}} \frac{\pi p_0}{4a}(2a^2 - r^2),\ r \le a,$$

where $\upsilon_{substrate}$ is the Poisson's ratio of substrate [*108*]. The stress distribution is depicted in Figure 33 [*108*]. The maximum shear stress is located at a distance of half contact radius below surface. Figure 34 presents the photo-elastic fringes pattern of shear stress from indenters of various geometries. They all show concentric

hemispherical contours. For uniform pressure and cylindrical contact, the highest stress is located at a distance from the contact surface. This distance is much shorter in the case of point loading. The flat punch shows stress concentration at the contact edges.

2.5.2 Elastic-Plastic Contact Problems and Instrumented Indentation

In metals, slip-plasticity develops when the elastic contact stress exceeds the material's yield stress. As the indenter is pressed deeper into the substrate, a plastic zone appears below the indenter tip, surrounded by an elastic region. This is called the "contained mode". The plastic zone grows with indentation depth and finally breaks out to the free surface. From then on the displaced material is free to escape by plastic flow to the sides of the indenter. This is the uncontained mode of indentation. It begins when mean contact pressure p_m reaches about triple the yield stress:

$$p_m = \frac{P}{\pi a^2} = C\sigma_{yield}.$$

When p_m is between 1 and 3, the plastic zone is contained by elastic materials [*108*]. The mean pressure is also defined as the hardness of the material.

Indentation is a traditional method to measure the hardness of materials. Instrumented indentation is the advanced form of indentation, where both displacement and load of the indenter is monitored continuously. It has been developed during the past decade driven by the need to measure modulus and hardness of thin films efficiently.

Nix *et al.* first proposed that the contact radius could be calculated from load-displacement curves, assuming that the initial part of the unloading curve is linear [*109*]. However when the "sink-in" or "pile-up" situation is present (Figure 35), the Doerner and Nix method is not accurate enough because the contact radius is larger in the "pile-up" situation and smaller when the "sink-in" occurs. This method was later improved by Oliver and Pharr [*110*], whose method is now used to calculate the contact radius.

Analytical solutions for most elastic-plastic contact problems are not readily available, especially with hardening present. But most metals are elastic-plastic solids with hardening behavior. Both finite element analysis and semi-analytical models are commonly used in analyzing elastic-plastic contact problems.

A semi analytical: spherical cavity model was proposed by Johnson to explain the elastic-plastic indentation process [*108*]. In this spherical cavity model, the contact surface of the indenter is encased in a hemi-spherical "core" with a hydrostatic component $\bar{p}$. Outside the core it is assumed that the material will respond the same way as in an elastic half space containing a spherical cavity under hydrostatic pressure $\bar{p}$. The elastic-plastic boundary is somewhere outside the spherical cavity. The hydrostatic pressure $\bar{p}$ below the indenter can be expressed as:

$$\frac{\bar{p}}{Y} = \frac{2}{3}\{1 + \ln[\frac{\frac{E^* \tan\beta}{Y} + 4(1-2\upsilon)}{6(1-\upsilon)}]\},$$

where Y is the yield stress of indented material. The β is the angle of indenter. For the Berkovich indenter, $\beta=19.3°$.

The representative strain proposed by Tabor is also used to characterize spherical indentation into elastic-plastic solids [*111, 112*]. The representative strain is a depth-sensitive parameter that is defined as:

$$\varepsilon_r = 0.2\frac{a}{R},$$

where a is the contact radius and R the indenter radius. *When the representative strain is equal to the true strain, the hardness H is about 2.8 times of the true stress* (Figure 36, [*111, 112*]):

$$\frac{H}{Y} = 2.8, \quad when \quad \varepsilon_r = \varepsilon$$

Tabor arrived at this conclusion after comparing the experimental data of spherical indentation and uniaxial deformation of copper and steel. The indentation and uniaxial deformation data set collapsed into a single line (Figure 36) when applying the above two equations. The correlation between spherical indentation experiments and uniaxial tensile data, although an empirical law, indicates that using the concept of representative strain, spherical indentation experiments may possibly be used to measure the true stress-true strain relationship.

Finite element analysis is an effective tool for investigating elastic-plastic contact problems [*113*]. Figure 37 shows the finite element modeling of the expansion of plastic zone under spherical indentation [*114*]. Sinclair *et al.* carried out a detailed finite

element analysis of the spherical indentation on elastic-plastic solids [*115*]. They confirmed Tabor's simple experimental correlations for work-hardening materials using the representative strain, and found generally good agreement between theory and other physical evidence. However they also found there was high strain gradient near the contact edge that was not predicted before.

2.5.3 Indentation-induced Shape Memory Effect

Shape memory effect under contact loading conditions has received very little attention previously. This is partly due to the complexity of the problem and the absence of suitable characterization methods. Ni *et al.* reported the shape memory and superelastic effects in NiTi alloy during spherical and sharp indentation [*116, 117*] using a well-controlled instrumented indentation method. A recovery ratio η was defined to quantify the indent recovery:

$$\eta = \frac{h_{\max} - h_{residual}}{h_{\max}},$$

where $h_{\max}$ is the maximum indentation depth, and $h_{residual}$ is the indent depth after recovery. Spherical indents in NiTi alloy recovered almost completely ($\eta = 100\%$) due to the shape memory or superelastic effect, if the indentation representative strain was less than 5% [*116, 117*]. Spherical indents in martensitic NiTi recovered after being heated above A_f (Figure 38) while in austenitic NiTi the indents recovered during

unloading (Figure 39 (a)). The recovery ratio was only about 45% during sharp indentation (Berkovich), because slip-plasticity impeded the martensite-austenite transformation and affected SME adversely. Deeper spherical indentation also resulted in decreased recovery ratio.

Gall *et al.* did Vickers indentation on NiTi single crystals and observed the existence of dislocations in the vicinity of indents in TEM (Figure 40). The same study also suggested that the precipitates size and crystal orientation also affect the recovery ratio [*118, 119*]. Indentation on single crystal CuAlNi SMA also showed indentation-induced SME [*120, 121*].

The above research shows robust shape memory and superelastic effects under contact loading conditions in NiTi and Cu-based SMA. This new phenomenon of shape memory alloys could be used to engineer novel applications in surface engineering, information storage and optics. It also prompts new questions about the mechanism of the shape memory effect.

2.5.4 Wear and Scratch Damage

Wear is the removal of material from a solid surface as a result of mechanical action. Wear can be divided into four categories: adhesive wear, abrasive wear, corrosive wear and surface fracture wear [*122, 123*]. In addition, there are several compound types of wear: erosion, fretting, and cavitation erosion [*122, 123*].

Adhesive wear arises as a result of a process by which isolated spots on two sliding surfaces adhere together momentarily. When shear occurs, the shear takes place at some place other than the original interface. As a result, an adhering particle is formed, which may come loose at a later stage. Adhesive wear is considered the purest and most important form of wear because it is the only one which is always present. Unlike other types of wear, adhesive wear can not be completely eliminated.

A quantitative expression of adhesive wear was derived by Archard [*124-126*]:

$$V = \frac{kPx}{3H},$$

where V is the wear volume formed after sliding through a distance x; P is the normal load and H the hardness of the tested material. The non-dimensional constant k represents the probability that a junction between two surfaces would lead to the formation of a wear particle. It would be ideal but actually difficult to relate the wear coefficient k to basic material properties (modulus and hardness) and surface properties (surface roughness and lubrication conditions).

Abrasive wear is produced by a hard protuberance plowing a groove in a softer surface so that the material in the groove is worn away. A similar expression to Archard's equation is also obtained:

$$V = \frac{\overline{\tan\theta} Px}{3H},$$

where $\overline{\tan\theta}$ is the tangent of the average effective roughness angle for the hard surface,

or for hard abrasive grains at an interface [*127*]. Values of $\overline{\tan\theta}$ under various circumstances have been tabulated [*127*]. This equation can explain some wear situations, for example, the reduction in wear rate when the abrasive hardness and the tested material hardness are nearly equal; the reduction in wear rate when smaller abrasive particles are used [*127*].

Corrosive wear is a form of wear where corrosion of a surface first occurs, then sliding occurs and removes the corrosion products, allowing further corrosion. Quantitative information on this form of wear is not readily available. Because the wear rate is governed by so many factors: the rate of corrosion, the rate of removal of corrosion products, the geometry of the sliding surfaces, and whether the whole of the corrosion products are removed all at once or in part.

Surface fracture wear is common in rolling elements like ball and roller bearings, wheels and rails, and gears. In this case, as the stresses come and go during continued rolling service, cracks grow in or below the surface of the element, and eventually a spalled particle is produced. This phenomenon is closely related to fatigue failure.

Wear tests are used to measure wear resistance. ASTM standards exist regarding various test materials and experimental configurations [*128*]. The pin-on-disk or ball-on-disk wear test is used most widely [*129*]. More details will be discussed in Chapter 3.

The scratch test is a semi-quantitative method to evaluate a coating or thin films strength and interfacial adhesion. Small-radius spherical indenters are used most widely

as the scratchers. The radius is between 100 and 200 μm. Different scratch methods, like progressively increasing load, constant load, and repeated scratch are available on various testing platforms.

Coating failure occurs when the scratch load is increased to a certain value termed the critical load. The failure can happen at the interface between coating and substrate, or within the coating itself, or a combination of both. The critical load is the most important numerical indication of interfacial adhesion from a scratch test. Although scratch tests are used widely and are easily understood intuitively, and there are ongoing efforts to establish a standard [*130*]. It remains difficult to interpret scratch test results quantitatively and consistently. Description of the sudden failure of the coating is beyond the established realm of continuum elasticity and plasticity.

Acoustic emission (AE) signals result either from the sudden release of elastic energy, or from surface interactions such as friction and adhesion. Sudden energy release can occur during unstable crack growth, high-speed phase transformations, or plastic instabilities. A transducer to measure the acoustic emission is attached to the scratch slider and its output can be correlated to events which occur along the scratch track. At constant load, as the scratch is created a baseline AE response is established due to plastic deformation and friction/adhesion. Individual AE responses from fracture are superimposed upon this signal. The magnitude of the acoustic emission signal depends on the size of the crack produced since the energy in the AE signal scales with the energy released in the process [*131*]. For coatings thicker than a micron, the area of

adhesive failure is large compared to the area of through-thickness cracks. Therefore, a large jump in the acoustic signal is thus a reasonable indication of adhesive failure.

Besides establishing the critical load, microscopic observation of the failed region also provides important information on the failure mechanism. Bull et al. proposed several failure modes from the appearance of the failed hard coating, such as through-thickness cracking, coating detachment, chipping, buckling, wedge spallation [*132, 133*]. The geometry and distribution of coating cracks also depends on the mechanical properties of coating and substrate.

2.5.5 Tribological Study on Bulk NiTi Shape Memory Alloy

A number of researchers have investigated the erosion wear behavior of NiTi alloys in different wear modes and compared NiTi alloys to conventional engineering materials like steels, Ni-based and Co-based tribo-alloys [*134-144*]. It is found that NiTi alloy has a better erosion wear resistance than conventional wear-resistant materials, especially during cavitation erosion processes [*141, 143*]. In addition, NiTi alloy is resistant to corrosive wear [*145*].

The wear resistance of conventional tribo-materials strongly depends on their mechanical properties such as hardness, modulus, hardening [*146, 147*]. Each of the mechanical properties contributes in greater or lesser degree to the wear resistance in different wear modes. It has been suggested that the high wear resistance of NiTi alloy

can be attributable to superelasticity [*142*]. Richman *et al.* demonstrated the superior cavitation resistance of NiTi alloy compared to a number of standard and wear-resistant materials including cast martensitic stainless steels and Co-based alloys (Stellite) [*141*]. Shida and Sugimoto observed remarkable erosion resistance of NiTi alloys during a water-jet erosion test [*142*]. Liang et al. observed that NiTi alloy showed high resistance to wear under impact during a sand blasting test. They compared NiTi alloy to a wear resistant alloy Ni-hard-4 ($Cr_{8.6}Ni_{5.2}C_{3.2}Fe$) and showed that NiTi has a lower erosion rate than the Ni-hard-4 alloy. They noticed that there was a strong correlation between the wear resistance and the superelastic strain.

Bulk superelastic NiTi also shows excellent adhesive and abrasive wear resistance. Li *et al.* carried out pin-on-disk and block-on-ring wear tests on superelastic NiTi and found the adhesive wear resistance was superior to steels and other alloys [*148-150*]. But few researchers compared the wear behavior of superelastic materials at different temperatures. Qian *et al.* studied the microscopic wear resistance of SE (superelastic) NiTi using a Berkovich indenter under μN load at various temperatures, which is an abrasive wear condition [*144*]. The wear resistance of NiTi is significantly better in the temperature range around A_f. This temperature dependence of wear resistance was shown in Figure 41. It is clear that at temperatures 50K above A_f=289K the wear performance deteriorated.

2.5.6 Hard Coatings and Interlayers

Hard coatings are widely used to reduce wear in tribo-contacts. Material loss by abrasive wear in tribo-contacts is minimized by using a coating with hardness greater than that of the counterface. Material transfer to the counterface by adhesive interactions and the accompanying material loss may also be reduced. Lubricating the contact, even if it is only boundary lubrication, serves the same purpose.

Chromium nitride (CrN) has a FCC NaCl lattice structure, and exhibits high hardness (~20 GPa), low electrical resistivity (640 $\mu\Omega$·cm) and high melting point (1553K) [*151-158*]. The outstanding properties of CrN have generated practical applications in the protective coating, tribological, and superconductive disciplines. Reactive magnetron sputtering combined with a negative substrate bias is the most common method of making chromium nitride films. Argon gas is normally used as sputter gas and N_2 as the reactive gas. The application of nitride hard coatings on cutting and forming tools has been successfully established over the past decade.

Hard coatings like CrN normally contain a high degree of intrinsic compressive stress owing to lattice distortion and CTE mismatch between coating and substrate. Residual compressive stress in the GPa range is not unusual. The residual stress increases with coating thickness, and thick CrN coatings tend to suffer from premature interfacial failure. It is difficult to produce single-layer nitride coating thicker than 6-7μm without encountering adhesion problems, which limits the expansion of CrN applicability on into other areas.

Diamond-like carbon (DLC) is a metastable form of amorphous carbon containing a significant fraction of sp^3 bonds. It has a high hardness (12-17 GPa), chemical inertness, optical transparency, and it is a wide band gap semiconductor [*159*]. DLC films have widespread applications as protective coatings in areas including optical windows, magnetic storage disks, car parts, biomedical coatings, and micro-electro-mechanical devices. The most common industrial process for deposition of DLC is direct-current or radio-frequency sputtering of a graphite electrode in an Ar plasma. Other methods like ion beam assisted sputter deposition, pulsed laser deposition and cathodic arc deposition are also used. DLC has a hardness around 12-17 GPa, slightly lower than that of CrN. The high compressive stress in DLC also limits the maximum thickness of the coating. DLC coatings are notable for their low friction coefficient compared with other hard coatings [*160-163*]. The friction coefficient of DLC on steel can be below 0.1 without lubrication, close to the friction coefficient of steel on steel with lubrication [*164, 165*].

Interlayers have long been used to boost interfacial adhesion, moderate intrinsic stress and increase performance. For example, the problem of high residual stress in electroplated nickel was overcome by introducing a Cu interlayer [*166-168*]. NiP interlayers were used to increase corrosion resistance and tribological performance of TiN and TiAlN coatings because the porosity of these PVD coatings was sealed off by the NiP interlayer [*169-172*]. Interestingly, the TiAlN/NiP structure on steel drill bits did not meet expectations because NiP can not withstand high impact forces during service, which shows the importance of the mechanical properties of interlayers [*169*].

There is more discussion about interlayers between hard coatings and soft substrates in section 2.6.

2.6 Tribological Study of Hard Coatings on Soft Substrates

2.6.1 Experimental Research

PVD hard coatings on soft lightweight alloy substrates are intended for potential application in machine components in automobile, aerospace and other industries. Here, the tribological system is closed, so that wear debris including coating fragments circulates within the system and can cause severe consequences. The control of wear resistance and coating properties are more stringent for coated machine components. It represents a wider application area and more complicated problem than traditional hard coating:hard substrate system for tool materials.

The economic and engineering significance of hard coating:soft substrate tribological systems is being recognized, leading to a rapidly expanding research literature on this topic since 2000 [*173-196*]. A rich selection of coatings have been applied to aluminum substrates by various methods: nitride coatings by PVD [*181, 185, 191, 194, 196*] and arc ion plating [*174, 176, 183-185, 190*], ferrous coating by thermal spray [*182*], ceramic coating by micro-arc oxidation [*185*], plasma spray [*192*] and Mo-WC coating by laser surface cladding [*189*]. The majority of research efforts are devoted to coating processes and tribological characterization.

Experimental studies offer valuable information and solid support for the hard coating: soft substrate tribological systems. Zhou *et al.* used arc ion plating to deposit TiN and CrN onto 6061 and 7075 aluminum alloy substrates [*183, 184*]. They compared the tribological performances of hard coatings on these two alloy substrates and suggested the substrates' mechanical properties had an influence on the tribological properties. They pointed out that the plastic deformation of substrate during wear tests can cause hard coating fragmentation. Miki *et al.* depositied TiN on aluminum alloy substrates by arc ion plating (AIP) method and an ion beam mixing (IBM) method [*190*]. They focused on the measurement of residual stress in hard coatings using X-ray diffraction. Different residual stress was obtained by altering substrate bias voltage during the deposition process with residual stresses of 2.3 GPa developed at lower N_2 pressures. However they found that wear resistance of nitride coatings was not sensitive to the compressive stress. Kuruppu compared tribological performance of CrN and Cr2N coatings on A2 tool steel, 52100 stainless steel, and 2024 aluminum substrates, with and without Cr interlayers [*194*]. The coated aluminum samples showed slightly lower scratch resistance than hard substrates. Multilayered coatings on aluminum substrates showed better scratch resistance than a single coating structure. The substrate deformation was apparent in some wear tests, but the hard coatings did not wear or delaminate significantly. Murakami and Zhou et al. also investigated a similar problem. But they found single layer CrN on 2024 aluminum substrates has higher scratch resistance than multilayer structures but suffered dramatic coating delamination during

wear tests [*174, 183, 184*].

Xia *et al.* studied diamond-like carbon coated 2024 aluminum alloy samples with four different intermediate layers [*180, 186*]. Results showed that a thicker interlayer improves tribological performance. Specifically, stable friction coefficients for these four samples were nearly same and about 0.1, but the number of sliding cycles giving a stable friction coefficient increased with increasing interlayer thickness. The wear rate of the samples also decreased with increasing interlayer thickness. The same group also investigated gradient layers of DLC/TiN/Ti on nitrogen-implanted 2024 aluminum substrates. The results indicate that the gradient layer shows a gradual change in hardness, compact surface appearance and good tribological properties. Xu et al. used a laser cladding method to coat 2024 aluminum alloys substrates with composite Ti-Al-Fe-B coating [*173*]. The coated samples exhibited improved wear resistance compared to bare aluminum samples. Cain *et al.* investigated TiN coated 6061 aluminum alloy samples for electrical contact resistance improvement [*195*]. These were intended for electromagnetic shields with better corrosion and wear protection, and lower contact resistance at mated contact joints, which is important for contacts which are periodically operated in aggressive environments, such as the doors and access panels on mobile communications facilities used by the military in the field. It was concluded that TiN:Al contacts have significantly lower electrical contact resistance than comparable chromate conversion coatings or bare aluminum alloy contacts, when cycled through several thousand contact closures.

Some general points can be summarized from these studies on hard coating:soft substrates systems.

(1) Hard coatings on aluminum substrates generally exhibit satisfactory interfacial adhesion and scratch resistance, although in some cases poor interfacial adhesion was regarded as the reason for coating delamination during wear tests.

(2) Hard coatings provide wear and scratch resistance to soft substrates as expected. Thick coatings offer better tribological properties than thin coatings.

(3) Substrate deformation occurred during wear and scratch tests, which may contribute to coating failure.

(4) An interlayer can provide better tribological properties, but it depends closely on the process, interlayer properties and thickness.

2.6.2 Theoretical Research

Soft and compliant substrates pose a fundamentally different contact situation than hard and stiff substrates. A hard and stiff substrate does require a hard coating for abrasion resistance. The purpose of the coating is to guard against diffusive material transport under sliding contact conditions. The soft and compliant substrates have a lower load bearing capacity, which can partly be compensated in design by limiting contact stresses. However it is necessary to compare the differences in contact stress between coated hard substrates and soft substrates, to understand the benefits and

limitations of soft substrates. So far theoretical research on this problem lags in comparison with numerous experimental studies.

Souza *et al.* used finite element analysis to model spherical indentation on TiN and SiC coated 6061 aluminum substrates [*179, 188*]. They focused on circular crack patterns in hard coatings on soft substrates generated during spherical indentation, and compared modeling with experiments [*188*]. The number and location of circular cracks was found to be related to several factors: overall contact geometry, the friction coefficient between coating and indenter, the modulus mismatch between coating and substrate, the level of residual stress and coating fracture toughness. Another study attempted to relate pile-up from spherical indentation in TiN:Al with plastic strain [*179*], but without much success. The relation between pile-up and plastic strain is an important topic in instrumented indentation. These could have been more informative studies if the authors had shifted their attention to comparison of the contact stress situations of hard coating on soft substrates and hard substrates.

Ramalingam *et al.* used the displacement formulation method to compare the elastic contact stresses at the interface between coatings and substrates [*197, 198*]. It is found that stiff (high modulus) substrates and compliant (low modulus) substrates contribute to a quite different stress condition. Different loading conditions are also considered: normal point load (Figure 42), shear point load (Figure 43), normal strip load and shear strip load. Point loading represents the concentrated contact loading where stress and strain is localized, while strip load is the distributed contact loading over a length scale an

order of magnitude larger than the coating thickness. Results are summarized in the following table, which are compared to the case with stiff (high modulus) substrates.

Normal line load (Figure 42 and Figure 43)	• Displacements are distributed in compliant substrates over larger lateral dimensions than in stiff substrates. It is good for compliant substrates because the strain gradient is smaller. • The maximum normal bearing stress σ_y at coating:substrate interface is lower in compliant substrates; the maximum interfacial shear stress τ_{xy} is also lower in compliant substrates. It is good for compliant substrates because it is beneficial for coating adhesion. • The interfacial tensile stress σ_x is higher in compliant substrates, but can be lowered by increasing coating thickness. It is good for compliant substrates because increasing coating thickness could have a beneficial effect.
Shear Line Load	• Displacements are distributed in compliant substrates over larger lateral dimensions than in stiff substrates. It is good for compliant substrates.

	• Interfacial shear stress τ_{xy} is lower in compliant substrates; interfacial tensile stress σ_x is higher in compliant substrates than in stiff substrates. It is good for compliant substrates. • Stiff substrates have a higher positive σ_y, which tends to lift the coating from substrates, while σ_y is moderated in compliant substrates. It is good for compliant substrates because it is beneficial for coating adhesion.
Normal Strip Load (contact length≈10 times coating thickness)	• σ_x becomes compressive instead of tensile, regardless of substrates modulus. σ_x is more compressive in compliant substrates than in stiff substrates. It is not good for compliant substrates.
Shear Strip Load	• Higher tensile stress σ_x at coating:substrate interface in compliant substrates. It is not good for compliant substrates • Lower lifting stress σ_y in compliant substrates. It is good for coating adhesion on compliant substrates.

Bilayer composite structures, which involve an interlayer between a stiff coating and the substrate, have also been considered [*197*]. It was found that an interlayer reduced the maximum tensile stress σ_x up to 75%. Decreases in interfacial tensile stress are

accompanied by increases in shear and bearing stresses at the interface, but the rate of increase is low. For shear traction, similar but smaller gains in reducing tensile stresses are obtained with stiff interlayers. The lift-off (positive) σ_y is enhanced by introduction of an interlayer. The authors suggested even a thin interlayer can be helpful in lowering the maximum film tensile stress in heavily loaded conditions. Tensile and shear stresses are affected more strongly than the bearing or lifting stresses.

The Ramalingam study showed that there were both advantages and disadvantages of compliant substrates as support structures compared with stiff substrates. But since only elastic contact was considered, the plastic deformation on both soft and compliant substrates encountered during experimental research still posed a major problem. Introduction of an interlayer has the positive effect of reducing interfacial stress. Experimental research has also pointed to this direction.

2.6.3 Preliminary Study of CrN:NiTi:Al Tribological System

Bulk SE NiTi has shown excellent wear resistance [*134-144*]. The wear and scratch track in martensitic NiTi also showed recovery after austenite phase transformation [*2*]. This corresponds to the indentation-induced shape memory and superelastic effect discussed in 2.5.3. However the high cost of NiTi alloy production and processing would inhibit its tribological application. What is an economic and versatile way to utilize the tribological advantages of NiTi shape memory alloy? The NiTi interlayer

approach may well be the right answer. Ni *et al.* studied the tribological performances of CrN:NiTi:Al tribological systems, where CrN is nitride hard coating, NiTi is the interlayer, and 6061 aluminum alloy is the substrate [*1-3*]. It was found that a SE NiTi interlayer greatly improves the wear resistance compared to SMA NiTi or Cr interlayers (Figure 44). In scratch tests, the CrN coating shows no delamination with SE NiTi interlayer, while severe damage in CrN coating without NiTi interlayer was obvious Figure 45.

These studies provided no systematic information on how the evolution of martensite-austenite phase transformations affects tribological performance. This knowledge can only be obtained from wear and scratch tests carried out over the complete transformation temperature range. Another key problem is how coating:interlayer thickness ratio affects tribological performance. The residual stress of CrN coating and NiTi interlayer interact with each other, and with contact stresses during tribological loading. Residual stresses also tend to increase with coating and interlayer thickness. Detailed knowledge of this problem can be obtained from tribological tests over a matrix of coating:interlayer thickness ratios, and over a temperature range that covers the phase transformation temperatures.

2.7 Constitutive Modeling of Shape Memory Effect

2.7.1 One dimensional Constitutive Model of SME

Computational modeling of the shape memory effect has been developed with increasing applications of shape memory alloys. The macroscopic mechanical behavior of shape memory alloys is usually modeled following either a phenomenological or a micromechanical approach. One-dimensional phenomenological models are suitable for engineering practice, because they make use of measurable quantities as parameters and are often computationally efficient to implement. Uniaxial phenomenological models have been proposed by many researchers: Tanaka and Nagaki [*199*], Liang and Rogers [*200*], Ivshin and Pence [*201-203*], and Brinson and Huang [*204*], Boyd and Lagoudas [*205, 206*]. The main factor distinguishing these one-dimensional models is the particular kinetics governing phase transformations. Because the transformation strain is large compared to the elastic strain, the phenomenological transformational kinetics play a significant role.

The micromechanics approach tries in various ways to follow very closely the crystallography, using thermodynamics to describe the phase transformation [*207-211*]. These models often consider martensite variants as transforming inclusions and use micromechanics to calculate the interaction energy due to the phase transformation. Stresses and strains are obtained as volume averages in which many possible martensite variants are included. The micromechanical models are much more complicated than phenomenological models and are computationally demanding. But based more closely

on physical metallurgy, these models may yield a more accurate constitutive law.

One-dimensional phenomenological models start with how to model the mixture of martensite and austenite phases. Both parallel (Figure 46) and series (Figure 47) approaches can be adopted [*204*]. In the parallel model, the relationship between stress and strain is expressed as:

$$\sigma = (1-\xi)\sigma_A + \xi \cdot \sigma_M$$
$$\sigma_M = E_M(\varepsilon - \xi\delta), \sigma_A = E_A(\varepsilon - \xi\delta)$$
$$\sigma = (\xi \cdot E_M + (1-\xi) \cdot E_A)(\varepsilon - \xi\delta)$$

In the series model, it is:

$$\varepsilon = \xi\varepsilon_M + (1-\xi)\varepsilon_A$$
$$\varepsilon_M = \delta + \frac{\sigma}{E_M}, \varepsilon_A = \frac{\sigma}{E_A}$$
$$\sigma = \frac{(\varepsilon - \xi\delta)}{(\frac{\xi}{E_M} + \frac{1-\xi}{E_A})}$$

where ε_M, σ_M and ε_A, σ_A are the strain and stress contribution from the martensite phase and austenite phases, respectively. The σ and ε are the total stress and strain. The ξ is the martensite volume fraction, and δ is the phase transformation strain. E_M and E_A are the modulus of martensite and austenite phases.

As pointed out by Brinson and Huang [*204*], the key difference between various constitutive models of shape memory materials is the kinetic equations governing the phase transformations. The kinetic equation specifies how the martensite volume fraction changes with stress, temperature, and loading history. For instance, in the Boyd-Lagoudas model [*205, 206*], the kinetic equation takes the form of exponential

function:

$$\xi = 1 - \exp[a^M (M_S - T) + b^M \sigma]$$

$$\text{where } a^M = \frac{\ln(.01)}{(M_S - M_f)}, b^M = \frac{a^M}{C_M}.$$

The three-dimensional model developed in the present work is based on the one-dimensional Ivshin-Pence model [*201, 202*], whose kinetic equation is more complex.

2.7.2 One-dimensional Ivshin-Pence Model

The Ivshin-Pence model is a one-dimensional phenomenological model of shape memory effects. The transformation kinetics were carefully constructed to capture various aspects of the shape memory effect.

The shape memory alloy is treated as homogenous mixture of martensite and austenite phases. The total strain ε is expressed as:

$$\varepsilon = (1 - \alpha)\varepsilon_M + \alpha\varepsilon_A,$$

where ε_M and ε_A are the strain contributions from martensite phase and austenite phase. The variable α is the austenite volume fraction, used in the Ivshin-Pence model instead of the martensite volume fraction ξ. The variable ε_A is purely elastic but ε_M has both an elastic component ($\frac{\sigma}{E_M}$) and transformational component (δ):

$$\varepsilon_A = \frac{\sigma}{E_A},\ \varepsilon_M = \frac{\sigma}{E_M} + \delta .$$

What distinguishes the Ivshin-Pence model from other 1D constitutive models is its transformation kinetics that govern the hysteresis exhibited by the austenite phase fraction α.

The rate form for the austenite volume fraction is:

$$\frac{d\alpha}{dt} = \left\{ \frac{\alpha(t_K)}{\alpha_{\max}(\beta(T(t_K),\sigma(t_K)))} \right\} \frac{d\alpha_{\max}}{d\beta} \left(\frac{\partial\beta}{\partial T}\frac{\partial T}{\partial t} + \frac{\partial\beta}{\partial\sigma}\frac{d\sigma}{dt} \right), \frac{d\alpha}{dt} \le 0$$

$$\frac{d\alpha}{dt} = \left\{ \frac{1-\alpha(t_K)}{1-\alpha_{\min}(\beta(T(t_K),\sigma(t_K)))} \right\} \frac{d\alpha_{\min}}{d\beta} \left(\frac{\partial\beta}{\partial T}\frac{\partial T}{\partial t} + \frac{\partial\beta}{\partial\sigma}\frac{d\sigma}{dt} \right), \frac{d\alpha}{dt} \ge 0 \quad ,$$

where β characterizes neutrality curves that is a function of stress and temperature but do not involve hysteresis of phase transformations. The austenite volume fraction α is an explicit function of β. The variables $\alpha_{\max}$ and $\alpha_{\min}$ are envelope functions describing the outermost hysteresis behavior for the martensite phase transformation and the reverse austenite phase transformation, respectively. The variable t_K is the previous time when the transformation directions switch.

$\beta(T,\sigma)$ is a function of temperature and stress which characterize the driving force of phase transformations:

$$\beta(T,\sigma) = T + \frac{1}{\left(S_A^0 - S_M^0\right)} \left\{ \frac{\left(E_M - E_A\right)}{2E_M E_A}\sigma^2 - \delta\sigma \right\}.$$

where S_A^0 and S_M^0 a re the specific entropies of the austenite and martensite phases at reference temperature, E_M and E_A are the Young's modulus of the respective martensite and austenite phase, and δ is the martensite phase transformation strain.

The envelope functions can take various forms. The following form is used by the original authors and also in this study:

$$\alpha_{\max} = 0.5 + 0.5\tanh(k_1\beta + k_2)$$
$$\alpha_{\min} = 0.5 + 0.5\tanh(k_3\beta + k_4)$$

The austenite volume fraction α can be integrated using α_{max} and α_{min}:

$$\frac{d\alpha}{dt} = \left\{\frac{\alpha(t_K)}{\alpha_{\max}(\beta(T(t_K),\sigma(t_K)))}\right\}\frac{d\alpha_{\max}}{d\beta}\left(\frac{\partial\beta}{\partial T}\frac{\partial T}{\partial t} + \frac{\partial\beta}{\partial\sigma}\frac{d\sigma}{dt}\right), \frac{d\alpha}{dt} \le 0$$
$$\frac{d\alpha}{dt} = \left\{\frac{1-\alpha(t_K)}{1-\alpha_{\min}(\beta(T(t_K),\sigma(t_K)))}\right\}\frac{d\alpha_{\min}}{d\beta}\left(\frac{\partial\beta}{\partial T}\frac{\partial T}{\partial t} + \frac{\partial\beta}{\partial\sigma}\frac{d\sigma}{dt}\right), \frac{d\alpha}{dt} \ge 0$$

The k parameters are determined by the phase transformation temperatures:

$$\alpha_{\max}(\beta(M_f,0)) = \alpha_{\min}(\beta(A_s,0)) = \psi,$$
$$\alpha_{\max}(\beta(M_s,0)) = \alpha_{\min}(\beta(A_f,0)) = 1-\psi\text{'}$$

The parameter ψ is an arbitrary small number because $\psi = 0$ is a numerical singularity. In Ivshin-Pence model , $\psi = 0.02$ is used [*201, 202*].

2.7.3 Three Dimensional Constitutive Models of SME

A number of three-dimensional constitutive models have been proposed based on existing one-dimensional models. For phenomenological models, the expansion from one to three dimensions is based on generalized plasticity theory, assuming the martensite-austenite phase transformation also holds for the assumptions of classical plasticity theory. These assumptions are: 1) yield stress is insensitive to hydrostatic stress; 2) inelastic deformation due to the shape memory effect, like plastic deformation,

is volume conserving; 3) the plastic strain increment in each direction is proportional to the stress deviator component in that direction.

Current three-dimensional constitutive models of SME do not have enough experimental support from multidirectional loading [*212-217*]. Only one-dimensional models are well calibrated with uniaxial experimental data that is more readily available. The unique behavior of indentation-induced SME may thus be a suitable proving ground for three dimensional models. Modeling of indentation-induced SME also offers better understanding of complex SME under contact loading conditions.

Lubliner and Auricchio *et al.* proposed a framework of three dimensional constitutive model of shape memory effect based on generalized plasticity [*217*]. Generalized plasticity is an internal-variable model of rate-independent inelasticity that includes conventional or classical plasticity as a special case. It was developed in order to account for the behavior of elastic-plastic solids in which, following initial plastic loading and elastic unloading, the reloading is not necessarily elastic up to the state at which unloading began; such solids include graphite, some stainless steels and some minerals. The model is based on some fundamental axioms and on results from elementary set theory and topology, which makes it also applicable to other mechanical behavior like shape memory effect.

In the case of shape memory effect, the transformation strain rate tensor ε_{ij}^{T} was determined by:

$$\dot{\varepsilon}_{ij}^{T} = \dot{\lambda}(\frac{\sqrt{3}}{2\sqrt{J_2}} S_{ij}),$$

where S_{ij} was the deviator stress, J_2 the second invariant of stress, and λ is the effective transformation (inelastic) strain, whose rate form was determined by the kinetics of martensite-austenite phase transformations.

2.8 Summary

This chapter has briefly reviewed recent work in various research areas involved in this dissertation. The literature on shape memory alloys, shape memory and superelastic effect, contact mechanics, and constitutive modeling of shape memory materials is very extensive. It is difficult to cover these topics completely in this chapter. More attention is given to the superelastic effect, the Clausius-Clapeyron equation, and the Ivshin-Pence constitutive model due to their importance in this work.

Although there is also abundant literature on two-way shape memory effect, most of them are focused on training methods instead of reaching deep into the mechanism of the two-way shape memory effects. The few that focused on the mechanism and were well recognized were reviewed. There presently exists no literature about two-way shape memory effects from training methods involving indentation.

For hard coatings on soft and compliant substrates, more and more research papers have been published in recent years, reflecting a growing interest in these tribological

systems. The majority are devoted to coating deposition and tribological tests. Very few concern mechanics and modeling. Both experimental and theoretical work on this tribological system has been reviewed.

Chapter 3

Methods and Materials

3.1 Tribological Study

3.1.1 Substrate Materials

Both M2 tool steel and 6061 T6 aluminum alloy* were used as substrate materials. The M2 tool steel was supplied by Crucible Service Center (Syracuse, N.Y.). The 6061 T6 aluminum was supplied by United Aluminum Corp. (North Haven, C.T.)

Two mm thick M2 steel plates were cut into 25 mm×25 mm square pieces by electrical discharge machining. The steel substrates were polished to 50 nm surface roughness with 0.25 μm grit size diamond paste. The surface roughness was measured by optical surface profilometer. The samples were cleaned ultrasonically in acetone and then in methanol for 10 minutes before being introduced into the deposition chamber. 3mm thick 6061 T6 aluminum alloy plates were cut into 30mm×30mm square pieces and then mechanically polished to 50-70nm surface roughness using 0.05 μm grit size alumina suspension. The polished aluminum substrates were then cleaned with acetone and methanol.

* The T6 temper in the as-supplied material was later changed by processing.

3.1.2 NiTi Interlayer and Hard Coating Deposition

NiTi thin films were deposited by DC magnetron sputter deposition. The sputter cathode compositions were $Ni_{46.5}Ti_{53.5}$, $Ni_{48}Ti_{52}$, and $Ni_{38.5}Ti_{53.5}Cu_8$ (atomic percentage) for various experiments. The thin films compositions was $Ni_{48.3}Ti_{51.7}$, $Ni_{51.8}Ti_{48.2}$ and $Ti_{51.7}Ni_{42.2}Cu_{6.1}$ respectively, measured using a wet chemical analysis (the materials were dissolved with nitric and hydrofluoric acid and measurements were made by inductively coupled plasma optical emission microscopy by Wangyang Ni at GM R&D Center [*218*]). The detailed deposition parameters are listed in Table 3 through Table 6.

For samples intended for later diamond-like carbon (DLC) deposition, a Cr layer of 0.3 μm thick was deposited onto NiTi interlayers in the same chamber, without breaking vacuum. The purpose was to insulate the NiTi interlayer from contamination.

The thicknesses of deposited films were measured by the spherical abrasion method (CALOTEST, CSM Instruments SA)[†], and Wyko NT surface profilometer at film edges produced by masking. The surface roughness of the deposited thin films was measured to be 35±10 nm with a Wyko NT surface profilometer.

The NiTi:Al samples were then transferred to a TEER UDP 550 unbalanced magnetron sputter system for deposition of the hard coatings. Surfaces were sputter-cleaned for 600 seconds before deposition of CrN, and 3.6 ks before deposition of DLC.

[†] A rotating steel sphere wears through the coating, which gives a rim and then into the substrate which gives a crate. Coating thickness is determined from the diameters of the rim and the crate, measured optically. More details may be found at http://www.csm-instruments.com

400 V was applied to the samples during sputter cleaning. CrN coatings were deposited on both M2 steel and 6061 T6 aluminum substrates, with and without NiTi interlayers. DLC coatings were only deposited on the aluminum substrates with and without NiTi interlayers. A Cr layer of 0.1μm thickness was deposited before the deposition of CrN and DLC to facilitate bonding, which was indispensable for CrN and DLC coatings deposition.

CrN coatings were deposited by sputtering two chromium targets of 99.99% purity in a nitrogen- containing argon environment. Argon of 99.999% purity was used as the sputtering gas. The base pressure of the system was 8×10^{-4} Pa and the working partial Ar pressure was 0.13 Pa. The partial pressure of nitrogen was 0.13 Pa. The deposition power was 600W with 4 A at 150 V. The DLC coating was deposited by sputtering from one chromium and two graphite targets. The base pressure was 1.33×10^{-4} Pa and working Ar pressure was 0.13 Pa. The deposition power was 525 W with 3.5 A at 150 V.

NiTi interlayer and CrN layer thicknesses were measured at masked thin film edges by a surface profilometer. CrN and DLC coatings were also deposited onto reference aluminum and steel substrates without NiTi interlayers. Reference samples went through one same thermal history so that the hardness of the substrates was the same as the samples with a NiTi interlayer. The hardness of the as-received 6061 T6 aluminum alloy was 94 HRE (62 HRB), which dropped to 21 HRE after deposition of NiTi interlayers and CrN coatings.

3.1.3 Special Treatments of DLC:NiTi Interfaces

Special treatments were given to create a strong DLC:NiTi interface, because the CrN:NiTi interface was found to be weaker than desired during scratch tests. A 0.3 μm Cr layer was deposited onto NiTi interlayers after the deposition and annealing process, without breaking vacuum. The Cr layers shields the NiTi interlayers from any potential contamination. After the samples were set into the TEER deposition system, the Cr layers were subjected to 3.6 ks sputter cleaning. It had been calibrated that the 3.6 ks sputter cleaning would remove about 0.1 μm Cr layer. As a result, about 0.2 μm thick Cr layers still remain on the NiTi interlayers. Before the DLC deposition, another 0.1 μm thick Cr layer was deposited onto the sputter cleaned Cr surfaces. Thus, the DLC coatings and NiTi interlayers connected at the Cr-Cr interface, while the CrN coating and NiTi interlayers had a Cr-NiTi interface.

3.1.4 Characterization of NiTi Interlayer Properties

The phase transformation temperatures of NiTi interlayers on aluminum and steel substrates were estimated using temperature scanning X-ray diffraction (XRD). For room temperature martensitic NiTi interlayers, the measurement was carried out on a Scintag 2000 diffractometer (Cu Kα radiation) using a thermoelectric module for heating. The temperature of the NiTi interlayer was measured by a K-type thermocouple that was adhered to the interlayer surface. An XRD scan was taken after each designated

temperature was stabilized. Room temperature austenitic NiTi interlayers needed a special cooling stage to reach sub-ambient temperature. The thermoelectric cooler was not capable of reaching steady state below 283K. Therefore additional measurements were carried out on a Rigaku AFC6S (Cu Kα radiation) diffractometer with a low temperature sample stage which was cooled by liquid nitrogen. Since the thin films were attached to the substrates during the temperature controlled XRD measurements, the measured transformation temperatures included the effects of residual stresses in the thin films. Results of temperature scanning XRD shown in Figure 48 shows that room temperature martensitic NiTi on steel substrates has A_f 350±5K and *Ms* (the martensite start temperature) 310±5K. Figure 49 shows that room temperature austenitic NiTi has A_f 310K±5K and *Ms* 270±5K. The results of NiTi:Al samples are shown in Figure 50, Figure 51 and Figure 52.

The phase transformation stress of NiTi thin films on aluminum substrates was measured by the wafer curvature scanning method, which is based on the Stoney equation [*58, 60, 219*]. The surface reflectivity of DLC and CrN hard coatings are not good enough for laser scanning stress measurement, but good enough for optical profilometer. The optical profilometer can also measure curvature over longer length, which is more than 20mm. Longer length provides more accurate curvature measurement. However the laser scanning stress measurement is capable of providing real time stress measurement vs. changing temperature, from which residual stress evolution can be

obtained. The optical profilometer method can only take "snap-shot" of the curvature at certain stable temperature. This first-order approximation is valid for $t_c < t_s/100$.

The Stoney equation calculates the stress σ_c in the thin film:

$$\sigma_c = \frac{E_s t_s^2}{6t_c} K,$$

where E_c is the biaxial modulus of the substrate, t_c and t_s are the thicknesses of thin film and substrate, respectively. K is the curvature of thin film:substrate bilayer, which is measured by the laser scanning method.

The aluminum substrates that supported NiTi thin films were plastically deformed during thin film deposition and annealing by the intrinsic residual stress in the NiTi thin film (section 4.1.1). As a result the total curvature measured was not caused entirely by the residual stress in the NiTi thin film. Part of the curvature came from plastic deformation of the aluminum substrates. However the Stoney equation is still valid for measuring the relative residual stress change in the NiTi thin film. Let $K_{plastic}$ be the curvature from plastic deformation; K_1 and K_2 are total curvatures measured at two different temperatures; σ_c^1 and σ_c^2 are the residual stresses in the NiTi thin films at two different temperatures:

$$\sigma_c^1 = \frac{E_s t_s^2}{6t_c}(K_1 - K_{plastic})$$

$$\sigma_c^2 = \frac{E_s t_s^2}{6t_c}(K_2 - K_{plastic})$$

The change in residual stress $\Delta\sigma_1^2 = \sigma_c^2 - \sigma_c^1$ between two temperatures can be

calculated by Stoney equation:

$$\Delta\sigma_1^2 = \sigma_c^2 - \sigma_c^1 = \frac{E_s t_s^2}{6t_c}(K_2 - K_1).$$

A resistance-heating furnace was used to heat the samples, which were placed on the surface of the heater type thermocouple was inserted in a tight-fitting hole on the side of the furnace. Because the thermocouple did not contact the samples, actual temperature could have been lower than the measured temperatures.

The CrN hardness and elastic modulus were 20±2GPa and 200±20GPa, measured from nine indentation tests at different locations on the coating; the DLC hardness and modulus were 10±1GPa and 160±20GPa; both were measured by nanoindentation on Nano Indenter XP (MTS Systems Corp.).

Temperature scanning indentations were also done on NiTi interlayers on steel substrates to verify indentational superelasticity at elevated temperatures. The indentation experiments were carried out on a Micro Materials (Wrexham, U.K.) Nano Test 600 system with a Berkovich diamond indenter. The samples were immersed in liquid nitrogen for 10 minutes before experiments to obtain a fully martensite phase in the interlayers. The indenter and substrate holder had resistance-heating ability. The temperature at the indenter and sample surface was measured by two thermocouples and controlled by independent temperature controllers. After the designated temperature was reached the experimental set-up was left overnight to reach thermal equilibrium and minimize thermal drift. The highest temperature used was 473K, far below the typical

aging temperature of 773 K for NiTi. As a result, the microstructure and mechanical properties of thin films are not expected to change by the heating step. The maximum load was set at 25 N so that the indentation depth would not exceed 10% of the film thickness in order to minimize the substrate influence on the indentation response of the films. The indentation speed was 5 nm/s, which was small enough to minimize any dynamic effects. Load-depth curves are shown in Figure 53.

3.1.5 Tribological Testing Methods

Scratch and wear tests were used to evaluate tribological performance. The scratch tests were performed on a Micro-Scratch Tester (CSM Instruments SA), which can also record acoustic emissions from the scratch. A 107 μm tip radius conical diamond indenter was used as the scratcher. (Conical indenters actually have a small-radius spherical tip.) If the indent or scratch dimension was small compared to the radius of the spherical tip, the conical indenter functions as a spherical indenter. A thermoelectric cooler heated the samples from below and the sample's surface temperature was measured by attaching a thermocouple.

The wear tests were performed on an ISC-200 Tribometer (Implant Sciences Corp.) equipped with heating sample holder. The wear counterpart was a 200 μm tip radius diamond spherical indenter under 0.49 N and 0.98 N loads, and a 3.175mm radius WC

ball under 0.98N, 1N and 5N loads. The geometry of the wear tracks and scratch tracks were characterized by Wyko NT surface profilometer and an Hitachi SC-2500C SEM.

The measurement of wear rate was made according to ASTM standard G 99 pin-on-disk wear test [*220*]:

$$\text{Wear Rate} = \frac{\text{Volume of the Wear Track}}{\text{Total moving distance of the Ball}}$$

Volume of the Wear Track=(Cross-sectional area) × (Circumference)

Total moving distance of the Ball = (Number of Total circles) × (Circumference)

3.2 Training and Characterization of The Two-way Shape Memory Effect

Both bulk NiTi and thin film NiTi SMAs were used in the two-way shape memory study. The bulk NiTi metal was purchased from Special Metals Corp. (New Hartford, New York). The nominal composition was $Ni_{50.31}$ $Ti_{49.69}$. The phase transformation temperatures were measured by differential scanning calorimetry using TA Instruments modulated 2920 DSC. The DSC scanning curves are presented in Figure 32. The phase transformation temperatures were: A_s =350K, A_f=404K; M_s =344K, and M_f =287K.

The as-received material was electrical-discharge machined to small pieces with dimensions of 2.45cm×2.45cm×1cm. Surface roughness was reduced to 0.05μm in three steps of mechanical polishing using 3, 1, and 0.5μm grit size diamond paste.

The NiTi thin films were sputter-deposited on to a (100) silicon wafer at 673K in 45

minutes, followed by annealing at 773K for 3.6ks. The film thickness was measured to be 4.5μm. The chemical composition was $Ni_{48.3}$ $Ti_{51.7}$ by wet chemical analysis. The phase transformation temperatures, A_S =343K, A_f=390K; M_S =329K, and M_f=282K, were estimated by the temperature scanning wafer curvature method

A simple "ball-and-clamp" method (Figure 54) was used to induce cyclic thermomechanical training to the NiTi sample. The NiTi sample was first cooled in liquid nitrogen for 5 min to ensure fully martensitic structure. A 3.175 mm diameter tungsten carbide ball was then clamped into the sample using a steel c-clamp with a fixed number of rotations of the clamping screw. The indentation depth was 170μm measured by an optical surface profilometer. The representative strain was about 9%. The whole fixture was then placed in a resistance-heating oven for 2 minutes to reach 423±10K. Afterwards, it was quenched into ice water for another 2 minutes, which concluded one training cycle. A total of 30 training cycles were performed. Since the number of rotations of the c-clamp screw is kept the same during the training procedure, the thermomechanical training is considered under a constant strain condition.

The profile of indents was measured using Wyko NT optical surface profilometer. A thermoelectric cooler (Marlow Industries Inc., Dallas, Texas) was placed below the sample for heating and cooling. A thermocouple was taped onto the side of the sample to measure one temperature. The profiles of the indents were taken after the sample was heated to 400±5K and measured again after the sample was cooled to 300±3K. During the process the position of the sample was kept the same.

Another training method, using a single-cycle deformation approach, was carried out by the following procedures. A 3×3 matrix of spherical indents was created on the bulk sample surface using a 1.59 mm diameter steel ball indenter under a 100kg load. Also a scratch was made with a 107μm tip radius spherical indenter under 15N load, and nanoindents were created on the NiTi thin films by a 10μm tip radius spherical diamond indenter using a Nano XP indenter (MTS). Before indentation, the samples were cooled in liquid nitrogen for 5min to ensure a fully martensitic structure. The samples were then heated to 423K on a hot plate for 10min to let the spherical indents recover, i.e., transform from the martensite to austenite. They were cooled again in liquid nitrogen for 5 min. The profiles of the indents and scratches were measured using a Wyko NT optical surface profilometer (Veeco Instruments, Inc.). A thermoelectric device (Marlow Industries, Inc.) was placed below the sample for heating and cooling. A thermocouple was taped to the back side of the sample to measure temperature. The profiles of the indents were taken after the sample was heated to 400±2K and taken again after it was cooled to 300±2K.

The residual indents and scratches on the bulk NiTi were removed by mechanical polishing: first using 240, 400 and 600 grit size silicon carbide grinding paper, and then with 6 μm and 1 μm grit diamond paste. The indents on the surface of NiTi thin film were polished using 0.05μm alumina suspensions. The profiles of surface protrusions were then measured using the Wyko surface profilometer together with the thermoelectric device for heating and cooling.

In the layered planarization experiment, the depth of successively polished layers was measured by comparing of the thicknesses of the polished NiTi sample and a reference sample, using optical surface profiler.

3.3 Finite Element Modeling of Spherical Indentation on Superelastic NiTi

Spherical indentation-induced superelasticity in NiTi was simulated in FEA and compared to the results of experiments, including load-displacement curves and recovery ratios. A three dimensional constitutive model is developed based on the one-dimensional Ivshin-Pence constitutive model [*202, 203*] and generalized plasticity theory [*217*], to describe the shape memory effect under contact loading conditions. Details can be found in section 2.7. The von-Mises slip-plasticity is also included in this model to capture the mechanical response of NiTi SMA in large deformation. Implementation of the model in a commercial finite element program (ABAQUS) is done by writing a user material subroutine.

3.3.1 Formulation of Three-dimensional Constitutive Model

First the 3D constitutive model is presented in terms of total strain rate $\dot{\varepsilon}_{ij}$. This total strain rate is decomposed into elastic part $\dot{\varepsilon}_{ij}^{E}$ and a transformation strain (inelastic) part $\dot{\varepsilon}_{ij}^{T}$:

$$\dot{\varepsilon}_{ij} = \dot{\varepsilon}_{ij}^{T} + \dot{\varepsilon}_{ij}^{E}, \quad (1)$$

Both the martensite phase (with volume fraction ξ) and austenite phase (with volume fraction α) contribute to the elastic response, with $\xi + \alpha = 1$. The elastic strain rate is:

$$\dot{\varepsilon}_{ij}^{E} = E_{ijkl}^{-1} \dot{\sigma}_{kl}$$

$$E_{ijkl}^{-1} = (1-\alpha) E_{M,ijkl}^{-1} + \alpha E_{A,ijkl}^{-1}, \quad (2)$$

where $E_{M,ijkl}^{-1}$, $E_{A,ijkl}^{-1}$ are the respective stiffness tensor for martensite and austenite phase, respectively.

For superelastic behavior, the transformational strain is dominant. The simplification that $E_{M,ijkl} = E_{A,ijkl} = E_{ijkl}$ can be made so that:

$$\dot{\varepsilon}_{ij}^{E} = E_{ijkl}^{-1} \dot{\sigma}_{kl}, \quad (3)$$

The E_{ijkl}^{-1} is represented in terms of Young's modulus E and Poisson's ratio υ.

If loading a tensile specimen of superelastic NiTi to 6% total strain using 400MPa tensile stress, it is assumed that 80% of the structure is stress induced martensitic phase. Without the simplification, the elastic strain is:

$$\varepsilon^E = 20\%\frac{400MPa}{80GPa} + 80\%\frac{400MPa}{30GPa} = 1.1\%.$$

With the simplification that $E_{M,ijkl} = E_{A,ijkl} = E_{ijkl}$, the elastic strain is

$$\varepsilon^E = \frac{400MPa}{80GPa} = 0.5\%.$$

There is 1.1%-0.5% = 0.6% difference in the elastic strain. This difference is 10% of the 6% total strain. So the simplification causes about 10% difference in the model's behavior.

Lubliner and Auricchio proposed a 3D frame work of the shape memory effect based on the generalized plasticity theory [*217*]. The transformation strain rate is determined by:

$$\dot{\varepsilon}_{ij}^{T} = \dot{\lambda}\left(\frac{\sqrt{3}}{2\sqrt{J_2}}S_{ij}\right), \qquad (4)$$

where S_{ij} is the deviator stress, J_2 the second invariant of stress, and λ the effective transformation (inelastic) strain, whose rate form is determined by the austenite volume fraction rate:

$$\dot{\lambda} = -\delta\dot{\alpha}. \qquad (5)$$

Here α is again the austenite volume fraction, whereas δ is a material constant that gives the maximum transformation strain that can be induced by the shape memory effect. This maximum transformation strain δ follows from crystallographic considerations and is typically about 5%. The austenite volume fraction $\alpha = \alpha(x,t)$ is a material dependant function of current von Mises stress and the overall loading history.

The α value is calculated using the Ivshin and Pence constitutive model. Combining the elastic part and transformation part, the complete strain rate was expressed as:

$$\dot{\varepsilon}_{ij} = -\delta \dot{\alpha}(\frac{\sqrt{3}}{2\sqrt{J_2}} S_{ij}) + E^{-1}_{ijkl} \dot{\sigma}_{kl} \qquad (6)$$

This constitutive relation between stress and strain is strictly in accordance with classical von Mises plasticity theory. The assumptions and limitations of the classical plasticity theory, like insensitivity to hydrostatic pressure and tension-compression asymmetry, were also implied in the model. Experimental results showed some shape memory materials had tension-compression asymmetry [77], and the phase transformation behavior shifted with elevating hydrostatic pressure [*221, 222*]. Inclusion of these factors into the current model will be the topic of future studies.

3.3.2 Formulation of Slip Plasticity

Slip plasticity dominates the deformation of SE NiTi if stress-induced martensite phase transformation is exhausted as the dominant deformation mechanism. Indentation usually involved strains larger than 7 %. Plasticity was thus necessary to be included in the constitutive model for indentation modeling. A simple but effective algorithm is used in this constitutive model to shift the deformation mechanism from superelasticity to von Mises plasticity where ever the austenite volume fraction has decreased to 5 % (95 % transformed from austenite to martensite). At this threshold superelasticity is replaced

by von Mises plasticity as the mechanism of plastic deformation. The strain rate is still decomposed in the same way as equation (1) with the elastic part expressed as equation (3) and inelastic part as (4). Equation (5) is replaced by an alternative expression so as to model von Mises plasticity with isotropic hardening. The complete form of equation (5) is expresses as:

$$\dot{\lambda} = \begin{cases} \dfrac{1}{h}\dfrac{\sqrt{3}}{2\sqrt{J_2}} S_{ij}\dot{\sigma}_{ij}, & (\alpha \le 0.05,\ \text{von Mises plasticity}) \\ -\delta\dot{\alpha}, & (\alpha > 0.05,\ \text{superelasticity}) \end{cases}, \quad (7)$$

where h is the plastic hardening slope.

After the superelastic constitutive model is switched to the slip-plasticity model, α is taken as fixed. The plastic strain continues to change according to equation (7) as long as the plastic loading is in effect while $\dot{J}_2 > 0$. The von Mises stress and plastic strain is increasing as plastic deformation proceeded.

Unloading occurs when $\dot{J}_2 < 0$. Initial unloading from the plastic deformation stage is elastic until the von Mises stress returns to the value associated with the previous transition from superelasticity to slip plasticity. Further unloading is governed by the constitutive model of superelasticity where the austenite volume fraction increases ($\dot{\alpha} > 0$).

The constitutive model is implemented in ABAQUS finite element program by customizing the user material subroutine. It is first tested under simple loading conditions of uniaxial tension, biaxial compression and shear. The stress-strain curves

from this test are presented in Figure 55. The constitutive model can simulate the superelastic behavior in multi-direction loading directions. Plastic deformation in uniaxial loading results in the residual strain, which came from residual martensites. The materials properties used are representative of typical SE NiTi, but not for specific samples, which were summarized in Table 8.

3.3.3 Finite Element Program Implementation

The finite element implementation is accomplished using the User Material Interface provided by ABAQUS. The strain increment is passed to the user material subroutine and the corresponding stress increment calculated from the constitutive relations using the return mapping algorithm. The state variables, including austenite volume fraction and effective plastic strain, are also updated. The strain increment can be expressed as:

$$d\varepsilon_{ij} = -\delta d\alpha(\frac{\sqrt{3}}{2\sqrt{J_2}}S_{ij}) + E^{-1}_{ijkl}d\sigma_{kl}.$$

Multiplying both sides by elastic modulus gives the trial stress increment as:

$$d\sigma^{t}_{ij} = E_{ijkl}d\varepsilon_{kl} = -\delta d\alpha(\frac{\sqrt{3}}{2\sqrt{J_2}}E_{ijkl}S_{kl}) + d\sigma_{ij}, \qquad (8)$$

The austenite volume fraction increment is expressed as:

$$d\alpha = \frac{\partial\alpha}{\partial\sigma_{eff}}\frac{d\sigma_{eff}}{d\sigma_{ij}}d\sigma_{ij}, \qquad (9)$$

where σ_{eff} is the von Mises stress (effective stress). $\partial\alpha / \partial\sigma_{eff}$ is determined by the one dimensional Ivshin-Pence model. The rate form of austenite volume fraction in Ivshin-Pence model is expressed as:

$$\frac{d\alpha}{dt} = \left\{ \frac{\alpha(t_K)}{\alpha_{\max}(\beta(T(t_K), \sigma_{eff}(t_K)))} \right\} \frac{d\alpha_{\max}}{d\beta} \left(\frac{\partial\beta}{\partial T}\frac{\partial T}{\partial t} + \frac{\partial\beta}{\partial\sigma}\frac{d\sigma_{eff}}{dt} \right), \frac{d\alpha}{dt} \le 0$$

$$\frac{d\alpha}{dt} = \left\{ \frac{1-\alpha(t_K)}{1-\alpha_{\min}(\beta(T(t_K), \sigma_{eff}(t_K)))} \right\} \frac{d\alpha_{\min}}{d\beta} \left(\frac{\partial\beta}{\partial T}\frac{\partial T}{\partial t} + \frac{\partial\beta}{\partial\sigma}\frac{d\sigma_{eff}}{dt} \right), \frac{d\alpha}{dt} \ge 0$$

In the modeling of superelasticity at a constant temperature, the above equation becomes:

$$\frac{\partial\alpha}{\partial\sigma_{eff}} = \left\{ \frac{\alpha(t_K)}{\alpha_{\max}(\beta(T(t_K), \sigma_{eff}(t_K)))} \right\} \frac{d\alpha_{\max}}{d\beta}\frac{\partial\beta}{\partial\sigma_{eff}}, \frac{d\alpha}{dt} \le 0$$

$$\frac{\partial\alpha}{\partial\sigma_{eff}} = \left\{ \frac{1-\alpha(t_K)}{1-\alpha_{\min}(\beta(T(t_K), \sigma(t_K)))} \right\} \frac{d\alpha_{\min}}{d\beta}\frac{\partial\beta}{\partial\sigma_{eff}}, \frac{d\alpha}{dt} \ge 0$$

For isothermal phase transformation, the switching constant t_k are the times of stress reversal. In the 3D generalization considered here the switching constants become times of von Mises stress reversal (equivalent to $\dot{J}_2$ reversal). Insert equation (9) into (8), the elastic trial stress is expressed as:

$$d\sigma_{ij}^t = \left(I_{ijkl} - \delta \frac{\partial\alpha}{\partial\sigma_{eff}} \frac{d\sigma_{eff}}{d\sigma_{im}} \frac{\sqrt{3}}{2\sqrt{J_2}} E_{mjkn} S_{nl} \right) d\sigma_{kl} = C_{ijkl} d\sigma_{kl}$$

After C_{ijkl} is calculated, the real stress increment $d\sigma_{ij}$ can be obtained by correction of the elastic trial stress increment $d\sigma_{ij}^t$

The indentation model was comprised of 15000 axisymmetric 4-node bilinear elements. Part of the mesh around contact region is shown in Figure 56. The indenter

was modeled as rigid body sphere using the corresponding feature in ABAQUS to increase computation efficiency. The friction coefficient between the indenter and the substrate is assumed to be zero. A reference elastic-plastic material was simulated under the same indentation conditions for comparison. Its elastic modulus and Poisson's ratio were the same as that of SE NiTi; its von Mises plasticity duplicated the loading stage of SE NiTi. The reference material properties are summarized in Table 8.

3.3.4 Validation and Discussion

The absolute and normalized load-displacement curves of indentations are shown in Figure 57 for three different indentation depths. The recovery ratio η is defined as a measure of the indent depth recovery:

$$\eta = \frac{h_{\max} - h_{residual}}{h_{\max}},$$

where h_{max} is the maximum indentation depth and $h_{residual}$ the residual indent depth after unloading. The recovery ratio η is smaller at deeper indentation depths for both SE NiTi and reference material. Experimental results has shown complete spherical indents recovery ($\eta = 100\%$) on SE NiTi [*117*], which were reproduce computationally here at shallow indentation depth, by the modeled indentation-induced superelasticity. The reference elastic-plastic materials' recovery ratios are much smaller than that of the SE NiTi at each indentation depths.

Tabor introduced the representative strain for spherical indentations:

$$\varepsilon_r = 0.2\frac{a}{R},$$

where a is the contact radius and R the indenter radius [*112*], which is also reviewed in 2.5.2. Ni *et al.* found that the spherical indentation-induced SME has 100% recovery when $\varepsilon_r \leq 5\%$ [*116*]. This is comparable to results of uniaxial loading of SE NiTi: when uniaxial strain was smaller than 5%-7%, the recovery of deformation strain upon unloading can be complete. The recovery ratio vs. representative strain from FEA modeling is shown in Figure 58. However, the complete recovery of $\eta = 100\%$ is obtained only at the lower representative strain of 1.5%. The cause of this discrepancy may be due to the constitutive modeling. Another likely cause is the stress-strain concentration at the contact edge, discussed below.

Figure 59 compares two computational load-displacement curves with experimental results from Ni *et al* [*117*]. The load-displacement curves are from two modeled NiTi materials with same properties but different phase transformation hysteresis Δ, where Δ = $(A_f+A_S)/2-(M_S+M_f)/2$. The modeled SE NiTi with Δ=30K is used only in Figure 59, to show the effect of phase transformation hysteresis on load-displacement curves. It is obvious that larger Δ also increases the hysteresis of indentation load-displacement curves. The two computational curves match the experimental results quite closely. The Δ=15K curve is more close to the experimental results in the loading stage while Δ=30K curve is more close in the unloading stage. In contrast, the experimental SE

NiTi's Δ is more than 70 K [*117*]. Better material calibration is needed to obtain a closer match between experiments and the finite element model.

The distribution and size of the indentation-induced phase transformation region is difficult to determine from experimental measurements, but is easily available from finite element modeling. Figure 60 depicts the indentation-induced phase transformation regions at peak load and at the end of unloading. The indentation depth is shallow so that the recovery ratio is 100 %. The contours of the transformed area consist of concentric hemi-spherical rings with maximum value at 0.6 a (contact radius) and size of 1.8 a. This corresponds to the contours of von Mises stress by the one dimensional constitutive relation. The shallow indentation does not exhaust the stress induced martensite phase transformation, where maximum austenite volume fraction is less than 60 %. Reverse transformation upon unloading lead to a perfect indent recovery and there are very few residual martensites (Figure 58 (b)). In comparison, the reference material has a recovery ratio of 56 %.

Figure 61 (a) shows that a deeper indentation resulted in a larger transformed area of 2.2a. The maximum transformed area is still located at 0.6a but inclined towards the contact edge, because there is stress-strain concentration at contact edge at deeper indentation depth. Although this concentration is not predicted by contact mechanics, the situation is also present in the modeling using reference materials and in results from other researchers [*115*]. The plastic strain contour in Figure 61(b) shows the largest plastic strain initiated at the contact edge. The plastic deformation impedes the reverse

phase transformation during the unloading stage and the indent recovery is not complete ($\eta = 71\%$). Contours of residual martensite expressed as austenite volume fraction is shown in Figure 61(c), which has an intriguing irregular pattern.[‡] More residual martensite segregates around the contact edge and near surface area and fade into austenite phase around $1.5a$. The size of the indentation-induced transformed region is also plotted in Figure 58. The transformed region is approximately two times the contact radius, which increases slightly with indentation depth.

In summary, spherical indentation on SE NiTi is investigated using finite element method, which incorporates a three dimensional constitutive model of the shape memory effect with plasticity:

1) The computational load-displacements curves from spherical indentation modeling capture indentation-induced superelasticity, which has exceptionally large indent recovery ratios compared to elastic-plastic materials.
2) Martensite phase transformation is driven by contact stresses, whose hemispherical contours have an outer limit of approximately two times the contact radius for indents with perfect recovery, and increase in size at deeper indentation depths.
3) For shallow indentation depths, the stress-induced martensite phase transformation is the deformation mechanism and no plasticity is involved. The indents recover perfectly after unloading, leaving very few residual martensites. For deep

[‡] The contours did not change with different mesh densities. Thus the pattern is not likely to come from numerical errors in the FEA.

indentations, plasticity develops first around contact edges. Plasticity impedes the reverse austenite to martensite phase transformation and results in partial indent recovery, where much more residual martensites are left after unloading.

4) The computational load-displacement curves match experimental results closely. There is disparity between the phase transformation hysteresis of computational and experimental SE NiTi. The perfect indent recovery predicted by the finite element model occurs at the lower representative strains than experimental values. Closer agreement between experiments and finite element models would need more accurate input parameters from better material calibration.

Chapter 4

Results and Discussion

4.1 Tribological System with NiTi Interlayers

The tribological performance of hard-coatings, such as chromium nitride and diamond like carbon, depends intimately on mechanical properties of the support structure beneath coating, which was review in section 2.6. In this work, the hypothesis of using superelastic NiTi interlayers to moderate contact stress and strain, and shield the soft substrates from plastic deformation, was tested by experiments.

To investigate how the mechanical properties of NiTi interlayers affect the tribological performance of the whole coating system, it is best that the tribological performances can be compared with martensite and austenite (superelastic) NiTi interlayers, *within one sample*. The temperature scanning methods complemented previous wear test results at room temperature by showing that in one single sample the tribological performance could change dramatically with the phase transformations of NiTi interlayers.

The various CrN:NiTi:Al specimen forms prepared in this study are designated by the following notation:

$$^{A}\mathrm{CrN}:^{B}\mathrm{NiTi}_{AF}:\mathrm{Al},$$

where the superscript *A* is coating thickness (μm) and *B* is interlayer thickness (μm).

The subscript "AF" is the austenite finish temperature A_f of NiTi interlayer. For instance, a sample with a 3.9 μm thick CrN coating and a 15 μm NiTi interlayer with A_f 353 K on an aluminum substrate would be

$$^{3.9}\text{CrN}:^{15}\text{NiTi}_{353}:\text{Al}.$$

A sample with a 2.5 μm thick DLC coating and a 21 μm NiTi interlayer with A_f 368 K on an aluminum substrate would be

$$^{2.5}\text{DLC}:^{21}\text{NiTi}_{368}:\text{Al}.$$

4.1.1 Residual and Phase Transformational Stress in NiTi Interlayers

The measurement of phase transformational stress is to prove that NiTi interlayers on the aluminum substrates, even covered with hard coatings, can change the mechanical behavior of the whole composite structure significantly, due to martensitic phase transformations. It has been shown in temperature scanning X-ray diffraction (Figure 50 to Figure 52) that the NiTi thin films on aluminum substrates undergo thermoelastic martensite phase transformation. Figure 62 to Figure 66 show that NiTi interlayers, attached to the aluminum substrates and further covered by the hard coatings, could have the stress-strain response similar to those from free-standing thin films.

Figure 62 shows the stress evolution in NiTi thin films on aluminum substrates continuously over three heating-cooling cycles, while Figure 63 shows the details of the first heating-cooling cycle. Figure 64 shows the slope of the residual stress change vs.

temperature due to CTE mismatch. Figure 65 shows the residual stress change due to phase transformation.

The residual stress in NiTi interlayers comes from two origins: the intrinsic stress from PVD process, and the extrinsic stress from coefficient of thermal expansion (CTE) mismatch, which was discussed in section 2.3.1. The aluminum substrates' CTE is larger than that of NiTi thin films. Thermal stress change is *tensile* during heating and *compressive* during cooling. The CTE mismatch between NiTi thin films and silicon substrates gives -1.0 MPa/K thermal stress rate (derivation can be found in section 2.3.1).

The residual stress can be relaxed partly or completely by martensite transformation, and restored by the reverse phase transformation. The transformational stress relaxation rate is governed by the thermodynamics of martensite phase transformation, which is described by the Clausius-Clapeyron equation in section 2.2.2. The transformational stress relaxation and restoration cause a significant but reversible wafer curvature change/displacement within a relatively small temperature hysteresis of about 80K.

The most significant problem encountered in the stress measurement is the plastic deformation of the 6061 T6 aluminum substrates occurs during deposition or heat treatment process where temperatures reached around 800K. This temperature is more than 2/3 of the melting point of aluminum (933K). The intrinsic compressive stress in NiTi thin films could plastically warp the aluminum substrate at this temperature to give a large plastic curvature. Were this curvature elastic, it would require 2-3GPa residual stress in the NiTi thin films, which is not possible for the NiTi thin films. It is difficult

to distinguish the plastic curvature and elastic curvature in the total curvature.

The residual stress shown from Figure 62 to Figure 65 is compressive (negative). The actual temperature could be lower than the measured temperatures because the thermocouple was inserted in a tight-fitting hole on the side of the furnace, not contacting the samples.

There are some fine details about the phase transformations revealed in the stress evolution. First there are nonlinear stress relaxations before the phase transformations in both heating and cooling directions. The stress relaxation flattens to the theoretical 1.01MPa/K curvature to a smaller or even negative values before actual phase transformation starts.

The R phase transformation might also be present in the second cycle (red curves) in the cooling direction (Figure 62). There was a stress relaxation about 20MPa before the martensitic phase transformation that can be caused by R-phase transformation. But the complicated precursor behaviors are not the focal point of the residual stress measurements here.

Relaxation of the residual stress is also obvious in Figure 62 between three consecutive heating-cooling curves, because the stress loops do not overlap each other. The stress relaxation might also come from the creep of the aluminum substrate. But generally the phase transformation behavior of NiTi thin films on aluminum substrate is quite strong and stable.

Figure 66 shows the curvature of $^{2.5}$DLC:^{12}NiTi$_{368}$:Al sample at different

temperatures, measured by optical profilometer scanning, from which the phase transformation stress in the NiTi interlayer can be measured. M_f and A_f temperatures were reached because further cooling and heating about 10 K did not change the curvature significantly.

To support tribological experimental data presented from 4.1.2 to 4.1.7, it is necessary to consider the residual stress in the composite structure of hard coating:interlayer:substrate. Because of the residual stress in DLC coating, the stress in the NiTi interlayer, and their coupling, plus the plastic curvature in aluminum substrate, it is very difficult to obtain full details of the real residual stress. One important piece of information that can be obtained in Figure 66 is the residual stress change due to the phase transformation of the NiTi interlayer, with the covering DLC coating. The phase transformation relaxed 450MPa compressive stress in the NiTi interlayer when cooling from austenitic phase to martensitic phase.

This is presented as proof that the NiTi interlayer has robust phase transformation that can affect the mechanical response of the tribological system.

4.1.2 Wear Resistance of CrN Coatings on 6061 Al Substrates with NiTi Interlayers

The wear resistance was measured in terms of wear loss at different temperatures for samples with and without NiTi interlayers. The definition of wear loss is introduced in

2.5.4. Figure 67 shows the temperature scanning wear test results on $^{3.9}$CrN:^{15}NiTi$_{353}$:Al and $^{3.9}$CrN:Al samples using the 200μm tip radius spherical indenter under 0.49N and 0.98N loads. $^{3.9}$CrN:^{15}NiTi$_{353}$:Al had two orders of magnitude improvement in wear resistance at temperatures above A_f, compared to $^{3.9}$CrN:Al. For $^{3.9}$CrN:^{15}NiTi$_{353}$:Al, the superelastic (austenitic) NiTi interlayer gave two orders of magnitude improvement in wear resistance as compared to the martensitic interlayer. The improvement in wear resistance decreased as the temperature was decreased towards room temperature. At room temperature with a martensitic interlayer, the wear resistance of $^{3.9}$CrN:^{15}NiTi$_{353}$:Al was slightly better (40% less for 0.49N load) than that $^{3.9}$CrN:Al. The wear resistance of samples without a NiTi interlayer changed very little over the temperature range.

The CrN:Al samples' wear results had no temperature dependence while CrN:NiTi:Al samples had a strong temperature dependence. Since the only difference between CrN:NiTi:Al and CrN:Al samples is the NiTi interlayer, the temperature dependence can only be explained by the temperature dependant mechanical properties of the NiTi interlayer. The improvement in wear resistance was thus apparently due to the superelasticity of the NiTi interlayer at temperatures above A_f. The superelasticity of the NiTi interlayer accommodated the contact strain, which was recovered after the wear counterpart was moved. Much less plastic deformation was left with each passing of the wear counterpart. The cyclic wear test amplified this effect. The wear loss of $^{3.9}$CrN:^{15}NiTi:Al (Figure 67) with SE interlayer is 40 times smaller than the same sample

with a martensite interlayer.

SEM images of the wear tracks where are shown in Figure 68 (0.98N load) and Figure 69 (0.49N load). The wear tracks from 0.49N shown in Figure 69 were similar to that in Figure 68, only the extent of deformation was much less. The better wear resistance is obvious in the less deformed wear tracks that were made above A_f. 0.98N load gave especially deep wear tracks in $^{3.9}$CrN:Al in Figure 68, with part of the CrN coatings delaminated. The wear track in $^{3.9}$CrN:Al also showed large spherical craters lying across the wear tracks.

It is natural that improvement in wear behavior with superelastic interlayers under 0.49N load is more significant than that under 0.98N. Under 0.49N load, the improvement in wear loss with SE NiTi interlayers compared to $^{3.9}$CrN:Al samples was higher than the case under 0.98N load. This is because lower load produced less deformation, and the percentage of the deformation that could be recovered by the superelastic response of the NiTi interlayer was larger, which means the superelasticity of NiTi interlayer was more prominent.

During the wear test, the motion of spherical indenter pushed the soft substrate material forward and piled the material ahead of the indenter by plastic deformation. But with the increasing piling-up, resistance to the motion of the indenter also increased, which eventually forced the indenter to "jump" across the piled material to a flat area. However wear tests on samples with superelastic NiTi interlayers did not show this behavior because the superelastic interlayer significantly reduced the plastic deformation

of the aluminum substrate.

Wear tracks with SE NiTi interlayers in Figure 68 had a smooth and shallow geometry, showing strong evidence of superior wear resistance. Wear tracks produced at lower temperature with martensitic NiTi interlayer had a resemblance to the wear tracks in CrN:Al, also showing slight delamination of CrN and substrate deformation. It is quite remarkable that the wear resistance changed so dramatically in the same sample when temperature was changed less than 100K.

The temperature scanning wear tests were repeated with a NiTiCu interlayer. The ternary NiTiCu interlayer has a narrower hysteresis than NiTi interlayer, which can be seen in the X-ray diffraction data (Figure 51). Tribological behavior can be potentially by influenced by the hysteresis of superelastic interlayers.

Figure 70 shows the SEM images of the wear tracks at different temperatures. The wear track produced with the presence of superelastic NiTiCu interlayer was narrower and shallower than wear track produced with a martensitic interlayer. Figure 71 shows the wear data on $^{1.7}$CrN:^{9}NiTiCu$_{343}$:Al samples. At room temperature, martensitic NiTiCu interlayer gave around 2 times improvement in wear resistance compared to the sample without interlayer, while $^{3.9}$CrN:^{15}NiTi:Al had only about 2 times improvement to compared to $^{3.9}$CrN:Al at room temperature. This may be because the $^{1.7}$CrN:^{9}NiTiCu$_{343}$:Al had larger ratio of interlayer to hard coating thickness (5.3) than $^{3.9}$CrN:^{15}NiTi$_{353}$:Al (3.8).

At temperature above A_f, the wear resistance of $^{1.7}$CrN:^{9}NiTiCu$_{343}$:Al is about 10

times higher than that the sample without interlayer. But the improvement in wear resistance with a superelastic interlayer was only 5 times compared to a martensitic interlayer. This number was smaller than the 80 times improvement in $^{3.9}$CrN:^{15}NiTi$_{353}$:Al samples when the NiTi interlayer transformed from martensite to austenite. This can only be explained by the difference in the mechanical properties between NiTi and NiTiCu interlayers. The superelasticity of the NiTiCu interlayer may be worse than that of the NiTi interlayer, which means the NiTiCu interlayer had smaller recoverable strain. The smaller recoverable strain limited the improvement in wear resistance. It would be best if there are tensile test results of both NiTiCu and NiTi thin films so that the differences in mechanical properties could be compared.

The SE NiTi interlayer thickness affects the wear resistance of CrN coating significantly. Figure 72 shows at room temperature how CrN and NiTi interlayer thickness affect wear resistance. The wear test was done using 6.35mm diameter WC under 5N load. For aluminum substrates, thicker CrN and NiTi interlayers improved the wear resistance. It is quite easy to understand that thicker CrN coating has better wear resistance, because thicker CrN coating bears more contact stress due to its high hardness, providing the increased residual stress associated with the thicker coating does not compromise interfacial adhesion.

CrN coating's intrinsic compressive stress scales with thickness [*223-225*]. Thick CrN coatings on steel substrates usually suffer performance degradation for the large intrinsic stress weakens the interface between CrN coating and substrate. This situation

is proved in the tribological tests of CrN:NiTi:M2, which is discussed in the next paragraph.

The martensitic NiTi interlayer also increases the wear resistance, compared to samples without interlayers. There is 40 times improvement between $^{1.7}$CrN:^{15}NiTi$_{353}$:Al and $^{1.7}$CrN:Al at room temperature. Where did this improvement come from? In scratch test results discussed in 4.1.6, it is obvious that the interfacial adhesion between CrN and NiTi at room temperature is worse than adhesion between CrN and Al. The improvement in wear resistance can not come from the adhesion of CrN coatings. It is more likely that the improvement in wear resistance comes from the better mechanical properties of martensitic NiTi interlayers compared to the soft aluminum substrates. The fatigue resistance of martensitic NiTi interlayer may be superior to those of the aluminum substrates. The martensitic NiTi interlayer may be able to accommodate large strain by aligning martensite variants and twins without introducing significant defects. The yield stress of NiTi interlayer (~200 MPa) [51, 52] is close to that of the fully annealed aluminum substrate (HRE 62, ~180MPa).

4.1.3 Contact Stress Induced Phase Transformation in NiTi Interlayer

The experimental results discussed in the previous sections clearly show that contact stress induced phase transformation in NiTi interlayer has a strong influence on tribological performance. Here two topics will be discussed about the contact stress

induced phase transformation in NiTi interlayer that will provide some interesting information. The first is about contact loading conditions that trigger the phase transformation. The second is about finite element modeling of spherical indentation on CrN:NiTi:Al.

Similar to uniaxial loading of SE NiTi, whether there is superelastic effect in NiTi interlayer is also dependant on the contact load conditions. If the contact stress is too small, the NiTi interlayer behaves like normal elastic material, and there is no difference in wear resistance between martensite and austenitic NiTi interlayer. Figure 73 shows the temperature scanning wear tests on $^{1.7}$CrN:^{15}NiTi$_{353}$:Al and $^{1.7}$CrN:Al samples using a 3.175mm radius WC ball under 0.98N. There is no improvement of wear resistance when the NiTi interlayer is superelastic at temperature above A_f. The reason is that under same 0.98N load, 3.175mm radius WC ball gave much less contact stress than the 200μm radius diamond indenter used in section 4.1.2. The contact stress was not large enough to initiate the superelastic effect in NiTi interlayer. In other words, the contact strain can be accommodated by the elastic deformation of CrN coating and NiTi interlayer and superelasticity is irrelevant.

In Figure 73, the martensitic NiTi interlayer improves the wear resistance of the CrN coating by nearly 100 times. This improvement is higher than the 40 times improvement in $^{1.7}$CrN:^{15}NiTi$_{353}$:Al and $^{1.7}$CrN: Al discussed in section 4.1.2 with Figure 72 because the load used here was decreased to 0.98N instead of 5N, but the wear counterpart remained a 6.35mm WC ball. It has been discussed that thicker martensitic

NiTi interlayers resulted in better wear resistance. So under lower wear load, the thicknesses of NiTi interlayers were virtually increased because the contact stress contours are geometrically similar (lower load gave smaller stress contours).

Figure 74 plots the elastic contact stress in elastic half space under 3.175mm radius sphere and 200μm radius sphere as a function of load using the equation introduced in 2.5.1:

$$p_0 = \frac{3P}{2\pi a^2} = \left(\frac{6PE^{*2}}{\pi^3 R^2} \right)^{1/3}$$

$$\frac{1}{E^*} = \frac{1}{E_{indenter}} + \frac{1}{E_{substrate}},$$

where P is normal load, a is contact radius, R is the indenter radius, E^* is composite modulus. The 3.175mm radius sphere under 0.49N has 558MPa elastic contact stress. This number is further attenuated by the CrN coating, and its intrinsic compressive residual stress, which in the end is not strong enough to trigger the superelastic response of NiTi interlayer. The elastic deformation of the CrN:NiTi:Al composite structure would be enough to support the contact stress around 550 MPa.

But on the other hand, the 200μm radius sphere gave a very high elastic contact stress (>2000MPa), which was impossible to support elastically. It has to be mediated by the deformation in the coating:interlayer:substrate system. The superelastic NiTi interlayer can accommodate the deformation superelastically while a martensitic NiTi layer and the aluminum substrate cannot, which is why the wear resistance improvement is present only under higher contact stress/strain loading conditions.

4.1.4 Wear Resistance of DLC Coatings on Soft Substrates with NiTi Interlayers

Temperature scanning wear tests were performed on the DLC:NiTi:Al and DLC:Al samples. The DLC (diamond-like-carbon) coating has different mechanical properties and residual stress compared to the CrN coatings. How these differences change the tribological behaviors with the presence of NiTi interlayers would provide valuable information on this complex problem, along with more convincing evidence that SE NiTi interlayer could enhance tribological performance.

First the DLC:NiTi:Al samples also showed improvement in wear resistance with the superelastic NiTi interlayers at elevated temperature. Figure 75 presents the wear resistance of $^{2.5}$DLC:^{9}NiTi$_{368}$:Al, $^{2.5}$DLC:^{15}NiTi$_{368}$:Al, $^{2.5}$DLC:^{21}NiTi$_{368}$:Al and $^{2.5}$DLC:Al samples at different temperatures. The NiTi interlayers have 9μm, 15μm, 21μm thicknesses. The SEM images of the wear tracks are compared in Figure 76. The 21μm SE NiTi interlayer improved the wear resistance 340 times compared to $^{2.5}$DLC:Al samples at temperature above A_f. The 15μm SE NiTi interlayer improved the wear resistance about 60 times compared to $^{2.5}$DLC:Al. This improvement is similar to the $^{3.9}$CrN:^{15}NiTi$_{353}$:Al with 15 μm SE NiTi interlayer, which had a 80 times improvement compared to $^{3.9}$CrN:Al. $^{2.5}$DLC:^{9}NiTi$_{368}$:Al sample only improved wear resistance about 4 times compared to $^{2.5}$DLC:Al sample.

The thicker NiTi interlayers greatly increased wear resistance. The $^{2.5}$DLC:^{9}NiTi$_{368}$:Al sample with a thin 9μm SE NiTi interlayer did not improve the wear resistance significantly, while 21μm SE NiTi interlayer produced a much better

improvement. Thicker NiTi interlayer (21 μm) even improved the wear resistance of DLC coating at room temperature in martensite phase quite significantly (10 times), compared to the DLC:Al sample. The improvement in wear resistance as a function of interlayer thickness is not linear, but logarithmic.

The reason of why thicker interlayers are better lies in the fact that contact stress and strain decays with depth. The basics of contact mechanics are reviewed in section 2.5.1 and 2.5.2. The contact stress and strain fields are hemispherical contours, the intensities of which decay with depth. For a given coating thickness, a thicker interlayer means larger portion of the contact strain is supported by the coating and interlayer, while the substrate is subjected to smaller stress and strain. Smaller contact stress and strain in aluminum substrates gave smaller plastic deformation.

It is true that thicker NiTi interlayer costs more in deposition time and target material but the increase in cost is linear, which justifies the benefits of thicker NiTi interlayer.

The DLC coating is known to have higher compressive stress than CrN coating but lower modulus and hardness. But the low friction coefficient of DLC coating makes it favorable in many applications. However no significant change in friction coefficient was observed with superelastic NiTi interlayer and martensitic NiTi interlayer in this work.

4.1.5 Wear Resistance of CrN Coatings on Hard Substrates with NiTi Interlayers

The wear results from CrN:NiTi:M2 system are quite different from that from CrN:NiTi:Al system, which vividly illustrates the importance of the mechanical properties of supporting substrates.

Figure 77 shows that the addition of a NiTi interlayer affects adversely on the wear resistance of CrN hard coatings. The increase in wear loss was biggest for 1.7 μm thin CrN coating and thick 12 μm NiTi interlayer, showing that large interlayer/coating thickness ratio is not suitable for hard substrates. On the other hand, small interlayer/coating thickness ratio for 6 μm NiTi interlayer and 3.9 μm CrN coating only caused moderate increase in wear loss compared to 3.9 μm CrN coating without an interlayer. The best result is seen in a thick coating/interlayer combination: 3.9 μm CrN coating and 12 μm NiTi interlayer, which is slightly better than the case without the NiTi interlayer.

Figure 78 presents the same data in Figure 77 but as a function of NiTi interlayer thickness. Although a thicker NiTi interlayer improves the wear resistance of samples with 2.8 μm and 3.9 μm CrN coatings, the wear resistance is still not improved compared with cases without the NiTi interlayers. For samples without interlayers, the wear resistance was highest for samples with the intermediate 2.8μm CrN coating.

The wear results on CrN:NiTi:M2 systems indicate that the NiTi interlayer may not be suitable for improving the wear resistance of hard coating/hard substrate combinations. The modulus and yield stress of NiTi interlayers are substantially lower than the CrN and

M2 tool steel. As a result, *strong interfacial adhesion must be realized* for a relatively weak interlayer between hard coating and hard substrate to function as an adhesive layer. However, scratch test results in section 4.1.6 shows the evidence of a weak interface between CrN and martensitic NiTi. Although the substrate is aluminum in that case, the CrN and NiTi interface is still the same here on steel substrates. The weak interface may very well be the reason for the worse wear resistance of CrN:NiTi:M2 compared to CrN:M2.

The interfacial adhesion problem can be solved, as shown in the DLC:NiTi:Al system discussed in section 4.1.7. It may yet be possible to improve the wear resistance of CrN:NiTi:M2 by promoting the interfacial adhesion between CrN and NiTi in a future study.

4.1.6 Interfacial Adhesion between CrN and NiTi

Figure 79 shows temperature scanning scratch tracks on a $^{3.9}$CrN:^{9}NiTi$_{353}$:Al sample. There is a significant temperature dependence of the scratch resistance. At temperature above A_f there was minimum coating delamination and failure but there is very significant coating delamination and failure at temperature around M_S in $^{3.9}$CrN:^{9}NiTi$_{353}$:Al. Figure 80 shows the scratch tracks of $^{3.9}$CrN:Al samples that were made at the same temperature. There is no change in scratch resistance with changing temperature. This comparison proves that the temperature dependence of the scratch

resistance of $^{3.9}$CrN:^{9}NiTi$_{353}$:Al sample only comes from the NiTi interlayer, which has temperature-dependant mechanical properties. It is direct evidence that the stress-induced superelasticity of NiTi interlayer can improve scratch resistance and lead to better tribological performance.

The scratch resistance can be quantified by a "critical load", which is the normal scratch load where interfacial failure occurs. The critical load is determined after scrutiny of various experimental data: the appearance of scratch tracks, changes in friction coefficient, and acoustic emission signals. In scratch tests on $^{3.9}$CrN:^{9}NiTi$_{353}$:Al samples, the acoustic emission signals, shown in Figure 81 and Figure 82, are good indication of the critical coating failure because of the sudden jump in acoustic emission when dramatic coating delamination happened. The critical coating failure load determined from acoustic emission can also be verified by inspecting SEM images of the scratch tracks (Figure 83 and Figure 84). The critical load determined from acoustic emission and SEM images agreed each other well. It is shown in Figure 85 that $^{3.9}$CrN:^{9}NiTi$_{353}$:Al has improved scratch resistance above A_f. The critical load jumped from 1.8N at room temperatures around M_s to 4.2N at temperatures above A_f. For $^{3.9}$CrN:Al, the scratch resistance remains relatively stable across the temperature range.

However it is noticeable in Figure 79 that $^{3.9}$CrN:^{9}NiTi$_{353}$:Al sample suffered more severe coating delamination than $^{3.9}$CrN:Al sample at temperature below A_f. The EDS obtained from delaminated region showed that the failure occurred at the CrN:NiTi interface (Figure 83) and CrN:Al interface (Figure 84), which suggested that the

CrN:NiTi interface was weaker than CrN:Al interface. Considering CrN and NiTi deposition took place at two different vacuum systems, the exposure of NiTi surface to air before deposition of CrN may contribute to the poorer interfacial adhesion. However the problem of insufficient adhesion is improved in subsequent DLC:NiTi:Al experiments.

4.1.7 Interfacial Adhesion between DLC:NiTi

The interfacial adhesion between DLC and NiTi was improved by two methods: interface chemistry and a sputter cleaning process. After deposition of NiTi and heat treatment, a 1μm pure Cr layer was deposited onto the NiTi surface without breaking vacuum. The NiTi:Al samples were then transferred to the TEER deposition system for DLC deposition. Aggressive sputter cleaning (3600 ks) was employed to remove about 0.5μm of the Cr. Another thin Cr layer (0.1μm) was then deposited onto the sputtered Cr surface before DLC deposition. The potentially weak interface between DLC and NiTi was replaced by cleaned and thin Cr surface. The reference samples without NiTi interlayer also went through this preparation procedures.

Scratch tests were used again to measure the interfacial adhesion of $^{2.5}$DLC:$^{15}NiTi_{368}$:Al and $^{2.5}$DLC:Al samples. The phase transformation temperatures of the NiTi interlayer were determined by temperature scanning X-ray diffraction (Figure 52). Figure 86 shows the scratch track on the DLC:Al sample produced by 107μm tip

radius spherical indenter and 7N linear progressive load, at room temperature. Figure 87 shows the scratch tracks on $^{2.5}$DLC:^{15}NiTi$_{368}$:Al produced under the same conditions. There is very severe DLC delamination and failure in the $^{2.5}$DLC:Al sample (Figure 86), while no significant coating fracture occurs in $^{2.5}$DLC:^{15}NiTi$_{368}$:Al (Figure 87) except at the edges of the scratch track. It is evident the interfacial adhesion between DLC and NiTi is much better than that between DLC and Al, even at room temperature with a martensitic NiTi interlayer. The delamination and dramatic failure of DLC coatings on aluminum substrates without NiTi interlayer at 7N scratch load made it unnecessary to conduct the scratch test at higher load.

Figure 88 shows the scratch track on $^{2.5}$DLC:^{15}NiTi$_{368}$:Al produced by the very high 30N scratch load. This load is more than 4 times higher than the case in Figure 86 and Figure 87. Under the high scratch load, the DLC coating failure is inevitable, which is manifest as fine cracks inside the scratch track. However the strong interface adhesion kept the fractured DLC coating attached to the NiTi interlayer. Otherwise the fractured coating would have the fragmented appearance in Figure 86 and Figure 79. The delamination interface was determined by EDS spectrum shown in Figure 89.

How does interfacial adhesion affect the appearance of the scratch tracks? Consider the scratch of $^{3.9}$CrN:^{9}NiTi$_{353}$:Al in Figure 79. The destructive nature of scratch test inevitably leads to some damage to the coating, CrN or DLC. A strong interface keeps the coating adhered to the interlayer or substrate, so that the fractures, which accommodate the contact strains, are uniformly spaced over the scratch track. This is

the case in the scratch tracks at temperature above A_f in Figure 79, also in $^{2.5}$DLC:^{15}NiTi$_{368}$:Al (Figure 87 and Figure 88). If the interface is weak, the coating would be fractured and then delaminated, damaged by the moving scratch head, resulting in the highly damaged look in scratch tracks at temperatures around M_S as seen in $^{3.9}$CrN:^{9}NiTi$_{353}$:Al (Figure 79), and also in the $^{2.5}$DLC:Al sample (Figure 86). Whether there are dislodged coating fragments are good indication of whether there is good interfacial adhesion.

The temperature scanning scratch test in the $^{2.5}$DLC:^{15}NiTi$_{368}$:Al sample did not show significant temperature dependence, which is different than the temperature scanning test on $^{3.9}$CrN:^{9}NiTi$_{353}$:Al sample. The reason is that the interface between DLC and NiTi is intrinsically so strong that the influence of SE NiTi interlayer on the interfacial adhesion is greatly reduced. Due to the good adhesion, scratch at temperature around M_S did not cause delamination of DLC coating; the enhanced adhesion with SE NiTi interlayer at temperatures above A_f still gives similar scratch tracks because fracture in the DLC is something SE NiTi interlayer can not prevent. So under the improved adhesion between DLC and NiTi, there is no significant temperature dependence in the scratch tracks in $^{2.5}$DLC:^{15}NiTi$_{368}$:Al sample.

4.1.8 Finite Element Modeling of Indentation on CrN:NiTi:Al and CrN:Al

Single-cycle spherical indentation on $^{3.9}$CrN:^{15}NiTi:Al and $^{3.9}$CrN:Al samples is simulated in FEA. Although the indentation loading is simpler than the cyclic sliding loading in the actual ball-on-disk wear tests, spherical indentation captures the main features of the contact loading conditions. Figure 90 shows the load-displacement curve from the indentation simulation. The maximum indentation depth in $^{3.9}$CrN:^{15}NiTi:Al and $^{3.9}$CrN:Al was 2.1μm and 2.5μm, respectively, because the SE NiTi interlayer had higher yield stress than the fully annealed aluminum substrate. After unloading, the $^{3.9}$CrN:^{15}NiTi:Al had only 1μm residual depth while the $^{3.9}$CrN:Al had 1.9μm residual depth. The shallower residual depth in $^{3.9}$CrN:^{15}NiTi:Al probably results from a combination of strain-recovery in the SE NiTi interlayer and a decrease in the amount of plastic deformation occurring in the aluminum substrate. The result is generally consistent with the experimental result showing that the $^{3.9}$CrN:^{15}NiTi:Al provided better wear resistance.

Figure 91 and Figure 92 show the strain ε_{xx} and ε_{yy} calculated by FEA of $^{3.9}$CrN:^{15}NiTi:Al and $^{3.9}$CrN:Al, in the loaded and unloaded state. The contours for the loaded state of $^{3.9}$CrN:^{15}NiTi:Al showed that the highest strain was at the NiTi:Al interface, but without much strain mismatch across the interface; the strains in CrN:NiTi:Al were smaller compared to strains in $^{3.9}$CrN:Al. After unloading, the strain contours in CrN:Al were similar to that at the loaded state.

Figure 93 shows the shear strain (ε_{xy}) contours in $^{3.9}$CrN:^{15}NiTi:Al and $^{3.9}$CrN:Al. A high shear strain of about 6.5% appears at the position under the edge of contact, which indicates that the material was being pushed outside of the contact zone. The hard CrN coating was not affected by this shearing flow due to its high hardness. As a result, the high shear strain gradient was located beneath the hard coating interface. In $^{3.9}$CrN:Al, the majority of the shear strain was plastic deformation; in $^{3.9}$CrN:^{15}NiTi:Al, the NiTi interlayer accommodated most of the shearing strain superelastically. There were also a shear strain gradient across NiTi:Al interface, which was caused by different material properties across the interface. Overall, the shearing strains in aluminum substrate were less in $^{3.9}$CrN:^{15}NiTi:Al both in the loaded and unloaded state, as compared to $^{3.9}$CrN:Al.

Figure 94 depicts the martensite volume fraction from stress induced phase transformation in loaded and unloaded states. There was a highly transformed area around the contact edge due to the stress concentration there. The lower center near the interface between NiTi and Al also showed more stress-induced martensite, which accommodated the strains from the vertical displacement of the spherical indenter.

Figure 95, Figure 96 and Figure 97 show the stress components in $^{3.9}$CrN:^{15}NiTi:Al and $^{3.9}$CrN:Al. The highest stress always was located within the CrN coating, although in the terms of strain, the CrN coating always had the smallest amount of deformation. This shows that the hard coating on softer substrate can shield the substrate from high contact stress, but not from deformation. On the other hand, the differences in stress components in $^{3.9}$CrN:^{15}NiTi:Al and $^{3.9}$CrN:Al are not as significant as that in strains.

This means that the addition of NiTi interlayer can shield the softer substrate from large plastic deformation. With the hard coating supporting contact stress and the SE NiTi accommodating contact strain, the finite element analysis proves that the CrN:NiTi is a useful combination for the protection of softer substrates.

4.2 Indentation-induced Two-way Shape Memory Effect

The Two-Way Shape Memory Effect (TWSME) has been achieved in NiTi and other shape memory alloys under uniaxial and bending loading, which has been reviewed in section 2.4. In this work TWSME under contact loading conditions is demonstrated for the first time by two different training methods.

Textured surfaces can have different tribological properties, for instance, lower friction coefficient, compared to smooth surfaces [*226-230*]. Surfaces with reversible texture that is controlled by temperature can then have variable friction coefficient and other controllable tribological and optical properties. Such surfaces can be realized using indentation-induced TWSME.

The experimental demonstrations of indentation-induced TWSME are presented in sections 4.2.1 and 4.2.2. Before the discussion of the mechanisms of indentation-induced TWSME in 4.2.5, two experiments are introduced and discussed in 4.2.3 and 4.2.4, which reveal some interesting aspects of this complicated problem.

4.2.1 Indentation-induced TWSME from Thermomechanical Training

Thermomechanical training of shape memory alloy is accomplished by cycling between temperatures above A_f and below M_f when a specimen is subjected to external stress or constraint, which has been reviewed in section 2.4.2. In this study a complex contact loading condition was used instead of simple axial loading conditions. However the experimental setup was simple. The details are described in section 3.2. Briefly, a 3.175mm diameter tungsten carbide sphere was pressed into a martensitic NiTi alloy sample to a certain depth and then the sample was cycled between temperatures below M_S and above A_f.

After the treatment, spherical indents exhibit two-way depth recovery with a shallow indent depth observed at high temperature and deep indent depth at low temperature. The reversible depth change is about 45% of the total indent depth and is stable over many cycles. Figure 98 (a) shows the 3D indent profiles taken at temperatures above A_f and below M_S, respectively. Figure 98 (b) shows the cross section profiles of the heated and cooled indent. D_A was the depth after heating the sample to 400±5K. Since this temperature was near A_f, the NiTi was in the austenite phase. D_M was the depth after cooling the sample to ambient temperature of 300±3K. Since the ambient temperature was close to M_f, the sample was in the martensitic structure.

After the first heating step, the indent depth decreased from the original indent depth of about 170 μm to 80 μm (Figure 99), an approximately 53% indent depth recovery. This is reminiscent of the one-way indentation depth recovery reported by Ni et al., who

showed that the shape memory effect exists under complex loading conditions produced by spherical and sharp indentations [*116, 231*]. After cooling to the ambient temperature of 300K, the indent depth increased from D_A of about 80 μm to D_M of about 140 μm, an approximately 75% increase in the depth of indent. The subsequent heating-cooling cycles produced nearly constant indent depth ratio, $(D_M-D_A)/D_M$, of about 45% (Figure 100).

Figure 99 and Figure 100 show that the two-way indent depth change was quite stable over the five heating-cooling cycles tested. Both D_A and D_M slightly increased over the thermal cycles, with a small decrease in the two-way depth change D_A-D_M over the five thermal cycles. It is so far unclear the fatigue behavior of the two-way depth change (D_A-D_M) over more thermal cycles. The depth changed most significantly between the first and second thermal cycles. D_A increased 2.5μm; D_M increased 6.3μm and D_A-D_M increased 3.7μm. But their values stabilized over the next 4 cycles with D_A increasing 0.75μm/cycle, D_M 1.4 μm/cycle and D_A-D_M 0.65μm/cycle.

Figure 101 shows the ratio of $(D_M-D_A)/D_M$, which compares the depth change to the depth of the indent at martensite phase. The smallest ratio of depth change, around 0.5, is at the center of the indent. Although the ratio increases to 1 further away from the indent, both D_M and D_A become small and dominant by the surface roughness, causing the fluctuation in the ratio. Ideally the $(D_M-D_A)/D_M$ should approach zero for surfaces far away from indents, because the surface does not move between austenite phase and martensite phase. But (D_M-D_A) is not zero because: 1) small surface roughness change

in NiTi between martensitic and austenitic phase, 2) measurement error between two measurements.

The "ball-and-clamp" training used in this study was used to induce the low temperature shape into the sample by constraining the high temperature recovery. Under this "constant-strain" training procedure, the stress was not constant during the heating and cooling cycles. When heating temperatures above A_f, the stress under the sphere increased as the recovery was constrained. When cooling below M_f the stress was decreased. Since the displacement of the clamped ball was constant, the only effect that thermal cycling had created was the alternation between high and low contact stress. The resulting "sink-in" of the area around the indent indicated that additional dislocations were generated during the training, which most likely occurred during the heating stage when contact stress increased.

Undoubtedly plastic deformation was introduced in the martensite phase during the initial ball clamping or indentation process. The initial contact radius was about 0.8 mm. The representative strain ε_R :

$$\varepsilon_R = 0.2\frac{a}{R} = 0.2 \times \frac{0.8}{1.5875} = 0.10$$

The 10% representative strain was high enough to introduce slip-plasticity in the NiTi sample. These dislocations would have a spherically symmetric distribution due to the symmetry of the spherical indentation. When first heated above A_f, the intensified contact stress due to constrained recovery must have generated additional dislocations

into the austenite phase. The process should be equivalent to the process of an unconstrained recovery followed by indentation to the same depth in the austenite phase. These dislocations first introduced in the austenitic phase are different in mechanics compared to the previous set of dislocations from indentation in martensitic NiTi. It is also very possible that these dislocations would move when the sample was cooled back to martensitic phase, because internal stress and strain field changed. When the sample was heated back to austenitic phase, new dislocations might be introduced because the previous dislocations in the austenitic phase have moved due to phase transformations. The training cycles might stabilize these two sets of dislocations so that no more additional dislocations are introduced during heat-cooling cycles. However it is also possible that the stabilization is not achieved during training so that new dislocations are introduced during each training cycle, which might contribute to the "sinking-in" effect described below.

It is noticeable in Figure 98 that the area around the indent had a "sinking-in" effect in the martensite phase but was leveled in the austenite phase. The radius of the sinking-in area was about 1.8 mm, which was about 2.6 times of 700 μm indent radius. This sinking-in area and its reversible change over heating-cooling cycles indicate that the training procedure has affected not only the microstructure beneath the sphere but also a large portion of material around the indent. Since the surrounding area is not directly under the indenter, either propagation of dislocations or residual stress field causes the "sink-in" effect. Additional research is necessary to determine the

mechanisms of indentation-induced TWSME.

4.2.2 One-cycle Deformation Training and Reversible Surface Topography

The One-cycle deformation training method is an efficient and effective alternative training method to the thermomechanical training because it does not involve cyclic heating and cooling. Section 2.4.2 reviews previous research on the one-cycle deformation training method. The experimental procedures were described in section 3.2 of Chapter 3. First, spherical indents or scratches were made on the surface of a NiTi alloy in its martensite phase. Second, the indented or scratched surface was polished mechanically to restore a flat surface in a step referred to as "planarization". Two-way reversible circular and line *protrusions* were thus produced by altering the temperature to drive martensite-to-austenite phase transformations. Figure 102 schematically illustrates the preparation method and the proposed mechanisms responsible for the two-way reversible surface protrusions [*57*].

Spherical indentation was performed on a martensitic NiTi sample so that after being heated above A_f, the indent recovered partially. The experimental details are described in 3.2 of Chapter 3. Figure 103 showed that residual indent had two-way reversible depth change with heating and cooling: indents were shallower in the austenitic condition and deeper in the martensitic condition. The average reversible depth change was 13.6±0.3 μm over five thermal cycles tested, which is about 24% of the total indent depth. But the reversible depth change is not constant: it increased after first two thermal cycles.

This "self-training" effect is discussed in section 4.2.4.

Reversible surface topography can be realized from the indentation-induced TWSME. Figure 104 shows a 3×3 matrix of circular protrusions. Figure 105 shows the sectional profile of the reversible surface protrusion and its height over first five thermal cycles. Figure 106 shows the actual shape of the circular surface protrusion, with same length scale in the horizontal and vertical directions. Although in Figure 106 it seems the circular surface protrusion is not very significant because the aspect (height/ width) ratio is low, it is a strongly visible phenomenon.

Surface morphology can be characterized by several different kinds of surface fluctuations: form error, waviness, and roughness (Figure 107). Surface roughness is generally referred to the shortest-wavelength irregularities of a surface, and waviness is the intermediate-wavelength deviation, and form is the longest-wavelength deviation. Reversible surface protrusions can be potentially created to change the roughness, waviness or form error, depending on the loading conditions of the indentations. The surface protrusion shown in Figure 106 creates a surface form error, which is a long-wavelength deviation from a flat surface. Figure 108 shows that imposing surface protrusions close to each other and Figure 111 shows that nanoscale protrusions can be created. These indicate that close-packed micro- and nanoscale protrusions can be made on the NiTi surface to change surface waviness and roughness.

Figure 108 shows a reversible GM logo on the surface of a 2.54 cm diameter NiTi SMA sample. The images were taken from a optical microscope, but also visible to

naked eye. The letters were made by joining circular surface protrusions closely adjacent to each other. The indenter and indentation load are the same as those in making circular protrusions shown in Figure 104, except that the indents are close to each other with around 0.8 mm spacing.

Comparing Figure 106 with Figure 108, it seems the reversible surface protrusions are more significant optically than in physical dimensions. The reason is that the reversible surface protrusions are big change in terms of surface form. The polished flat surface of NiTi SMA had a roughness about 60 nm. The reversible surface protrusions have a height above 10 μm, which is very big compared to the surface roughness.

It is also shown in Figure 108 that making overlapping indents does not significantly diminish the reversible surface protrusions. Although the stress and strain field of each indent should be affected by the adjacent indents, it seems there is no detrimental effect. Currently it is unclear whether this would change fatigue behavior.

Figure 109 shows a line protrusion after an indented and planarized bulk NiTi sample was heated to the austenite phase. These protruding structures disappeared when the sample was cooled down to the martensite phase. The height of the circular and line protrusions was 13.6±0.1μm and 0.8±0.05μm over the first five heating-cooling cycles, respectively.

The geometry and size of reversible surface topography (RST) can be readily controlled by indenter shape and applied load. Furthermore, intricate patterns of RST

can be efficiently laid out by arranging positions of indentations or length and direction of scratches accordingly.

The reversible surface topography was also realized in sputter-deposited NiTi thin film on silicon substrates. This means the reversible surface topography could be readily integrated into the micro-electro-mechanical systems (MEMS). Figure 110 shows the same effect achieved in a 4.5μm thick sputtered NiTi thin film deposited on a (100)-silicon substrate. The height of the circular protrusion was 33.2±7.2 nm over the first five temperature cycles. However the protrusion deteriorated over the first five thermal cycles more significantly than RST on bulk NiTi samples (Figure 112), which is discussed in section 4.2.3.

Figure 111 shows the reversible line protrusions on NiTi thin films, which were planarized from a scratch that was produced by manually sliding a razor blade on the NiTi thin film. The line protrusions had three parallel lines. This may had come from some imperfections in the razor blade. There was also a non-reversible "x" shaped line protrusions nearby, which were from scratches in mechanical polishing.

Indeed, not every surface deformation in NiTi SMA could give reversible surface protrusions. Spherical indentation and sliding were shown to be effective loading conditions. But it is possible that more "blunt" indenters, like flat end punch, or more "sharp" indenters, like Berkovich indenter, could not successfully induced TWSME, which is for future research to clarify.

The RST in NiTi thin film on silicon substrate shown in Figure 110, deteriorated over

the first five thermal cycles (Figure 112). It is quite different from the RST in bulk NiTi. This can be explained by the effect of the NiTi thin film thickness. The indent diameter is about 7 μm. Therefore 7 μm NiTi thin film was needed to fully contain the deformation zone that supported the TWSME (see section 4.2.3 for detail). But the NiTi thin film thickness used in the experiment had a thickness of only 4.5μm, less than the contact diameter size that needs to support reversible surface protrusion. The compromised deformation region underneath indent caused the deterioration of reversible surface protrusion in Figure 112.

4.2.3 Layered Planarization

Insight into the mechanism underlying cyclic TWSME from indentation of NiTi-based shape memory alloys can be obtained by experiments in which successively deeper surface-removal steps are performed, until the reversible displacement effect is found to vanish. Results of such an experiment are shown in Figure 113. An indent was again made in martensitic NiTi, with a 1.59 mm diameter ball, and the specimen polished just sufficiently to remove any trace of the indent, while maintaining the temperature below M_f. After heating past A_f the height of the thermally-reversible surface protrusion was determined, and subsequently measured again as additional surface layers were successively polished away in each case, while the specimen was martensitic. The protrusion amplitude was found to monotonically decrease from initial

maximum of just over 11 μm until it vanished after ~0.5 mm (extrapolated) of the surface had been removed. Protrusion formation thus apparently involves transformational behavior in a subsurface zone nearly 40 times the protrusion height, indicating that the effect can be produced with an average of ~2.3% transformational strain in the subsurface volume, well within the known capability of TWSME in NiTi alloys [*4*].

Furthermore, when the contact mechanics of indentation are considered, the depth at which the cyclic protrusion amplitude vanished is consistent with existing theories on the mechanisms of TWSME in NiTi alloys. Figure 114 adapted from Samuels and Mulhearn [232] shows theoretical predictions and experimental results that give the distribution of plastic strain beneath a spherical indenter in Cu-30%Zn brass. Contours are shown for plastic strains of 7%, 1% and 0%, the latter contour corresponding to the elastic-plastic boundary. Of particular significance is the location of the 7% contour, occurring at a depth approximately equal to the radius of the contact perimeter of the indent. In the present experiment, the initial indent contact radius was 450 +/- 25 μm. Therefore, the surface removal experiment, in which the effect vanished after removal of ~0.47 mm (roughly equal to the initial indent contact radius), indicates that cyclic protrusion formation depends on TWSME occurring in material that experienced more than 6 to 7% plastic strain (in the martensite phase) during indentation. This corresponds closely to the maximum strain (6-8%) that can be tolerated by thermal martensite before the onset of plastic flow via dislocation production. It is therefore concluded that the initial indentation event created, within a near-surface zone whose

depth corresponded to the indenter radius, sufficient numbers of dislocations in the martensite that could later cause a shape strain to occur during the austenite-to-martensite transformation. At greater depth below the indent, where smaller plastic strains occurred, little dislocation production is expected since strains in this region can be accommodated entirely by martensite variant-boundary motion (deformation twinning). This deeper material effectively self-accommodated the transformational shears on cooling, and was therefore unable to contribute significantly to TWSME in the present context.

4.2.4 Small Hysteresis and "Self Training" of Reversible Surface Protrusion

The relaxation and recovery of surface protrusion has a much smaller temperature hysteresis compared to the phase transformation hysteresis of annealed NiTi alloy sample. Figure 115 showed the surface protrusion height vs. temperature, for planarization of a spherical indent that was produced under 60kg load using 1.587mm diameter ball. The protrusion started to rise before the nominal A_S temperature. Before the temperature reached $(A_S+A_f)/2$, surface protrusion height has already reached 90% of maximum height, with a rate 0.26μm/K. During the cooling stage, the surface protrusion decreased slowly before M_S but started a rapid descent well above M_S. Again 90% of the protrusion height was diminished before $(M_S+M_f)/2$ with a rate 0.31 μm/K.

As can be seen in Figure 115, the martensite-austenite phase transformation temperatures shifted to lower temperatures in the heating direction; the austenite-martensite transformation temperatures shifted to higher temperatures in the cooling direction. The hysteresis of the reversible surface protrusion was 30±3K compared to the phase transformation hysteresis of 60±5K, from DSC measurement of free standing sample (Figure 32).

How could, in TWSME, the martensite-austenite transformation temperatures shifted downwards to lower temperatures in the heating direction? Stalmans *et al.* noticed the lowering of phase transformation temperatures in TWSME when the sample was subjected to external stress that was "opposing" the direction of TWSME, and provided a plausible explanation from the Clausius-Clapeyron equation [106] (reviewed in detail in section 2.4.3) .

The main reason is that the directions of the transformation strain in TWSME are set by the training process; the external stress posed afterwards can either be "along" or "opposing" the direction of TWSME. The former elevates phase transformation temperatures and the later suppresses phase transformation temperatures. For instance, if a specimen was trained to possess such TWSME: shrinkage occurs during austenite-martensite transformation in the cooling direction ($\Delta\varepsilon_A^M < 0$) and elongation occurs during martensite-austenite transformation in the heating direction ($\Delta\varepsilon_M^A > 0$). The tensile stress is in the opposite direction of TWSME because it suppresses the strain change in the cooling direction.

The Clausius-Clapeyron equation can be used to explain this by simply considering the sign of enthalpy, strain and stress. The C-C equation is:

$$\frac{\Delta\sigma}{\Delta T}=\frac{\Delta H_A^M}{T\Delta\varepsilon_A^M}.$$

Tensile stress lowers the phase transformation temperatures as follows: on in cooling from austenite to martensite phase, $\Delta H_A^M>0, \Delta\varepsilon_A^M<0$ and $\frac{\Delta H_A^M}{T\Delta\varepsilon_A^M}<0$. The left hand side of the Clausius-Clapeyron equation $\frac{\Delta\sigma}{\Delta T}$ must has the same sign as the right hand side, $\frac{\Delta H_A^M}{T\Delta\varepsilon_A^M}$. Since $\Delta\sigma>0$ (tensile), ΔT must be negative to give $\frac{\Delta\sigma}{\Delta T}<0$ so that the left hand side of C-C equation was negative. Here the tensile stress lowers the phase transformation temperature in the cooling direction.

In the heating from martensitic to austenitic phase, $\frac{\Delta H_M^A}{T\Delta\varepsilon_M^A}$ is still negative because $\Delta H_M^A<0$, $\Delta\varepsilon_M^A>0$. Both enthalpy and strain change flip sign. Note that in one-way SME, the strain change does not change sign. Since $\Delta\sigma>0$ (tensile), ΔT is still negative.

Therefore, small hysteresis can be obtained in indentation-induced TWSME only if the residual stress meets the following requirements:

It must be in the opposite direction of TWSME during heating so that phase transformation temperatures are lowered;

It must not be in the opposite direction of TWSME during cooling so that phase transformation temperatures are elevated.

If the same TWSME specimen in the previous paragraph were subjected to compressive stress during cooling ($\Delta\varepsilon_A^M < 0$), the austenite-martensite phase transformation temperatures would be shifted upwards in the cooling direction; if the stress was changed to tensile during heating ($\Delta\varepsilon_M^A > 0$), the martensite-austenite transformation temperatures were shifted downwards in the heating direction. Thus small hysteresis can be achieved by moving the transformation temperatures towards each other.

In the above situation, the direction of the stress can actually assist the deformation: tensile stress with positive strain change and compressive with negative strain change. This could stabilize the TWSME.

A similar situation may be what actually happened in the small hysteresis behavior of reversible surface topography, which is shown in a schematic in Figure 116. It is known that residual stress exists in elastic-plastic indentation [108]. The distribution and extent of the residual stress in indentation-induced TWSME is very complicated, considering the coupling of martensite phase transformation and planarization process. However the residual stress may very possibly act in the direction that elevates the phase transformation temperatures during heating and suppresses the transformation temperatures during cooling, creating the small hysteresis.

Other experimental evidence comes from the "self training" effect of the indentation-induced TWSME. As can be seen in Figure 103 (reversible depth change from one-cycle deformation training) and Figure 105 (reversible circular surface

protrusions), initial thermal cycles after training process did not lead to immediate deterioration of the TWSME, but instead acted to strengthen the TWSME slightly. It was in sharp contrast to the fatigue behavior of uniaxial TWSME, where the two-way effect deteriorated significantly during the first several thermal cycles [101]. It has been pointed out in the previous paragraphs that for TWSME to have small hysteresis, the direction of external stress must be in directions to assist the deformation. The residual stress in indentation-induced TWSME may very possibly act this way, strengthening the TWSME, curbing the deterioration, and narrowing the temperature hysteresis.

4.2.5 Mechanism of Indentation-induced TWSME

The successive layered planarization experiment revealed that a zone underneath indent with the size of the indent diameter is mainly responsible for the reversible surface topography. Theoretical calculation based on contact mechanics and experimental measurements by Samuel and Mulhearn [232] also pointed out this zone is a highly deformed region with at least 7% plastic strain.

In one-cycle deformation training of TWSME, it is believed that the dislocation structure and the associated stress field create microstructural, thermodynamic and stress anisotropy within the martensite phase, as discussed in section 2.4.2. The *thermodynamic anisotropy* means that after training, the crystallographically equivalent martensite variants are no longer thermodynamically equivalent: the trained martensite

variants are thermodynamically preferred to the non-trained variants. The thermodynamic anisotropy must have come from certain changes in microstructure as the result of training. The microstructural basis of the thermodynamic anisotropy was termed *microstructural anisotropy*. As a result, martensite variants in certain orientations are thermodynamically favored over others when cooled from the austenite phase. The preferred nucleation and growth of these directional martensite variants enable the SMA to "remember" its low temperature shape.

As is shown section 2.4.2, slip-plasticity is effective to introduce TWSME under uniaxial loading. In indentation-induced TWSME, dislocations should play a similar important role to induce the reversible effect. Comparing to simple loading conditions such as tension and compression, indentation and scratching are effective to introduce dislocations locally and symmetrically. Several authors have suggested that indentations are accommodated by circular loops of "geometrically necessary dislocations" under spherical indenters [233, 234] (Figure 117). It is assumed that the indentation is accommodated by circular loops of geometrically necessary dislocations with Burgers vectors normal to the plane of the surface. As the indenter is forced into the surface of a single crystal, geometrically necessary dislocations are required to account for the permanent shape change at the surface. These geometrically necessary dislocations lead to spherically symmetric microstructures and residual stresses beneath the indents, which may induce TWSME.

On the other hand, the small hysteresis of the reversible surface topography and

"self-training" effect indicated the residual stress played a significant role in altering phase transformation temperatures and stabilizing the two-way effect. However, the distribution and extent of the residual stress in indentation-induced TWSME are very complicated, especially considering the coupling with the martensite phase transformation, which undoubtedly changes the residual stress significantly.

The residual stress and strain fields in an as-indented martensitic NiTi should be close to those in an elastic-plastic material. But how the stress and strain fields change after the first recovery is unclear. How those change in the following thermal cycles would be a useful finite element analysis to shed some light on indentational TWSME.

Indentational shape memory effect has not been modeled in this work due to the difficulty determining appropriate boundary conditions. Therefore a finite element analysis with general approximation was made here, which is an indentation in an austenitic NiTi. The reason is that the stress-strain field in austenitic NiTi, which includes the effects of stress-induced phase transformation, may be close to those after a thermally driven phase transformation in an austenitic NiTi.

Figure 118 presents a finite element analysis of the σ_{yy} residual stress field (normal to the surface) in austenitic NiTi after spherical indentation. There exits a highly compressive stress "core" extending from one quarter of the indent diameter to one indent diameter beneath the residual indent. The compressive stress also agrees with Figure 116, where there should be a compressive stress at temperature above A_f to pull the surface protrusion down. When cooling down from the austenite phase to the

martensite phase, this compressive stress in the vertical direction may be able to help pull material back from surface, which would create a deeper indent. How this residual stress evolves in phase transformations by heating and cooling would help provide more information.

Chapter 5

Conclusions and Future Work

5.1 Conclusions: Hard Coating Systems with NiTi Interlayer

Based on temperature-controlled scratch and dry sliding wear experiments on CrN and DLC coated 6061 T6 aluminum, tested both with and without NiTi interlayers, the following conclusions may be drawn:

1) Magnetron sputter deposition is capable of producing excellent adhesion of NiTi on aluminum substrates, without elaborate surface preparation or other adhesion-promoters.

2) The NiTi thin films on aluminum substrates display robust martensitic transformational behavior, as shown in temperature-scanning X-ray diffraction and wafer-curvature measurements. The wafer-curvature measured on DLC:NiTi:Al also shows strong phase transformational stress relaxation and recovery in the NiTi interlayer.

3) Superelastic NiTi interlayers on very soft aluminum substantially improves adhesion of nitride hard coatings, as indicated by an increase in the critical load for delamination as measured in temperature-controlled scratch tests. The marked increase in performance at test temperatures near A_f strongly suggests that stress-induced A->M transformation is responsible for the observed

improvement.

4) The adhesion of hard coatings to martensitic NiTi interlayers can be improved by deposition of a protective Cr layer and subsequent aggressive sputter cleaning. This procedure could also be replaced by depositing NiTi interlayers and hard coatings within the same vacuum chamber.

5) NiTi interlayers dramatically improve the wear behavior of CrN and DLC films on soft aluminum and can increase wear resistance by a factor of 100-300. The best performance is noted for test temperatures near or above A_f. Martensitic NiTi interlayers can improve the wear resistance by a factor of 40-100.

6) Thicker NiTi interlayers are more effective. Performance monotonically improves as the interlayer thickness is increases to 21 μm. Thicker CrN coating also increases wear resistance monotonically for thicknesses up to 4 μm. It is unclear now whether there is an upper limit to hard coating and interlayer thickness on aluminum substrates.

7) The NiTi interlayers between CrN and hard M2 steel substrates do not improve wear resistance significantly, compared to the samples without NiTi interlayers. It is suspected that the weak CrN:NiTi interface is responsible for the worse wear resistance of CrN:NiTi:M2. However the interfacial adhesion can be improved, which might lead to better wear performance of CrN:NiTi:M2 in future studies. Placing an interlayer that is softer and more compliant than the substrate can lead to larger strains in the hard coating, and larger interfacial

mismatches.

8) Finite element analysis proves that the use of superelastic NiTi interlayers can shield the soft aluminum substrate from contact strains, while the CrN hard coating can support contact stress. The combination of CrN hard coating and superelastic NiTi interlayer successfully protects the aluminum substrates.

5.2 Conclusions: Indentation-Induced TWSME

1) The two-way shape memory (TWSME) effect can be realized at the micro- and nano-scale using spherical indentation. Both thermomechanical cycling and slip-plastic deformation were proven to be effective training methods to induce the two-way shape memory effect. Thermomechanical cycling results in larger reversible indent depth change and a "sink-in" effect. The slip-plastic deformation is an efficient one-cycle training method and there is no "sink-in" effect. TWSME does not decay significantly over initial thermal cycles.

2) Reversible surface protrusions (RSP) are produced from planarizing spherical indents with TWSME. The height of the RSP is the same as the two-way indent depth change, which means the planarization process does not affect the TWSME. Layered planarization experiment shows that the RSP arises from transformational activity in a zone with the size of the contact radius beneath the indent, which is about the boundary of 7% plastic strain.

3) The residual stress underneath the indents may possibly strengthen the TWSME. The RSP has a smaller temperature hysteresis than that of the bulk NiTi SMA. Second is the "self-training" effect, which means the RSP does not decay but strengthens slightly during initial thermal cycles. From the above two phenomena and thermodynamic analysis, it is concluded that the residual stress from contact loading may be able to promote the TWSME and RSP.

5.3 Suggestions to Future Work

1) Mechanisms of indentation-induced shape memory, superelasticity and two-way shape memory effect. New experimental tools like synchrotron X-ray diffraction and in-situ TEM indentation can be used to analyze the microstructures beneath indents in NiTi alloys, along with traditional experimental techniques like cross-sectioning samples with indents.
2) Tribological applications of indentation-induced two-way shape memory effect. Surfaces with reversible surface protrusions could have different friction coefficients compared to flat surface. The difference in friction coefficients is also dependent on testing conditions like loading configurations and lubrications.
3) Development of finite element modeling of shape memory effect is the next step after current modeling of superelasticity. FEA of shape memory effect can provide stress-strain distributions beneath indents in NiTi before and after phase

transformations, which can be used to explain indentation-induced shape memory and two-way shape memory effect.

4) Tribological tests on CrN:NiTi:Al and DLC:NiTi:Al samples with re-heat treated aluminum substrates. The temper of 6061 T6 aluminum substrates were destroyed during NiTi interlayer deposition, which led to low hardness (HRE 62). It is possible to re-heat treat the aluminum alloy to restore the hardness to HRB 60, after the deposition of NiTi interlayers and hard coatings.

5) Finite element modeling using cohesive elements and user material subroutine for superelasticity. The cohesive elements can be used to model interfacial delamination between coatings, interlayers and substrates. It is possible to show in FEA that superelastic NiTi interlayers discourage interfacial delamination under contact loading, which supports experimental results. Parametric studies can also be carried out to find the optimal mechanical properties of hard coating, NiTi interlayer and substrate to maximize tribological performance.

Appendices

Table 1. Comparison of crystallographic data of NiTi martensite a, Otsuka et al [*20*]; b, Hehmann and Sandrock [235]; c, Michal and Sinclair [*21*]; d, Kudoh et al [*22*].

	OSS (a)	**HS (b)**	**MS (c)**	**KTSO (d)**
a (nm)	0.2889	0.2883	0.2885	0.2898
b (nm)	0.4120	0.4117	0.4120	0.4108
c (nm	0.4622	0.4623	0.4622	0.4646
β (°)	96.8	96.8	96.8	97.78
V (nm^3)	0.05463	0.05449	0.5455	0.05479
Atoms per unit cell	4	4	4	4
Space group	P2/c	$P2_1/m$	$P2_1/m$	$P2_1/m$

Table 2. Lattice structure and parameters of precipitates in NiTi alloys

Name	**Ti_3Ni_4**	**Ti_2Ni_3**	**$TiNi_3$**	**$TiNi_2$**
Space group	R3 (rhombohedral)	I4/mmm (tetragonal)	DO_{24} (hexagonal)	Fd3m (cubic)
Lattice parameter	$a = 0.67nm$ $\alpha = 113.8^\circ$	$a = 0.3095nm$ $c = 1.3585nm$	$a = 0.501nm$, $c = 0.8307nm$ $c/a = 1.6284$	$a = 1.132nm$
Reference	[236, 237]	[238]	[239]	[240]

Table 3. Deposition parameters for NiTi interlayers on 6061 T6 substrates and M2 steel substrates, before CrN deposition

Target Composition (at.%)	**Deposition Power (W)**	**Ar Pressure (Pa)**	**Substrate-Target Distance (mm)**	**Deposition Temperature (K)**
53.5 Ti 46.5Ni	200	0.35	63.5	483
Film Composition (at.%)	**Deposition Time (hour)**	**Base Pressure (Pa)**	**NiTi Film Thickness (μm)**	**Heat treatment**
51.7 Ti 48.3 Ni	0.45,1.5,2.5	5.2×10^{-5}	4.5, 9, 15	800K for 7200 ks

Table 4. Deposition parameters for NiTiCu interlayers on 6061 T6 substrates, before CrN deposition

Target Composition (at.%)	**Deposition Power (W)**	**Ar Pressure (Pa)**	**Substrate-Target Distance (mm)**	**Deposition Temperature (K)**
53.5 Ti 8 Cu 38.5 Ni	200	0.35	63.5	743
Film Composition (at.%)	**Deposition Time (hour)**	**Base Pressure (Pa)**	**NiTi Film Thickness (μm)**	**Heat treatment**
51.7 Ti 6.1 Cu 42.2 Ni	1.5	5.3×10^{-5}	9	793K for 7200 ks

Table 5. Deposition parameters for NiTi interlayers on 6061 T6 substrates, before DLC deposition

Target Composition (at.%)	**Deposition Power (W)**	**Ar Pressure (Pa)**	**Substrate-Target Distance (mm)**	**Deposition Temperature (K)**
53.5 Ti 46.5 Ni	200	0.53	63.5	523
Film Composition (at.%)	**Deposition Time (hour)**	**Base Pressure (Pa)**	**NiTi Film Thickness (μm)**	**Heat treatment**
51.7 Ti 48.3 Ni	2.5,3.5	2.0×10^{-4}	9,15,21	773K for 9000 ks

Table 6. Deposition parameters for NiTi interlayers on M2 tool steel substrates, before CrN deposition

Target Composition (at.%)	**Deposition Power (W)**	**Ar Pressure (Pa)**	**Substrate-Target Distance (mm)**	**Deposition Temperature (K)**
53.5 Ti 46.5 Ni 51.2 Ti 48.8 Ni	200	0.33	63.5	723
Film Composition (at.%)	**Deposition Time (hour)**	**Base Pressure (Pa)**	**NiTi Film Thickness (μm)**	**Heat treatment**
51.7 Ti 48.3 Ni 48.2 Ti 51.8 Ni	1,2	4.3×10^{-5}	6,12	793K for 7200 ks

Table 7. Phase transformation temperatures of thin film and bulk NiTi used in TWSME study

	Austenite start (A_S)	**Austenite finish** (A_f)	**Martensite start** (M_S)	**Martensite finish** (M_f)
Bulk NiTi	350K	404K	344K	287K
Thin Film NiTi	343K	390K	329K	282K

Table 8. Material parameters of NiTi and reference materials used in finite element modeling. (The "Ref" stands for reference material)

Phase transformation temperatures	**Austenite start** (A_S)	**Austenite finish** (A_f)	**Martensite start** (M_S)	**Martensite finish** (M_f)	
	318 K	338 K	323 K	303 K	
k_i parameters	k_1	k_2	k_3	k_4	
	0.1946	-7.784	0.1946	-10.622	
Transformation Strain	**Testing Temperature**	**Elastic Modulus** (NiTi and Ref)	**Plastic hardening slope h** (NiTi and Ref)	**Poisson's ratio**	**Yield stress** (Ref)
5%	90K	80 GPa	10 GPa	0.3	533.5 MPa

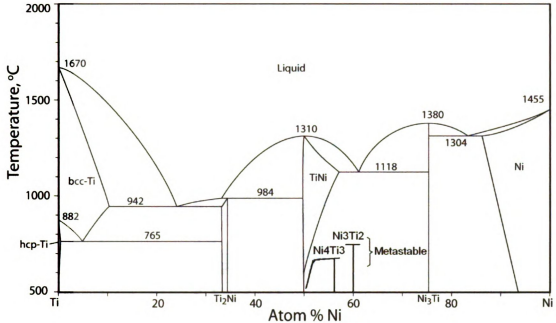

Figure 1. Phase diagram of a NiTi alloy by Massalski[241], to which the phase equilibrium between the B2 and Ti_3Ni_4 phases are added [242].

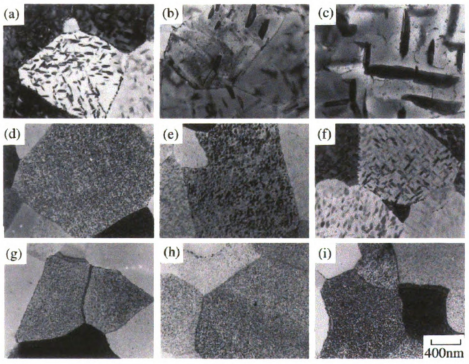

Figure 2. Transmission electron micrographs of Ti_3Ni_4 precipitates in 51.3at%NiTi thin films which were solution-treated at 973 K for 3.6 ks followed by age-treatment at 773 K for (a) 3.6 ks; (b) 36 ks and (c) 360 ks, at 673 K for (d) 3.6 ks; (e) 36 ks and (f) 360 ks, and at 573 K for (g) 3.6 ks; (h) 36 ks and (i) 360 ks (after reference [*51*]).

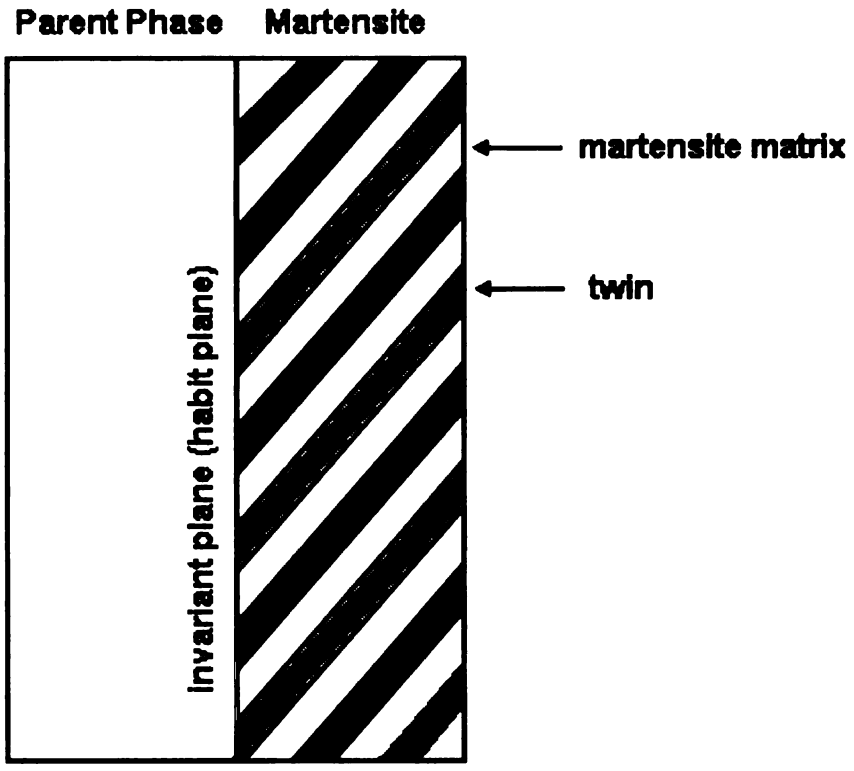

Figure 3. Schematic illustration of parent and martensite with invariant plane as a habit plane.

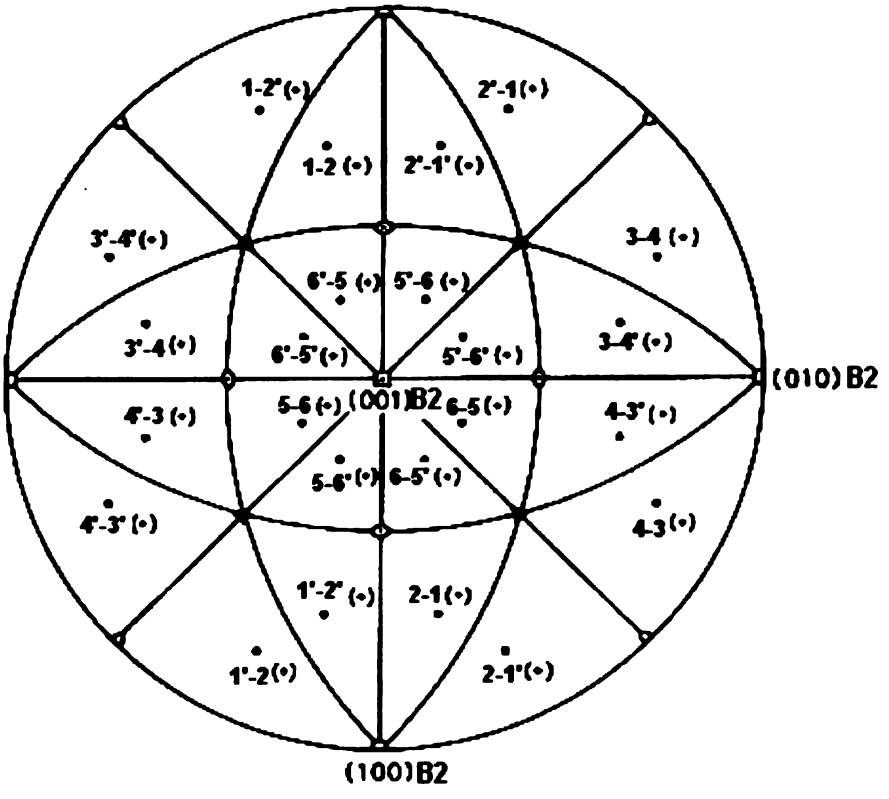

Figure 4. Stereographic projection of 24 habit plane variants from WLR theory, for <01−1> Type II twinning.

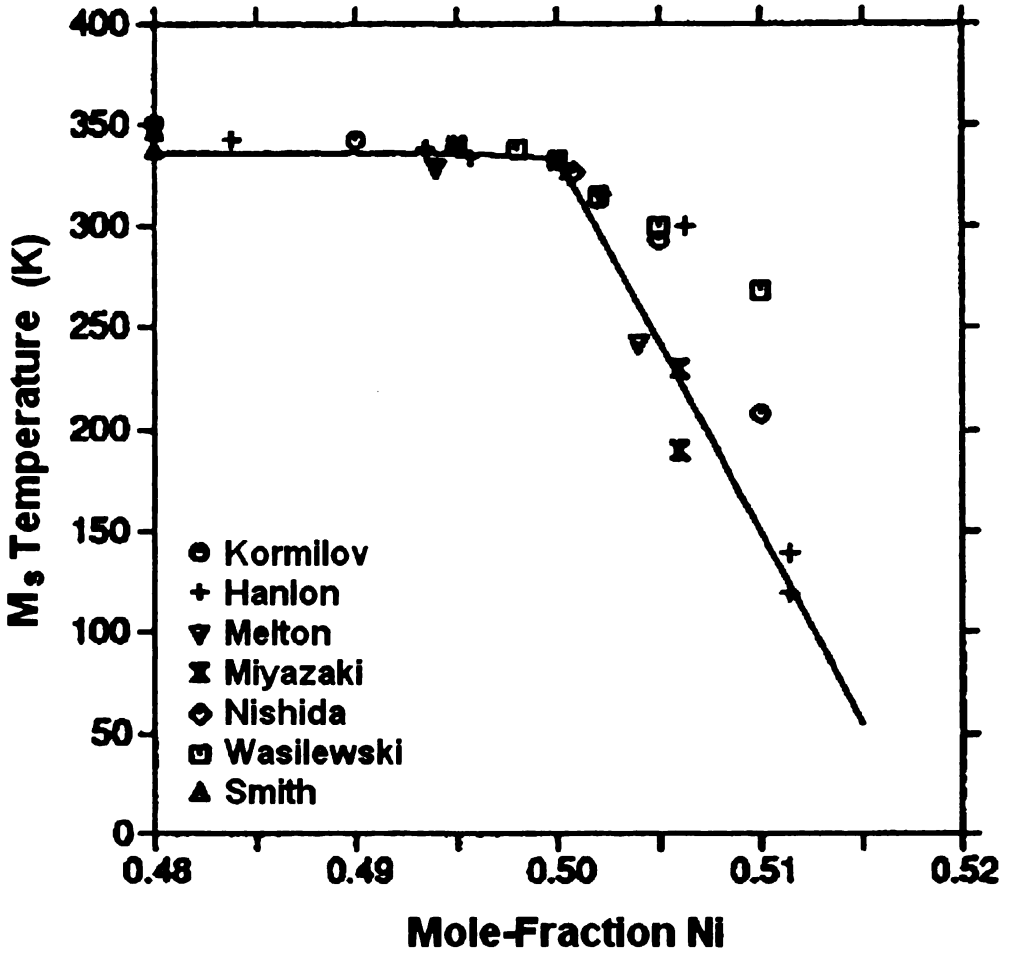

Figure 5. *Ms* temperature as a function of Ni content for binary NiTi alloys. Different data symbols represent data from different authors. The solid line is given by thermodynamic calculations (after reference [*34*]).

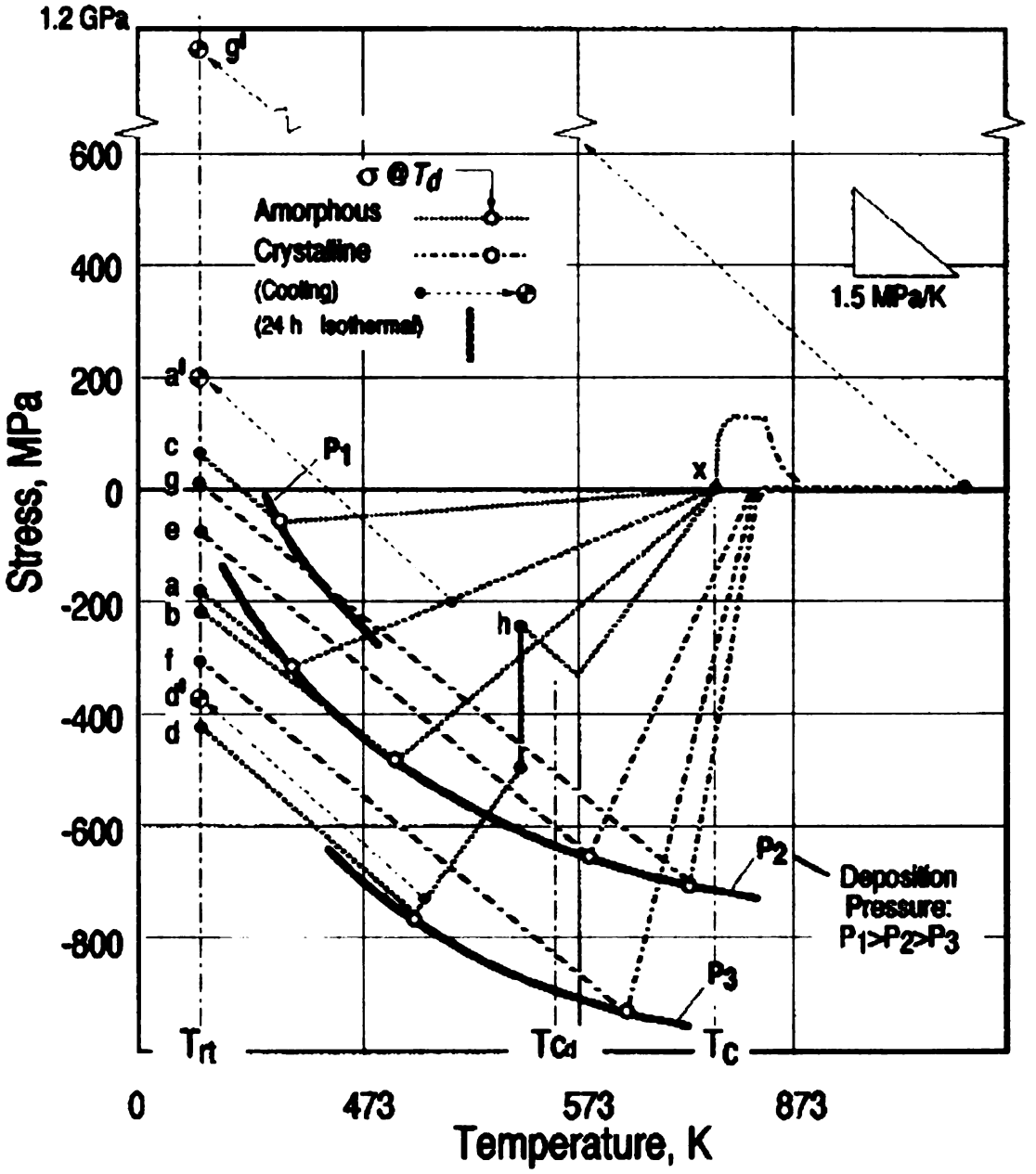

Figure 6. Schematic stress-temperature diagram for isochronal annealing of sputtered NiTi films on (100) silicon. Dark curves P1, P2 and P3 show the general intrinsic stress–deposition temperature characteristics for different pressures of the working gas. Trajectories a, b, c and d are for amorphous films deposited at different pressures and at temperatures below T_{cd}, the minimum in-situ crystallization temperature. Isochronal crystallization occurs at T_c giving a transient tensile stress spike at x. Curve d additionally shows the effect of an isothermal hold inserted in the isochronal sequence. Trajectories e, f and g are for crystalline films deposited above T_{cd}. Cooling from any point on a trajectory generally proceeds along a path with slope 1.5 MPa/K, to points such as d`, a` and g`, allowing a wide range of stress levels to be obtained at T_{rt}. (after reference [*58*])

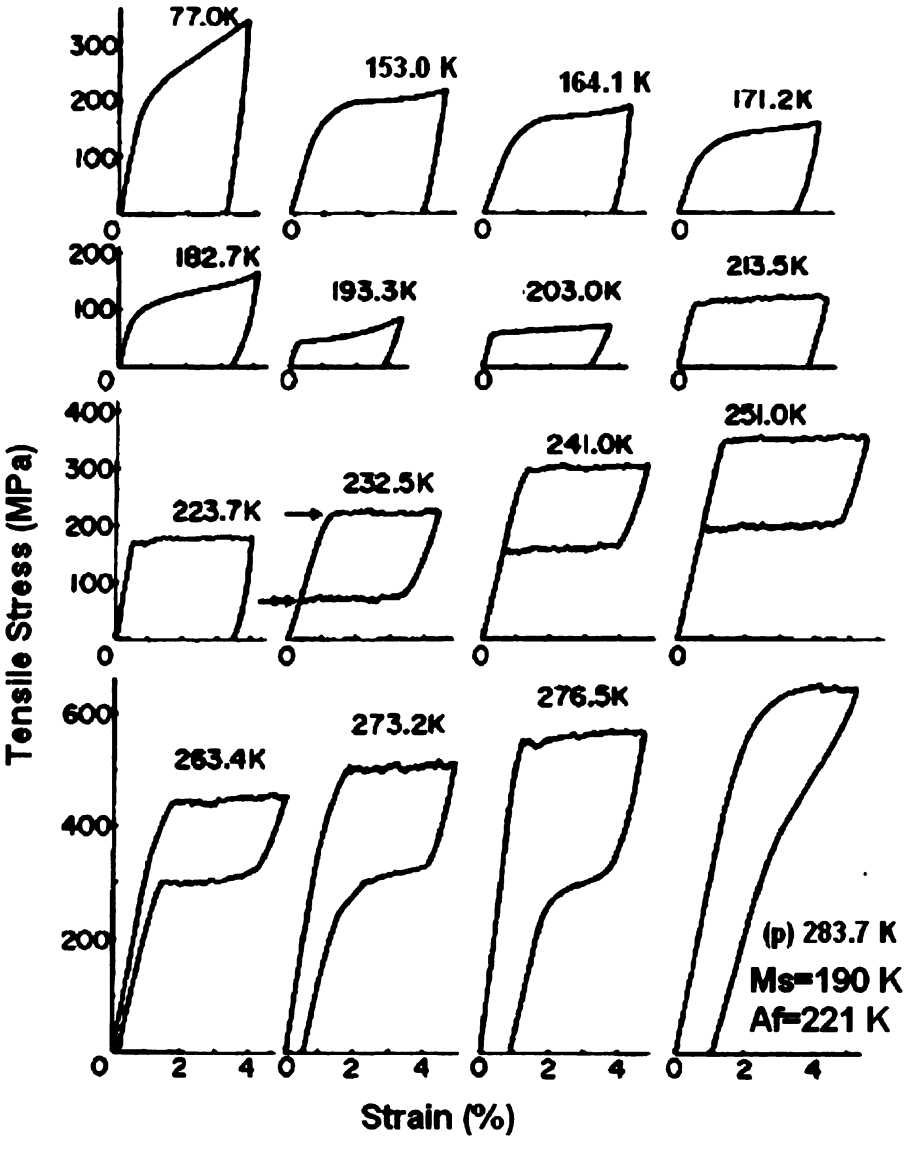

Figure 7. Stress–strain curves as a function of temperature of 50.6 at.% NiTi alloy, which was solution-treated at 1273 K for 1 h. The critical stress for inducing martensites and that for reverse transformation are indicated by an arrow (→) and by a double arrow (→→) in (j), respectively. (after reference [*68*])

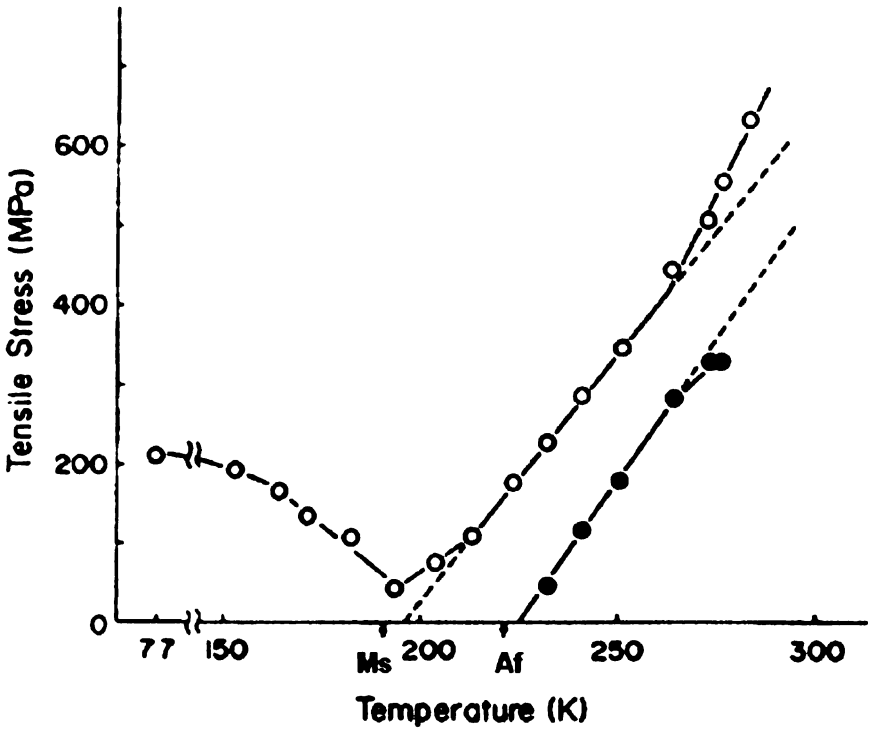

Figure 8. Critical stress as a function of temperature for inducing martensites (open circles) and for reverse transformation (solid circles), which were plotted from the data in Figure 7. (after reference [*68*])

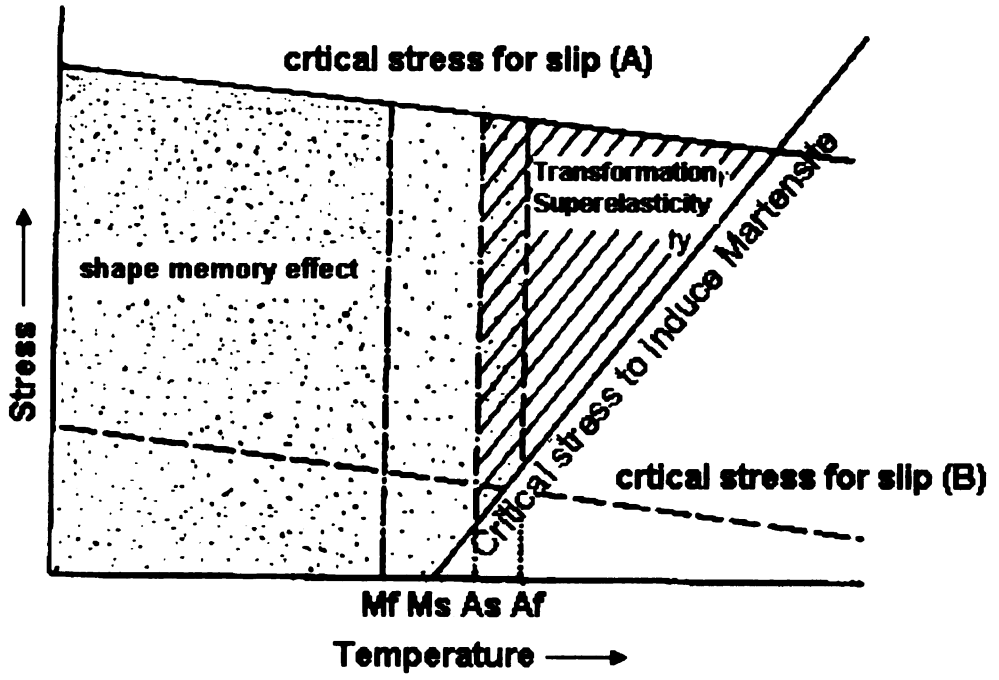

Figure 9. Schematic representation for the appearance of the shape memory effect and superelasticity in temperature–stress space. (after reference[*4*])

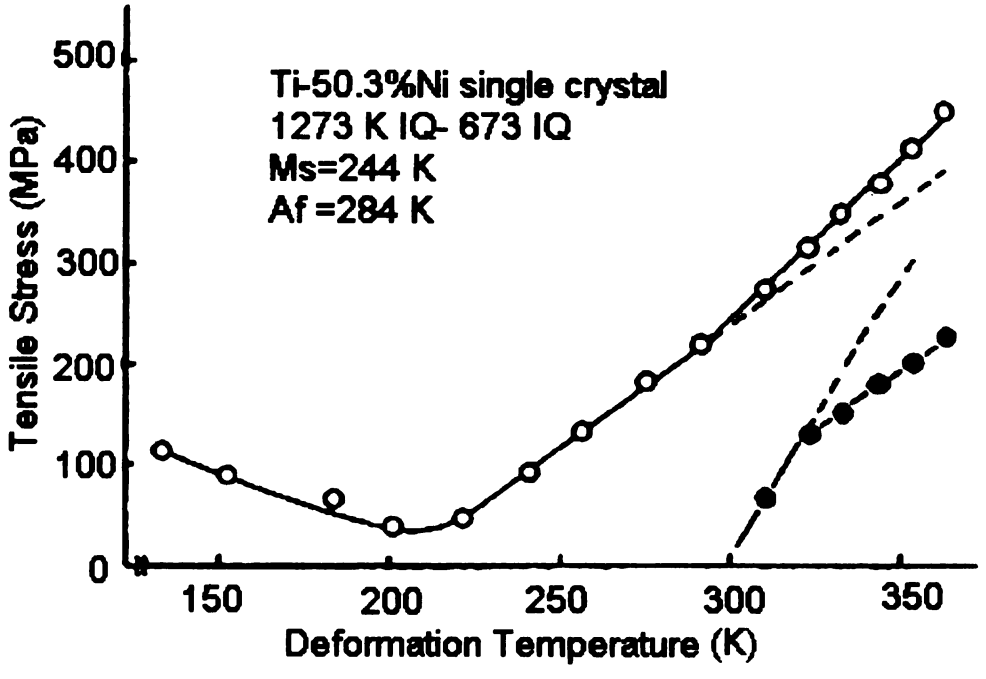

Figure 10. Critical stress for inducing martensites and for reverse transformation of a 50.3at.%NiTi single crystal, which was solution-treated at 1273 K for 1 h followed by aging at 673 K for 1 h. (after reference [*243*].)

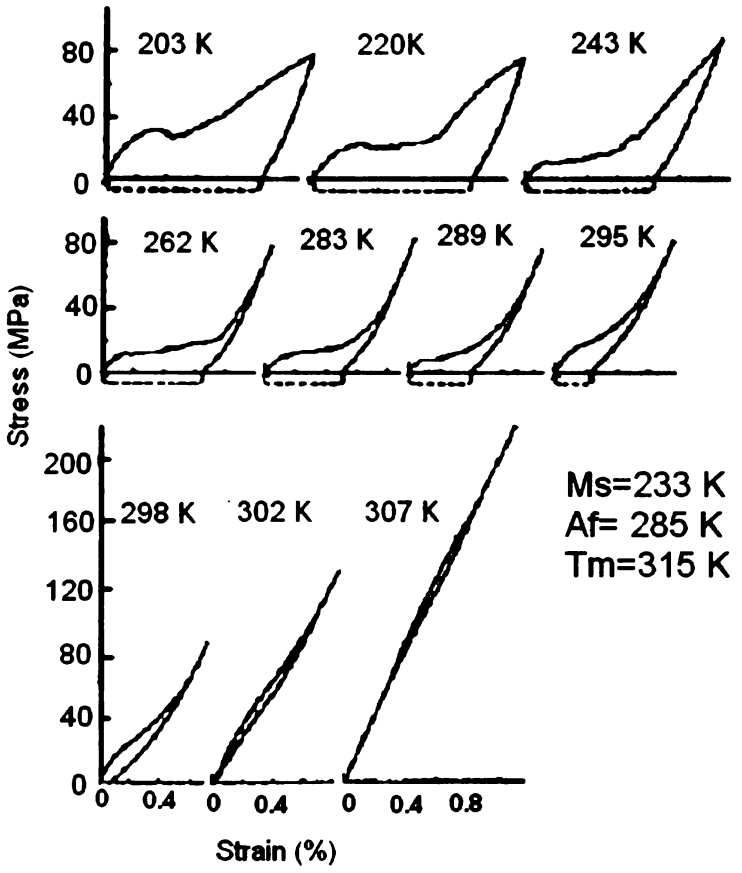

Figure 11. Stress–strain curves as a function of temperature of a Ti–50.5Ni single crystal, which was aged at 673 K for 1 h after solution-treatment. The curves are related with R-phase transformation or deformation of R-phase. T'_m=Rs. (after reference [*72*])

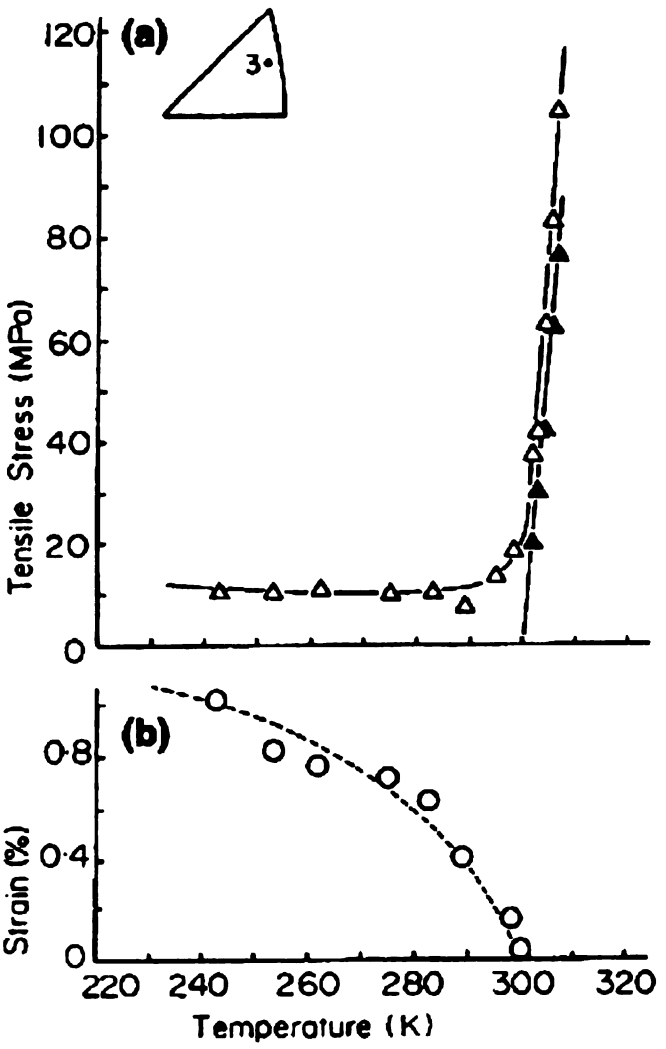

Figure 12. (a) Critical stresses for R-phase deformation and superelasticity, and (b) the recoverable strain of R-phase superelasticity, which is a function of temperature. (after reference [*72*])

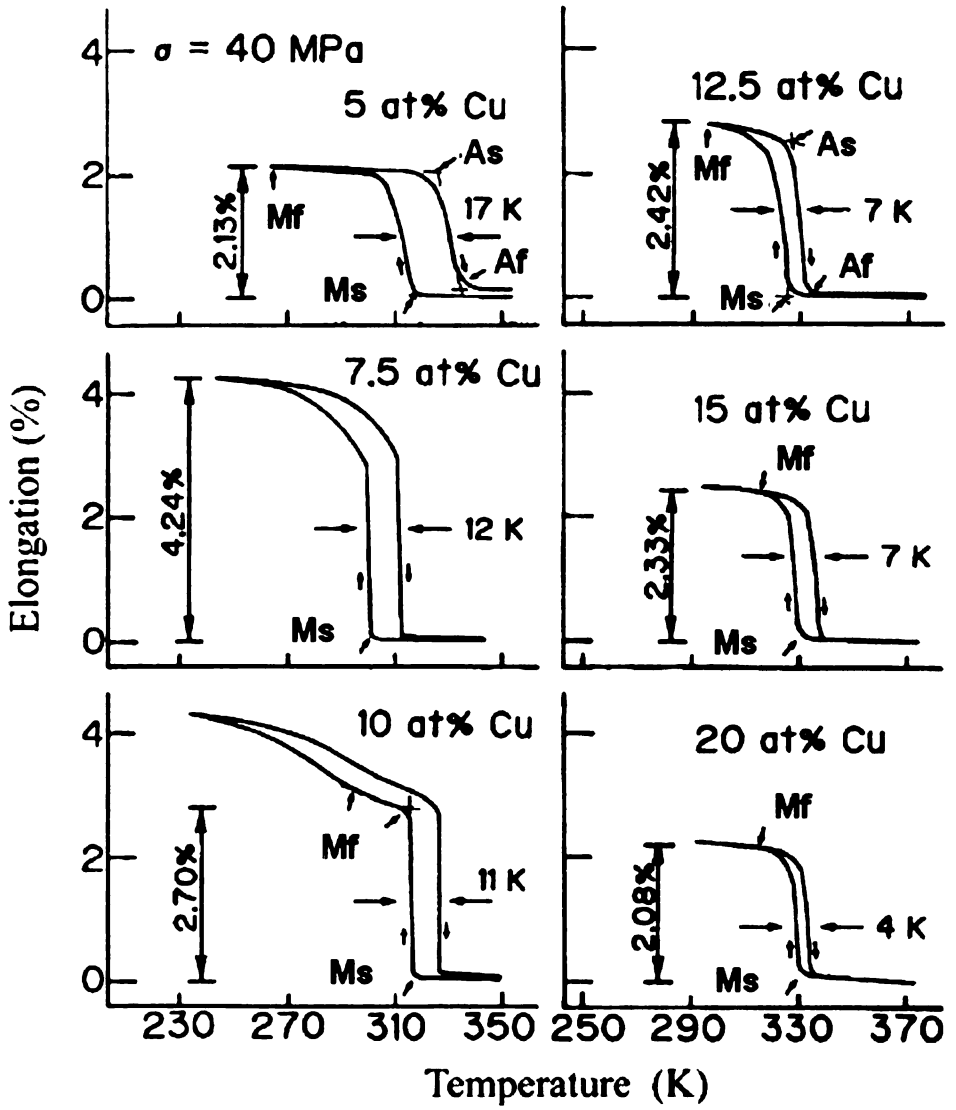

Figure 13. Elongation vs. temperature curves under 40 MPa load for Ti–Ni–Cu alloys with various compositions indicated. (after reference [73]).

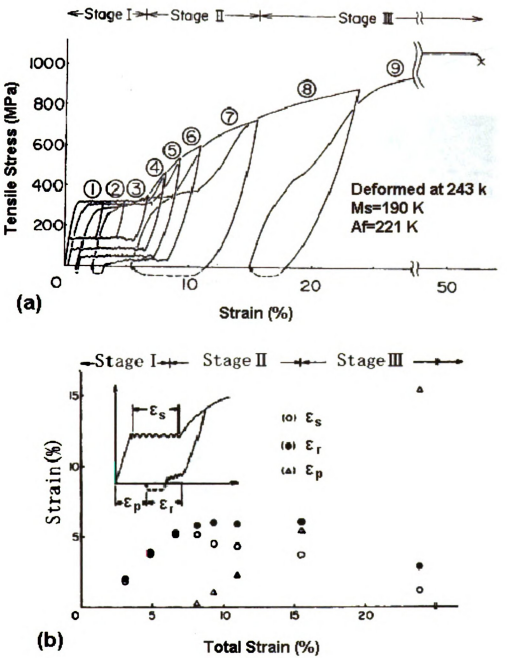

Figure 14. Stress–strain curves of 50.6 at.%NiTi alloy, which was deformed at 243 K ($>A_f$). The alloy was solution-treated at 1273 K for 1 h. Dashed lines represent the recovered strain upon heating to 373 K. The symbol (x) represents the fracture point. (b) Plots of various strains in (a) as a function of total strain. (after reference [*68*])

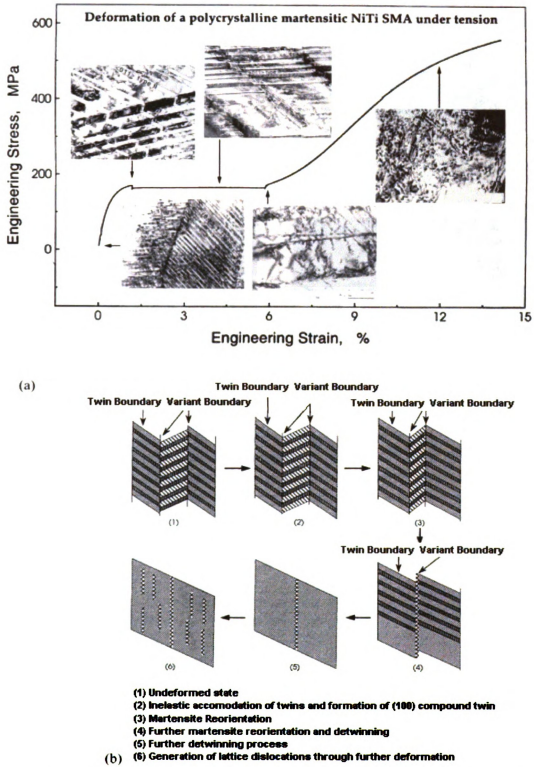

Figure 15. Deformation stage of martensitic NiTi alloy sample (after reference [78]).

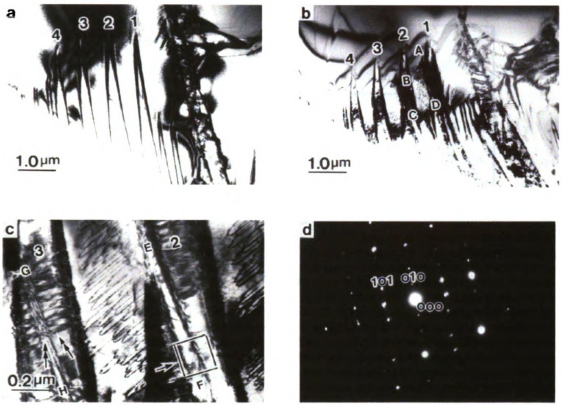

Figure 16. TEM images of in-situ tensile loading of superelastic NiTi. (a) martensite plates 1, 2, 3, 4 formed at 118 μm displacement. (b) High density of looped dislocations (marked by ABCD) formed at 150 μm displacement. (c) Magnified photo of the area between martensite plates 1, 2 and 3, in (b). (d) Diffraction pattern corresponding to the area indicated by single-headed arrow in (c). (After reference [79].) The martensite plate 2 shows some detwinning at the lower part; but the plate 3 does not seems to detwin, even though dislocations have been generated.

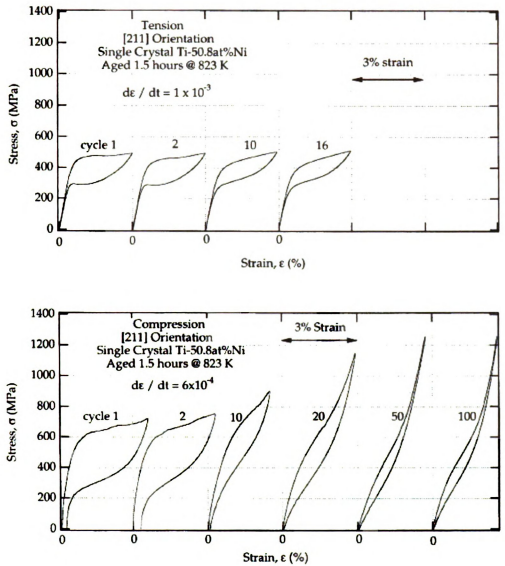

Figure 17. (above) Tensile cyclic stress–strain response of single crystal NiTi oriented in the [112] direction. The test temperature is above the A_f transformation temperature. (below) Compressive cyclic stress–strain response of single crystal NiTi oriented in the [112] direction. The test temperature is above the A_f transformation temperature. (after reference [76])

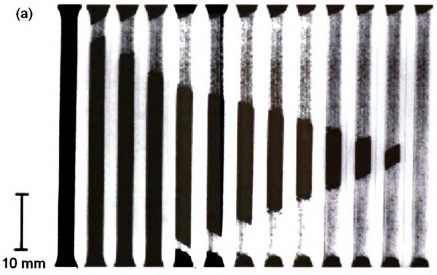

Figure 18. Observation of Luders deformation by photography for Ti-50.5Ni alloy. Black regions represent the parent phase, and lighter colored regions martensite. The strain increases with increasing numbers from (1) to (13). (after reference [83]).

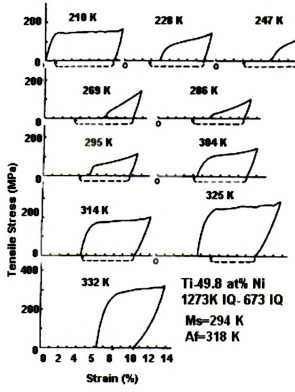

Figure 19. Effect of thermomechanical treatment on the stress–strain curves as a function of deformation temperature for 49.8at.%NiTi alloy. Solution-treatment at 1273 K for 1 h followed by annealing at 673 K for 1 h. (after reference [244])

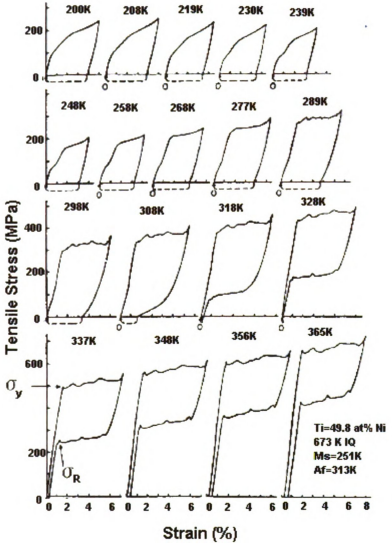

Figure 20. Effect of thermomechanical treatment on the stress–strain curves as a function of deformation temperature for 49.8at.%NiTi alloy. Annealed at 673 K for 1 h immediately after cold-working. (after reference [244])

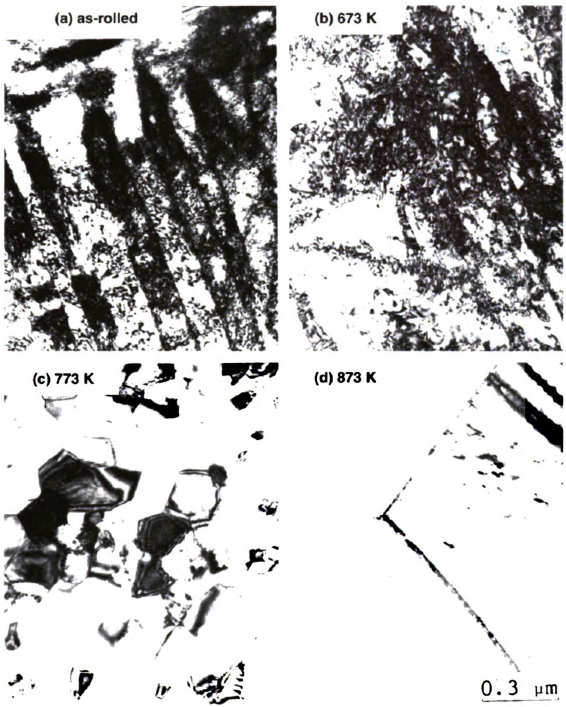

Figure 21. TEM images of 49.8at.% NiTi alloy, which were annealed for 1 h at various temperatures indicated after cold-working; (a) as cold-worked, (b) at 673 K, (c) at 773 K and (d) at 873 K. (after reference [245])

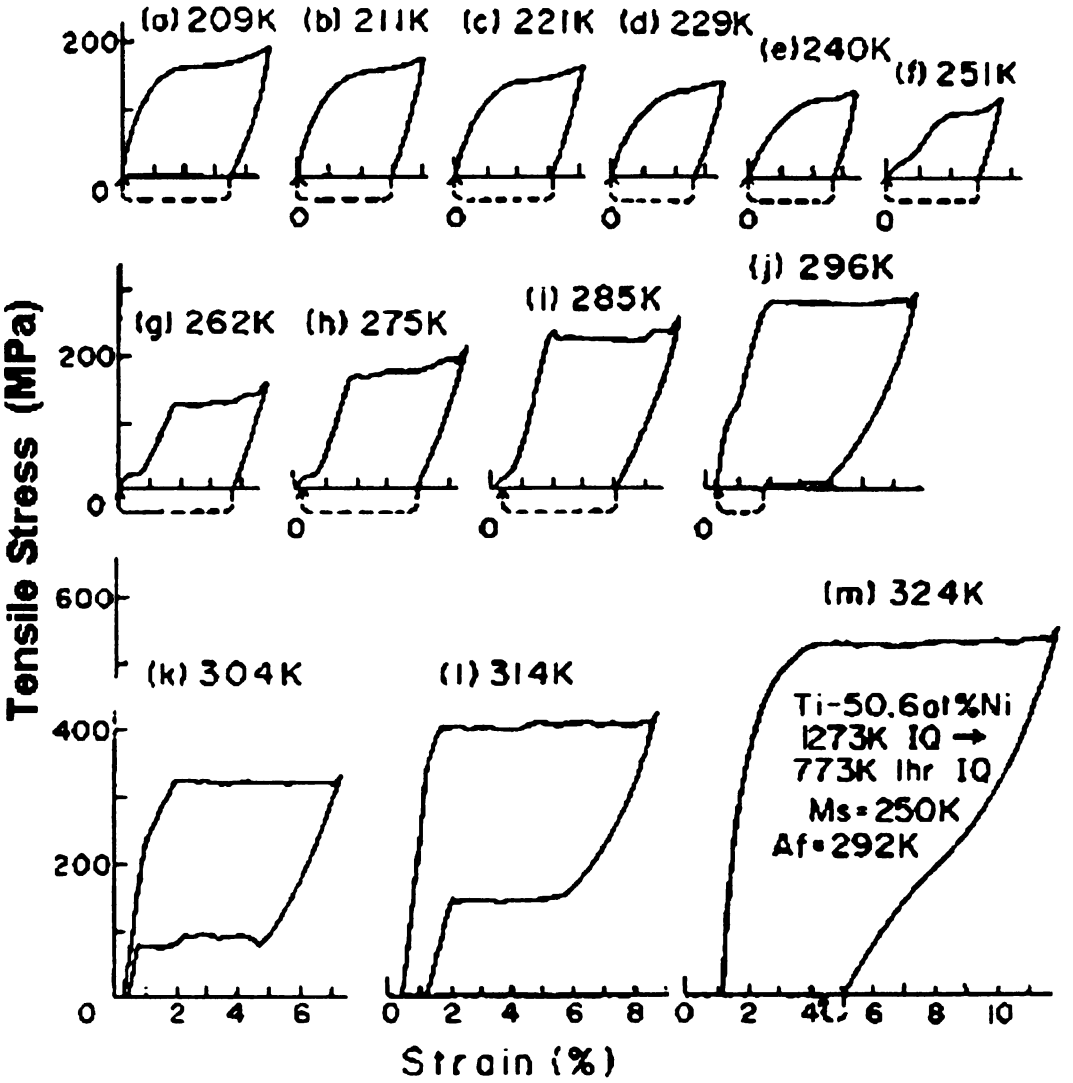

Figure 22. Stress–strain curves as a function of testing temperature of 50.6at.%NiTi alloy, which was aged at 773 K for 1 h after solution-treatment at 1273 K for 1 h. (after reference [245])

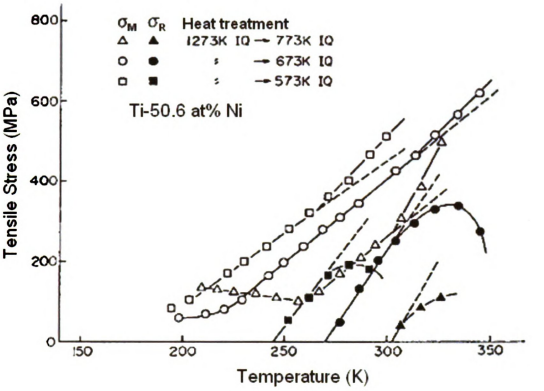

Figure 23. Effect of aging temperature on the critical stresses for inducing martensites and for reverse transformation in a 50.6at.% NiTi alloy, which was aged at various temperatures for 1 h after solution treatment. (after reference [244])

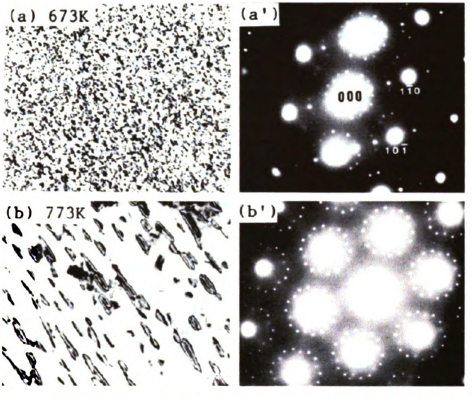

Figure 24. TEM images and corresponding diffraction patterns of 50.6at.% NiTi alloy specimens, which was aged at various temperatures after solution-treatment at 1273 K for 1 h; (a and a') at 673 K, (b and b') at 773 K. (after reference [245])

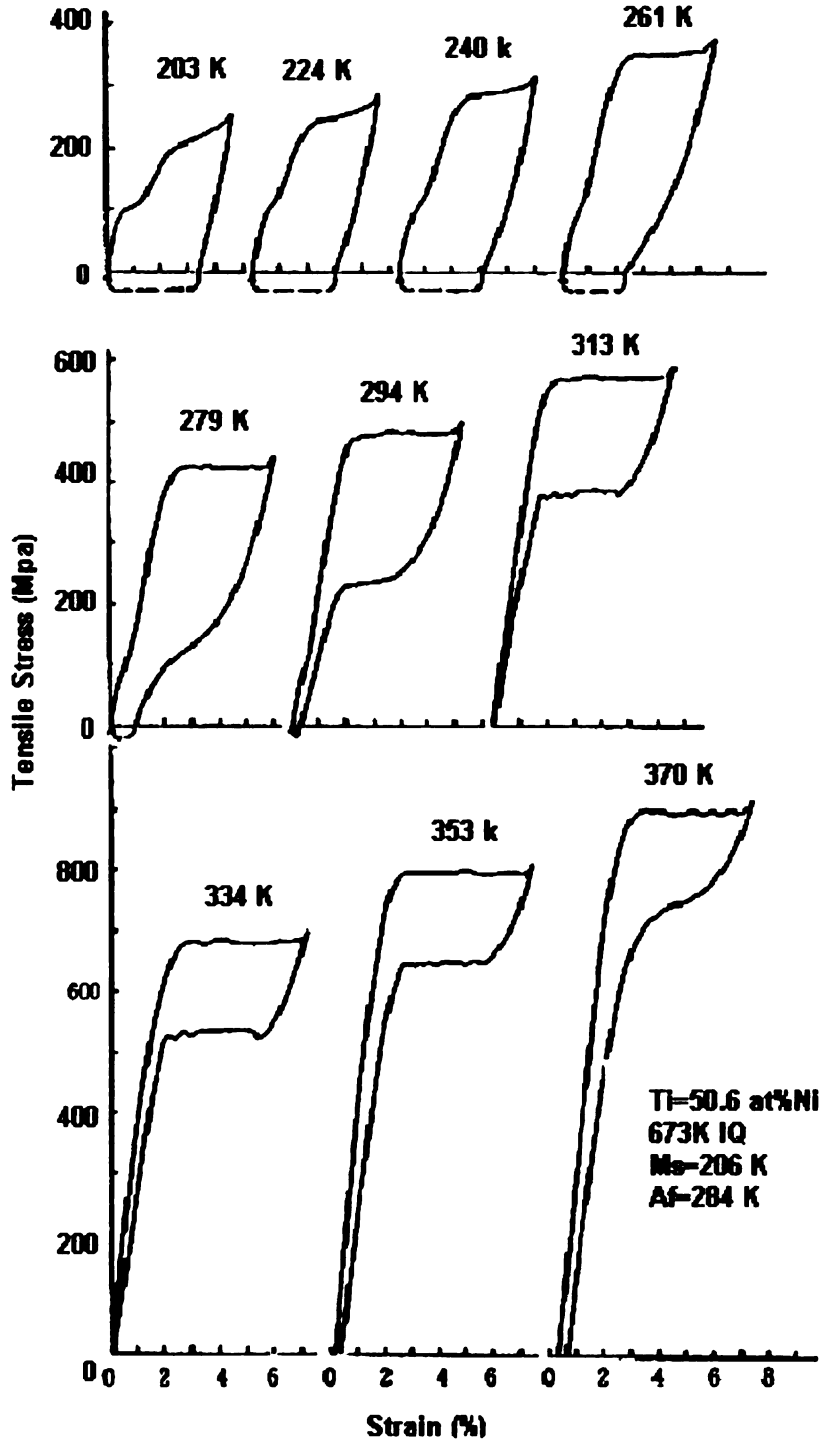

Figure 25. Stress–strain curves as a function of deformation temperature of 50.6at.%NiTi alloy, which was aged at 673 K immediately after cold-working. (after reference [245])

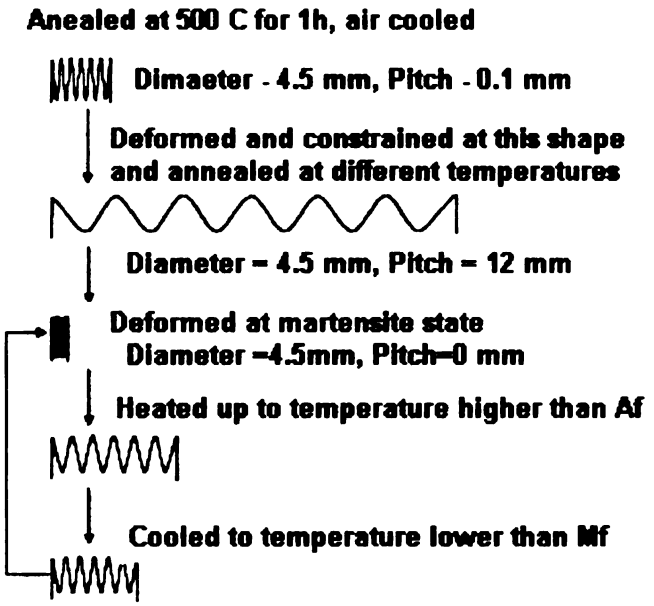

Figure 26. The procedure of processing TWSME TiNi SMAs spring (after reference [87])

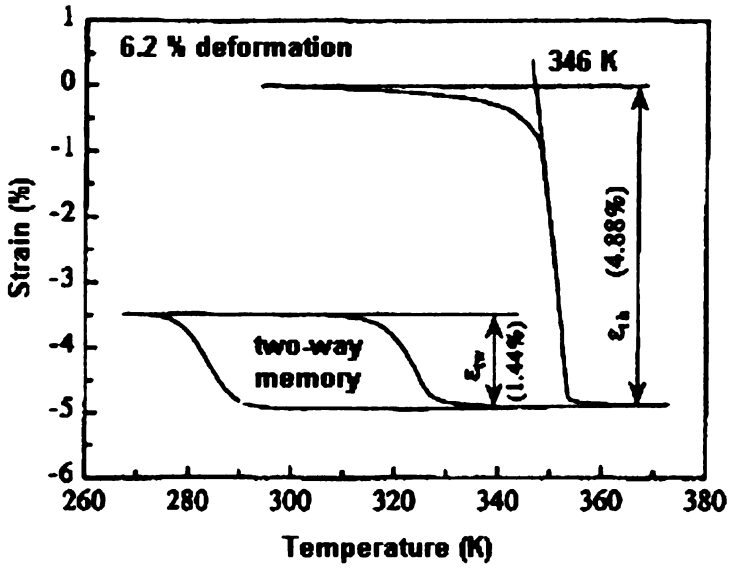

Figure 27. The two-way shape memory effect obtained after a single deformation by 6.2% of equiatomic NiTi alloy (after reference [102]).

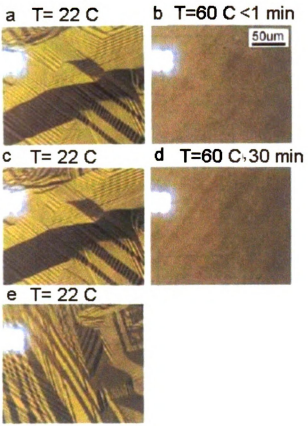

Figure 28. Optical microscopy verification of the predicted microstructure memory for an aged $Au_{51}Cd_{49}$ martensite and its disappearance after aging in the parent phase. (a) Domain pattern of the aged martensite (aged at room temperature for six months). The sample is heated up to (b) parent phase (60 °C), and immediately cooled down to (c) martensite. Then the sample is heated up again to (d) parent phase (60 °C) and aged for 30 minutes, followed by cooling down to (e) martensite. (after reference [104]).

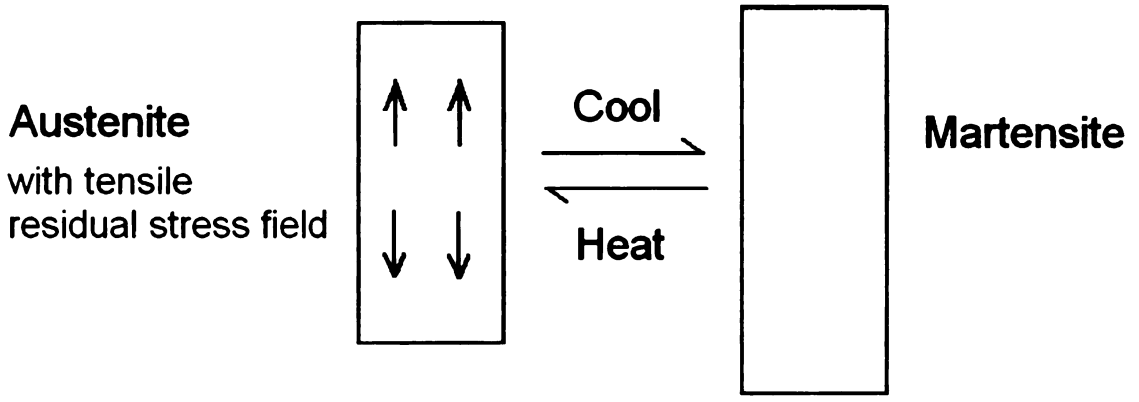

Figure 29. TWSME due to internal tensile residual stress: elongation during cooling and shrinkage during heating.

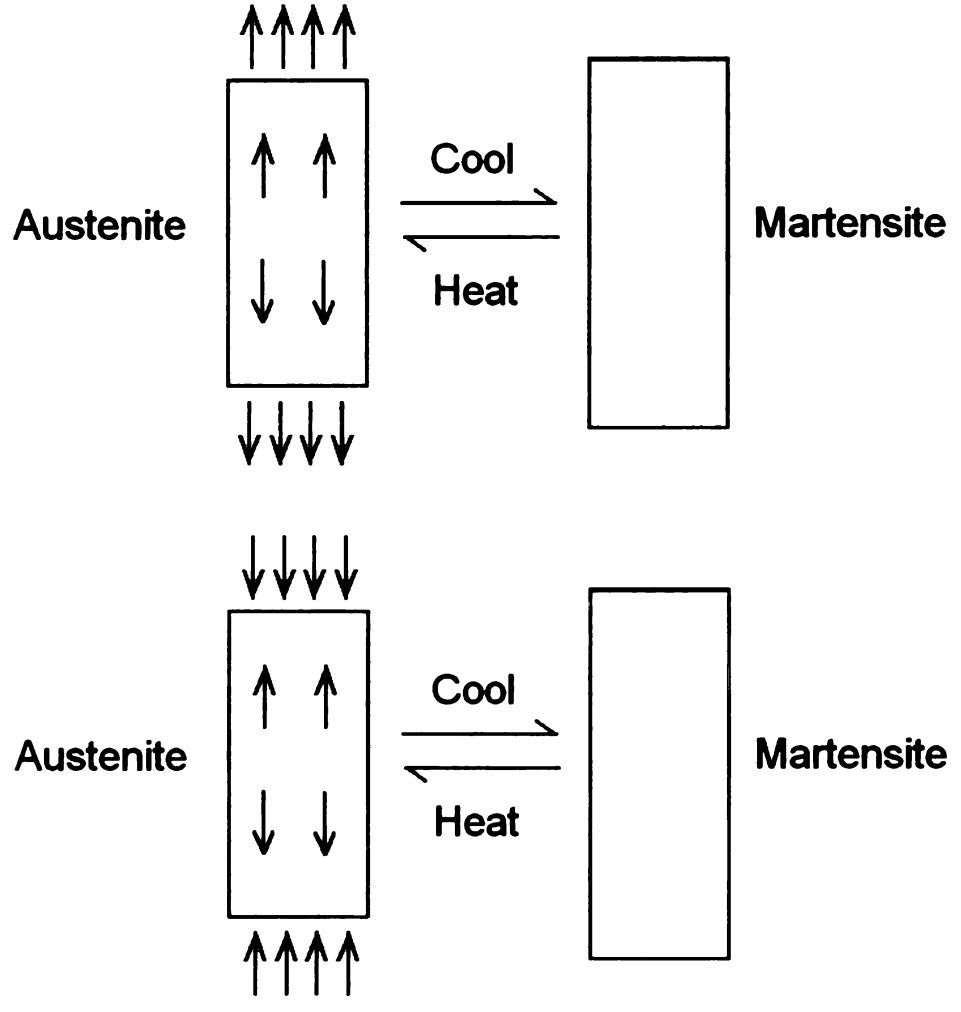

Figure 30. External Stress and Internal Compressive Stress Field. The tensile external stress increases the internal tensile stress, elevating phase transformation temperatures but compressive external stress decreases the internal tensile stress.

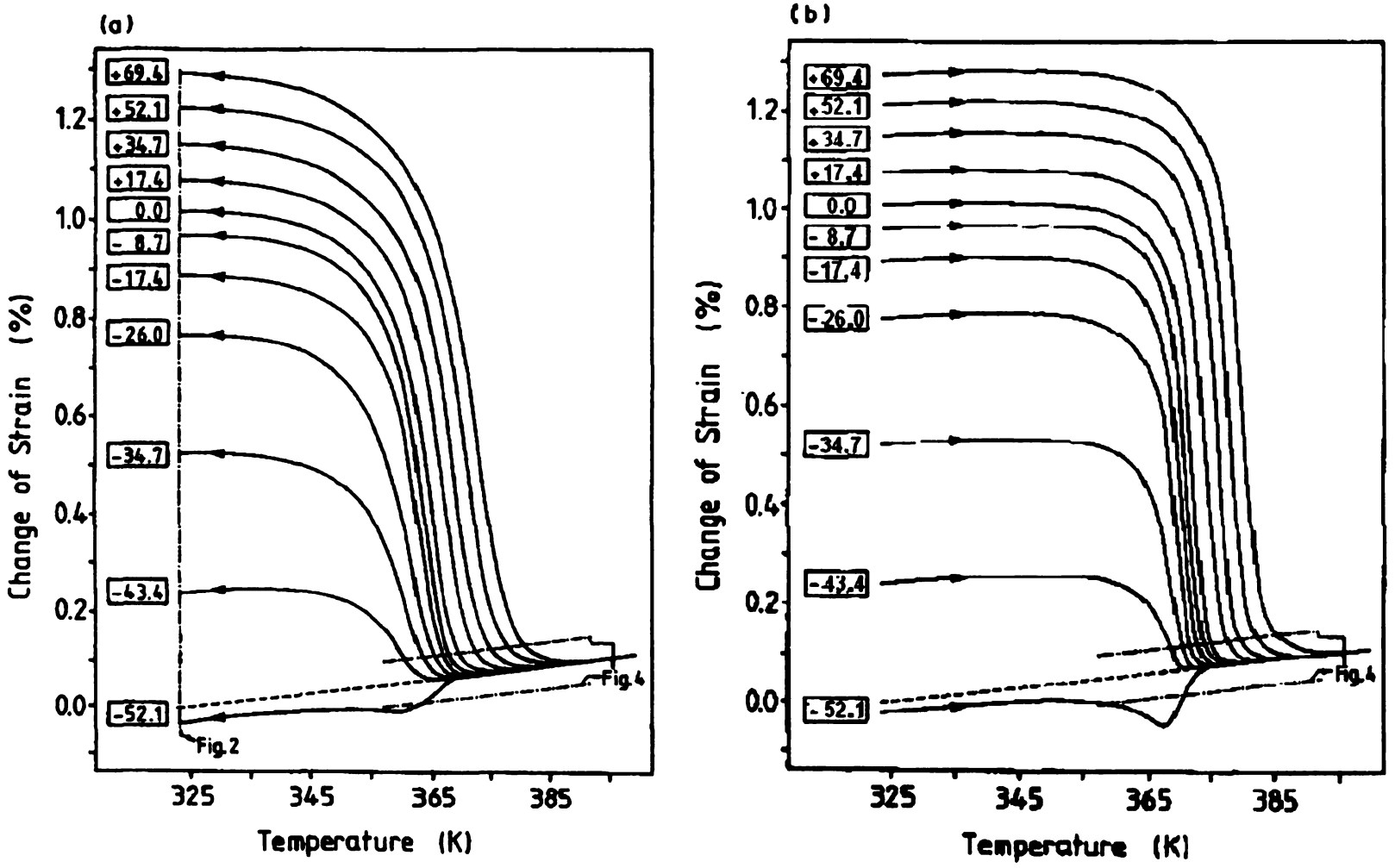

Figure 31. Strain-temperature curves during (a) cooling and (b) heating through the transformation region of a trained specimen at different external stresses. The external stresses are indicated in the rectangulars (in MPa). The pure elastic deformation which is caused by the loading in the austenitic condition has been subtracted to obtain a common curve in the austenitic condition.

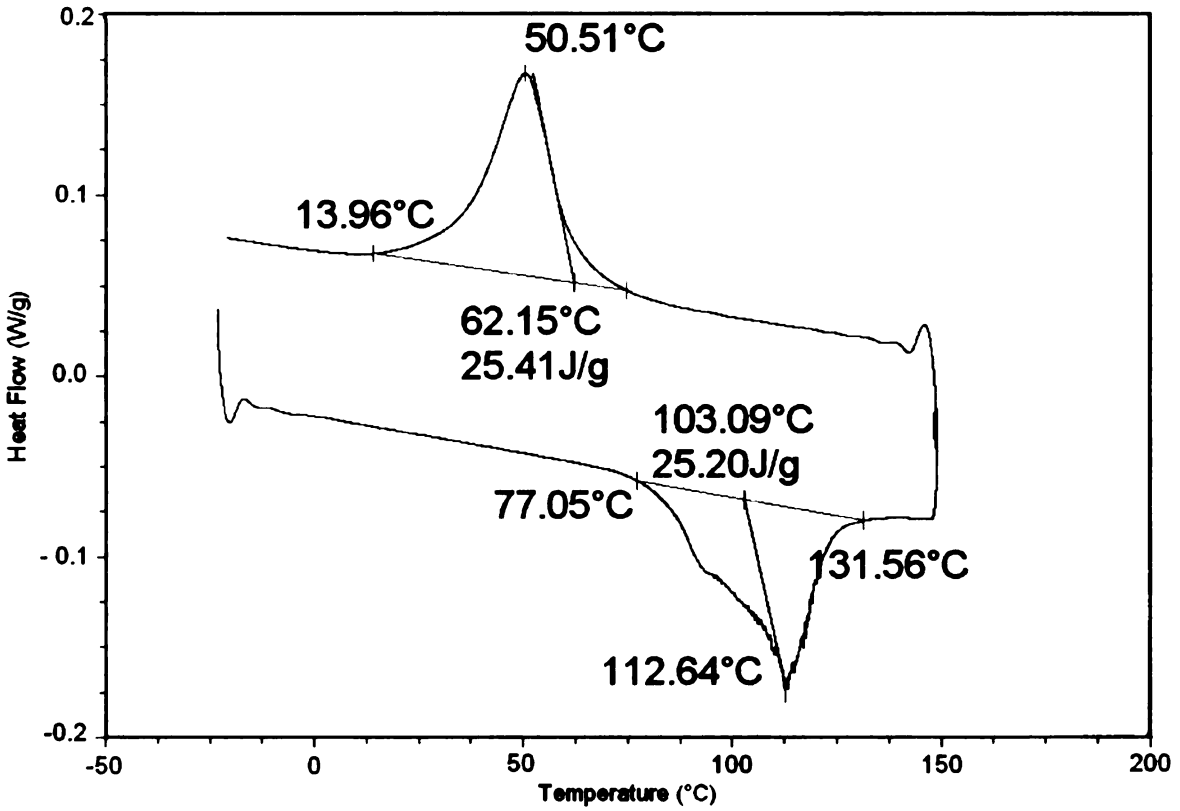

Figure 32. DSC curves of bulk NiTi samples used in TWSME study

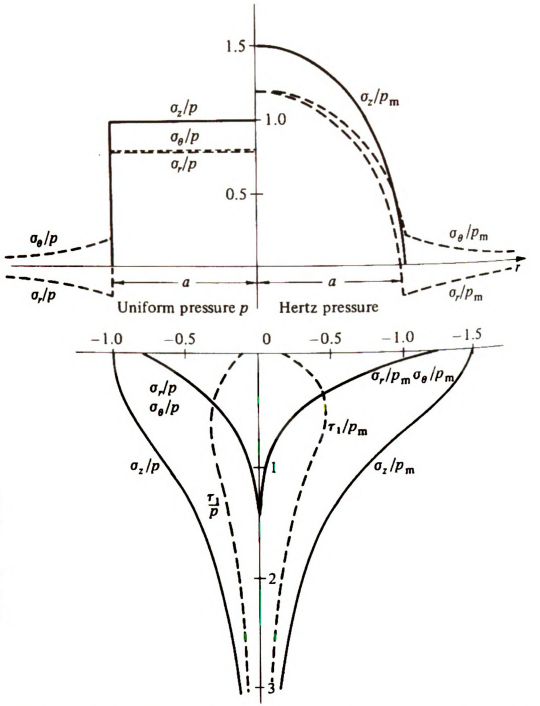

Figure 33. Stress distributions at the surface and along the axis of symmetry caused by (left) uniform pressure and (right) Hertz pressure acting on a contacting radius a (after K.L. Johnson, Contact Mechanics, Cambridge University Press, 1985, pp.94, [108]).

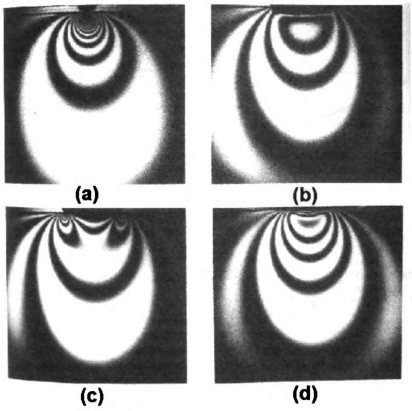

Figure 34. Two-dimensional photo-elastic fringe patterns (contours of shear stress). (a) point load; (b) uniform pressure; (c)rigid flat punch; (d) contact of cylinders. (after reference [108], pp.103).

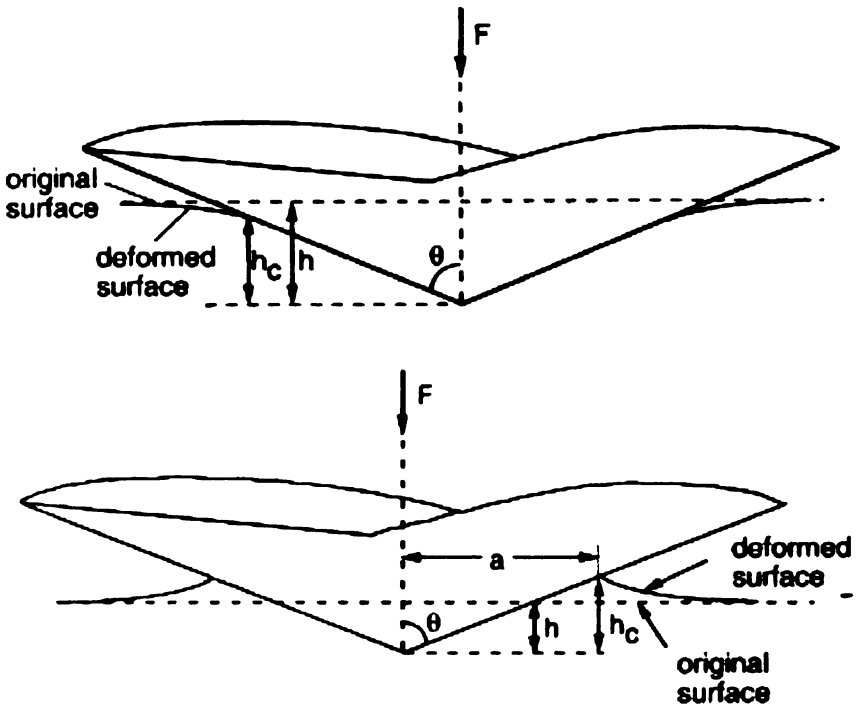

Figure 35. The "pile-up" (above) where contact radius is larger than linear case and, "sink-in" (below) where contact radius is smaller.

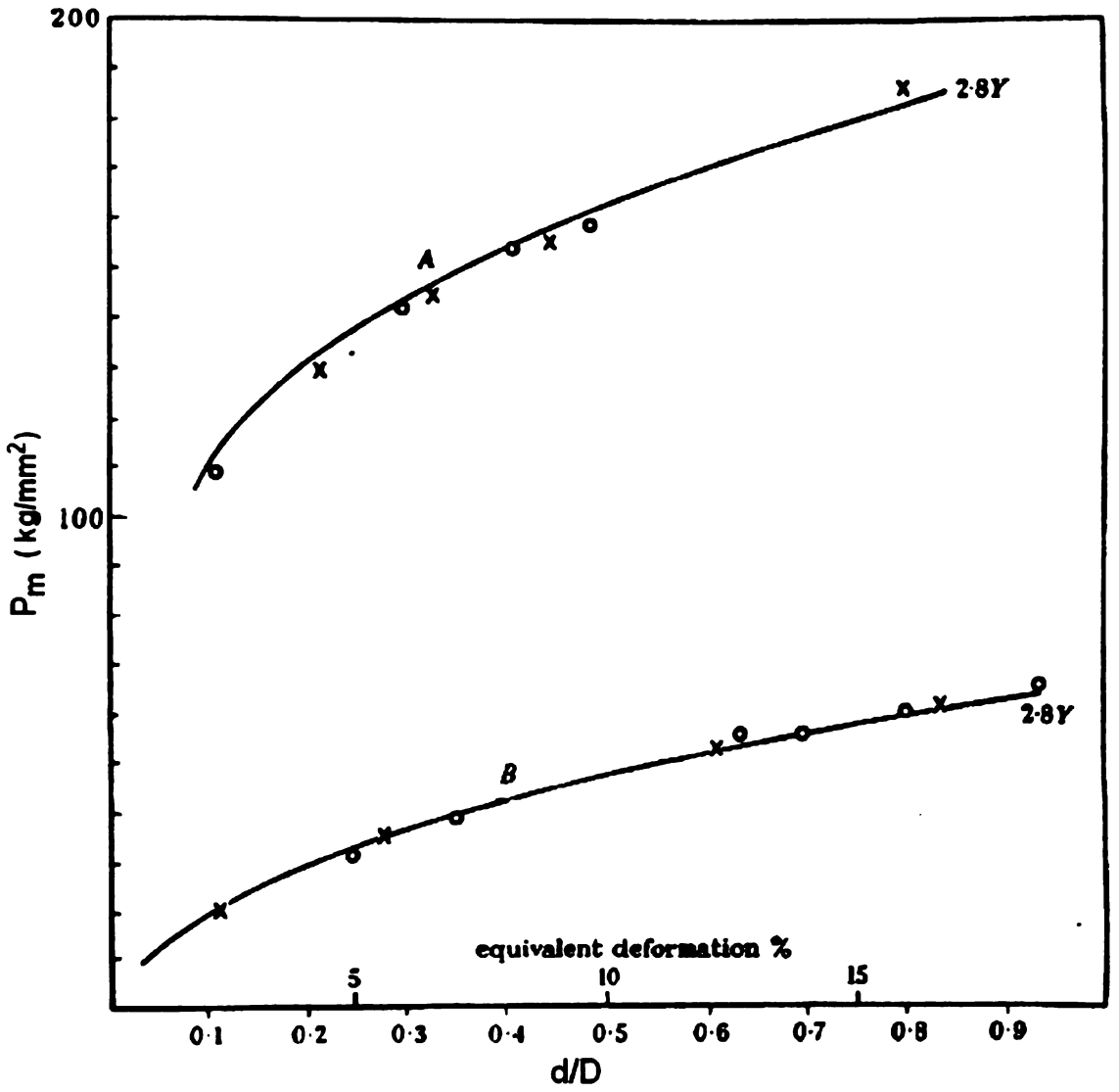

Figure 36. Representative strain vs. hardness in spherical indentation, and its correlation with true stress-true strain in uniaxial tension. Metal A is steel and metal B is copper. (after reference [*111, 112*])

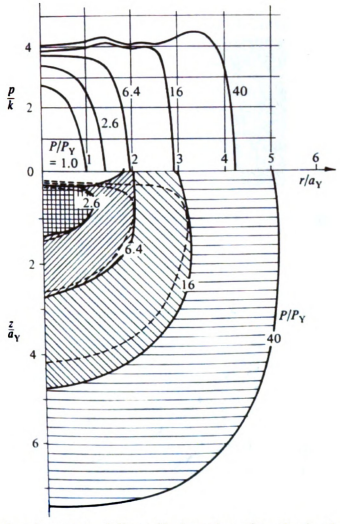

Figure 37. Finite element modeling of indentation of an elastic-plastic half space by a rigid sphere: development of the plastic zone. Broken line: contour of J_2. P_Y is the normal load needed to first initiate plastic flow. (after reference [*114*])

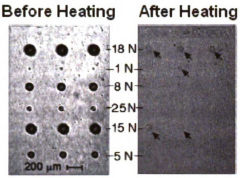

Figure 38. Recovery of spherical indents in NiTi alloy by the shape memory effect. (after reference [*231*])

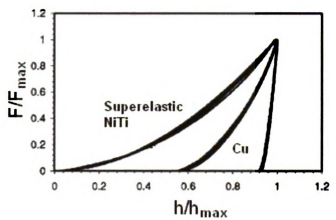

(a)

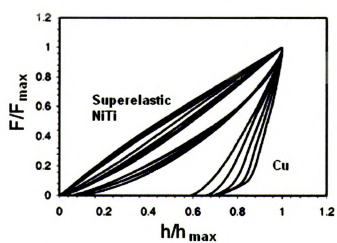

(b)

Figure 39. Load-displacement curves of (a) Berkovich and (b) spherical indentations in SE NiTi. (after reference [*117*])

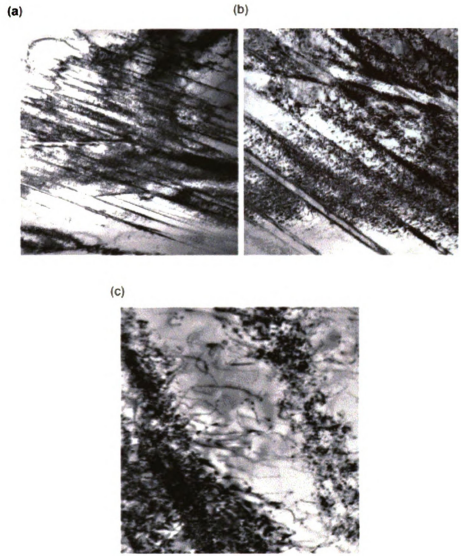

Figure 40. TEM images from the indent-affected zone in 50.9at%NiTi single crystals. Images (a) to (c) were taken adjacent to the same indent at different magnifications. (after reference [*118*]).

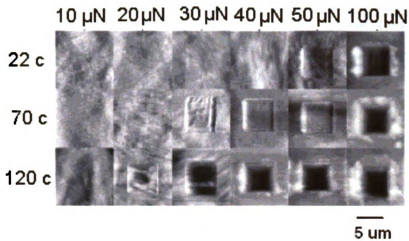

Figure 41. Images of wear marks on NiTi after 200 cycles of scanning scratch under different normal loads and temperatures. A_f is 16 °C. (after reference [144])

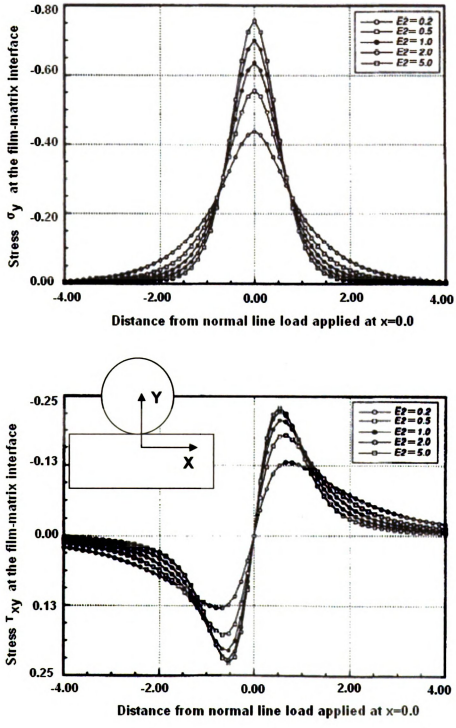

Figure 42. Calculated stresses due to an isolated unit normal line load applied at the origin as a function of substrate modulus E_2. Variation of bearing stress σ_y and shear stress τ_{xy} at the film-substrate interface are shown for a 1000 nm film with a reference elastic modulus E_1=1. (after reference [*198*])

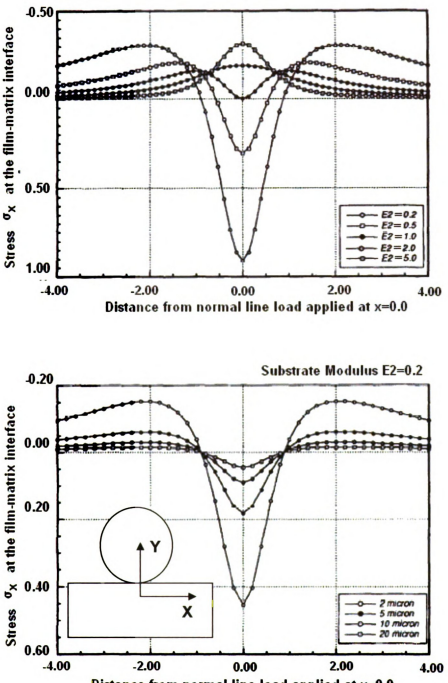

Figure 43. Calculated tensile stress σ_x at the film-substrate interface for a 1000 nm film with a reference elastic modulus E_1=1 for a unit normal line load at the origin. Substrate modulus E_2 is varied in the upper figure. The effect of varying the film thickness on the flexure stress is shown in the lower figure for a substrate of modulus E_2=0.2. (after reference [*198*])

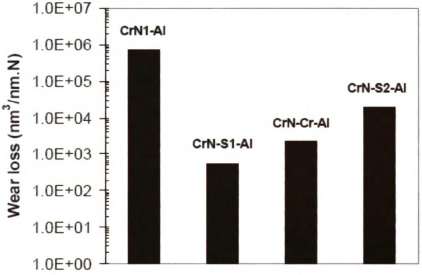

Figure 44. Wear test results of samples with1μm CrN coating and with: (from left to right) no interlayer, with 4 μm SE NiTi interlayer (S1), 4 μm Cr interlayer and 4μm SMA NiTi interlayer (S2). (after reference [3])

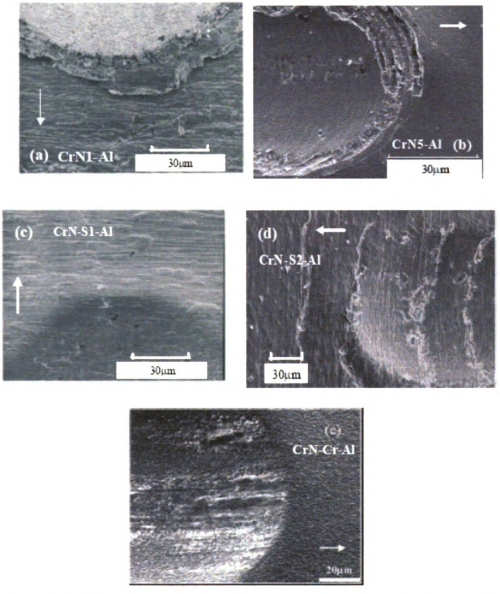

Figure 45. SEM Images of scratch track end with (a) 1μm CrN coating, no interlayer, (b) 5μm CrN coating no interlayer, (c) 1μm CrN coating 4μm SE NiTi interlayer, (d) 1μm CrN coating and 4μm SMA NiTi interlayer and (e) 1μm CrN coating and 4μm Cr interlayer. (after reference [*3*])

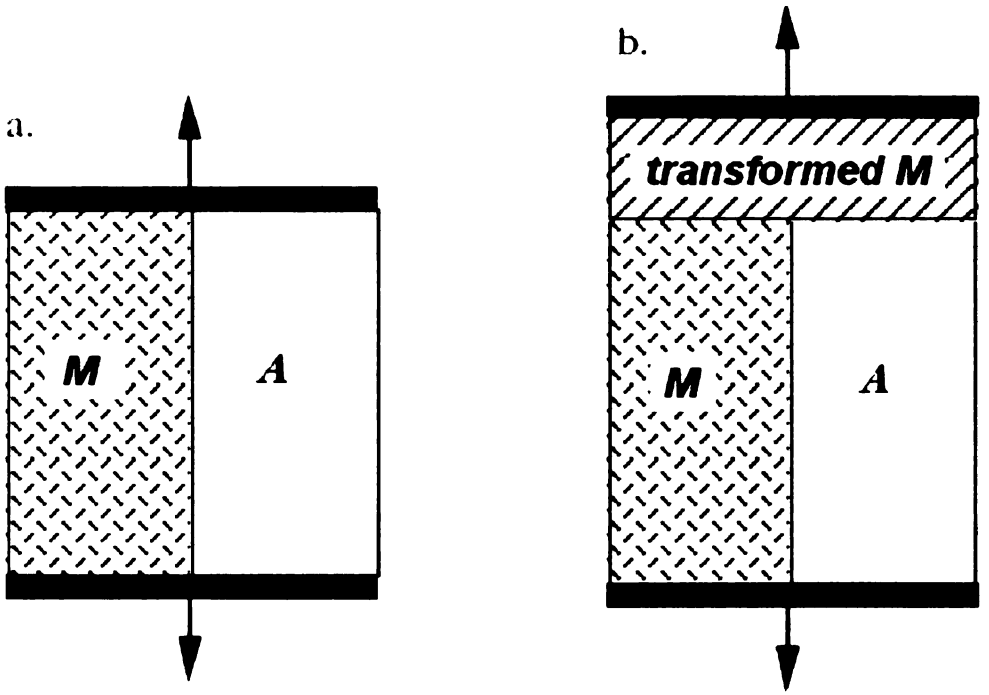

Figure 46. Vogit (parallel) model for stress induced martensite in austenite phase. (after reference [*204*])

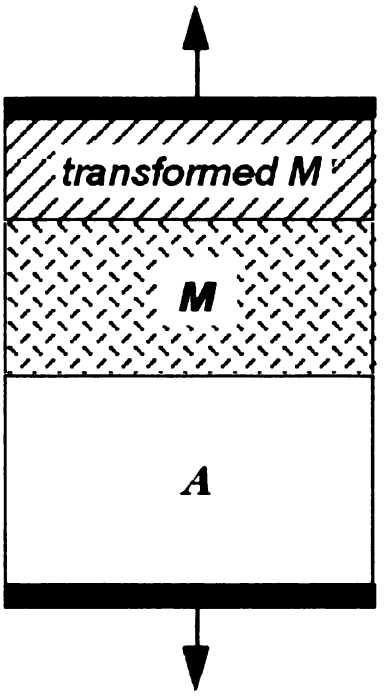

Figure 47. Series model for stress induced martensite in austenite phase. (after reference [*204*])

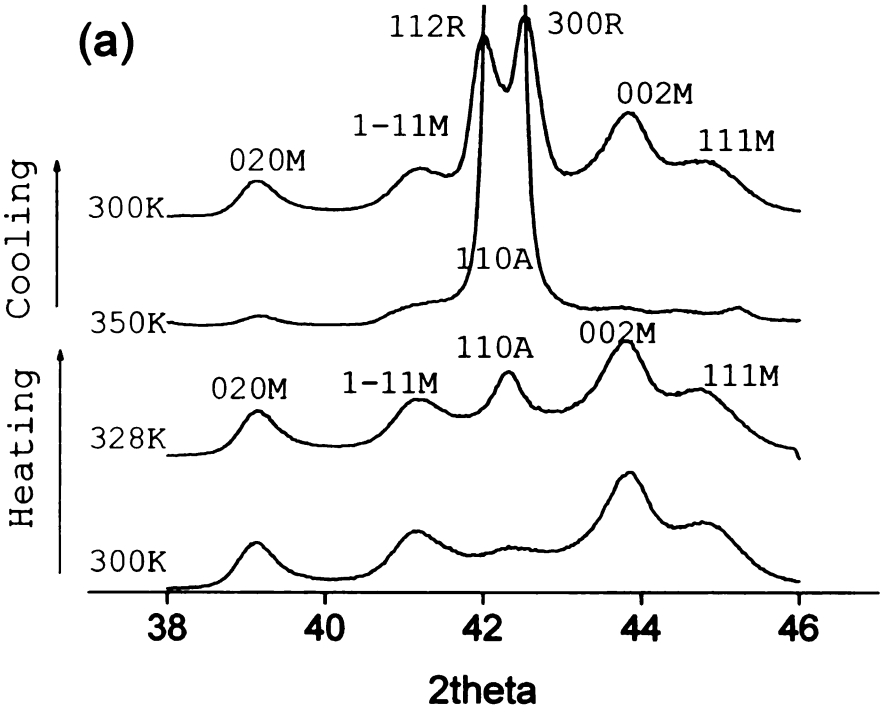

Figure 48. X ray diffraction patterns of NiTi thin films (sample #1) at various temperatures

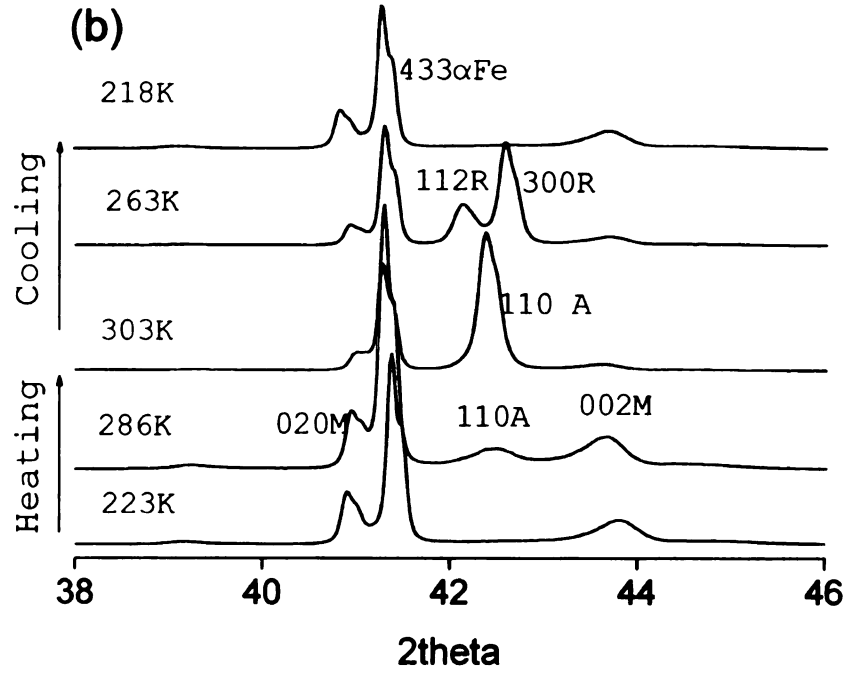

Figure 49. X ray diffraction patterns of NiTi thin films (sample #2) at various temperatures sample

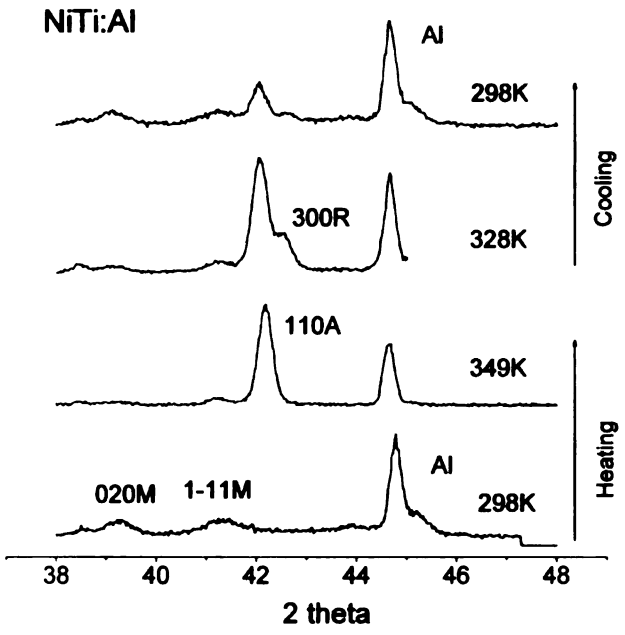

Figure 50. Temperature scanning X-ray diffraction of NiTi thin film on 6061T6 substrates, from which phase transformation temperatures were estimated and listed in TABLE. CrN coating was later deposited onto the NiTi thin films.

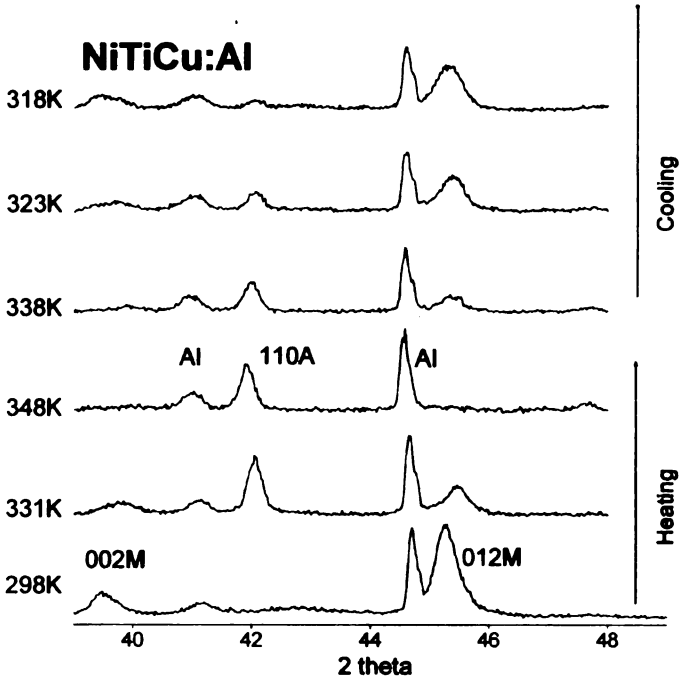

Figure 51. Temperature scanning X-ray diffraction of NiTiCu thin film on 6061T6 substrates. CrN coatings were later deposited on the NiTi thin films

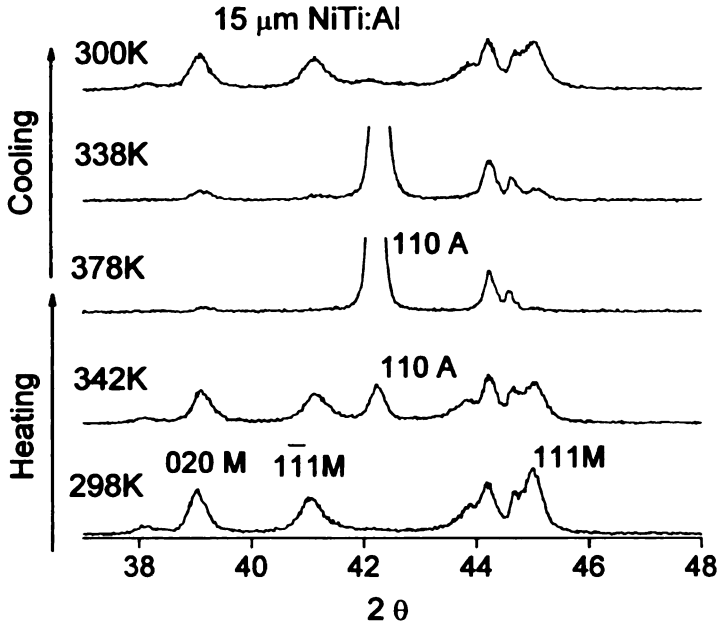

Figure 52. Temperature scanning X-ray diffraction of NiTi thin film on 6061 T6 aluminum substrates. The NiTi thin films were interlayers of DLC coatings

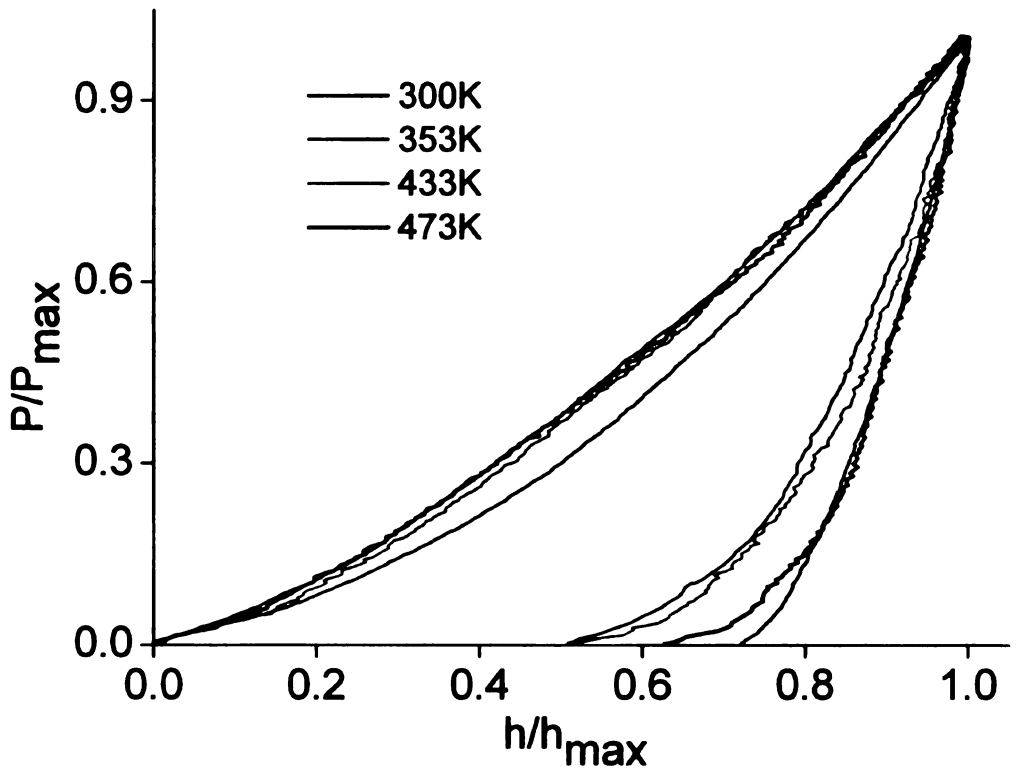

Figure 53. The normalized load-depth curves from Berkovich indentation of the NiTi thin films at different temperatures.

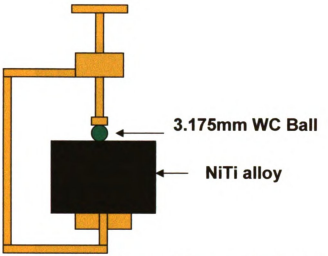

Figure 54. Diagram of thermomechanical training method to create two-way indent depth change.

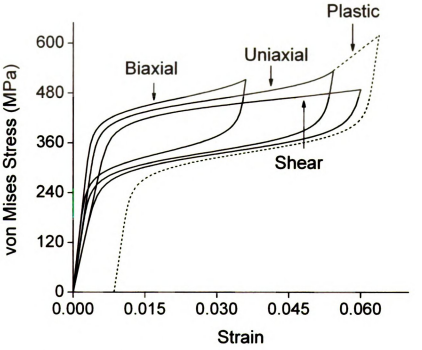

Figure 55. Stress-strain curves of simple loading conditions from the 3D constitutive model for superelastic effect with plasticity. For the biaxial loading curve, the strain rate is set the same in two loading directions. The dashed curve represents a high uniaxial load which causes plastic hardening and permanent plastic strain.

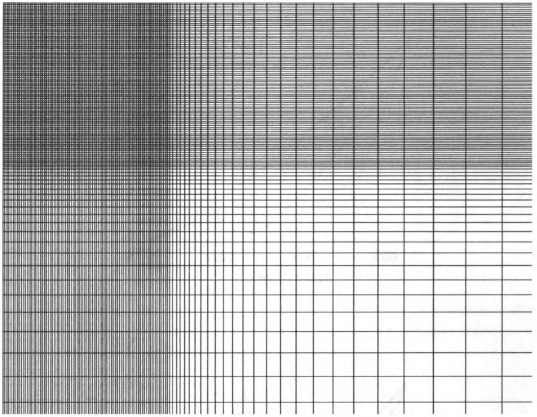

Figure 56. Finite element mesh of indentation model. The refined region is the contact region. Total node number is around 15000.

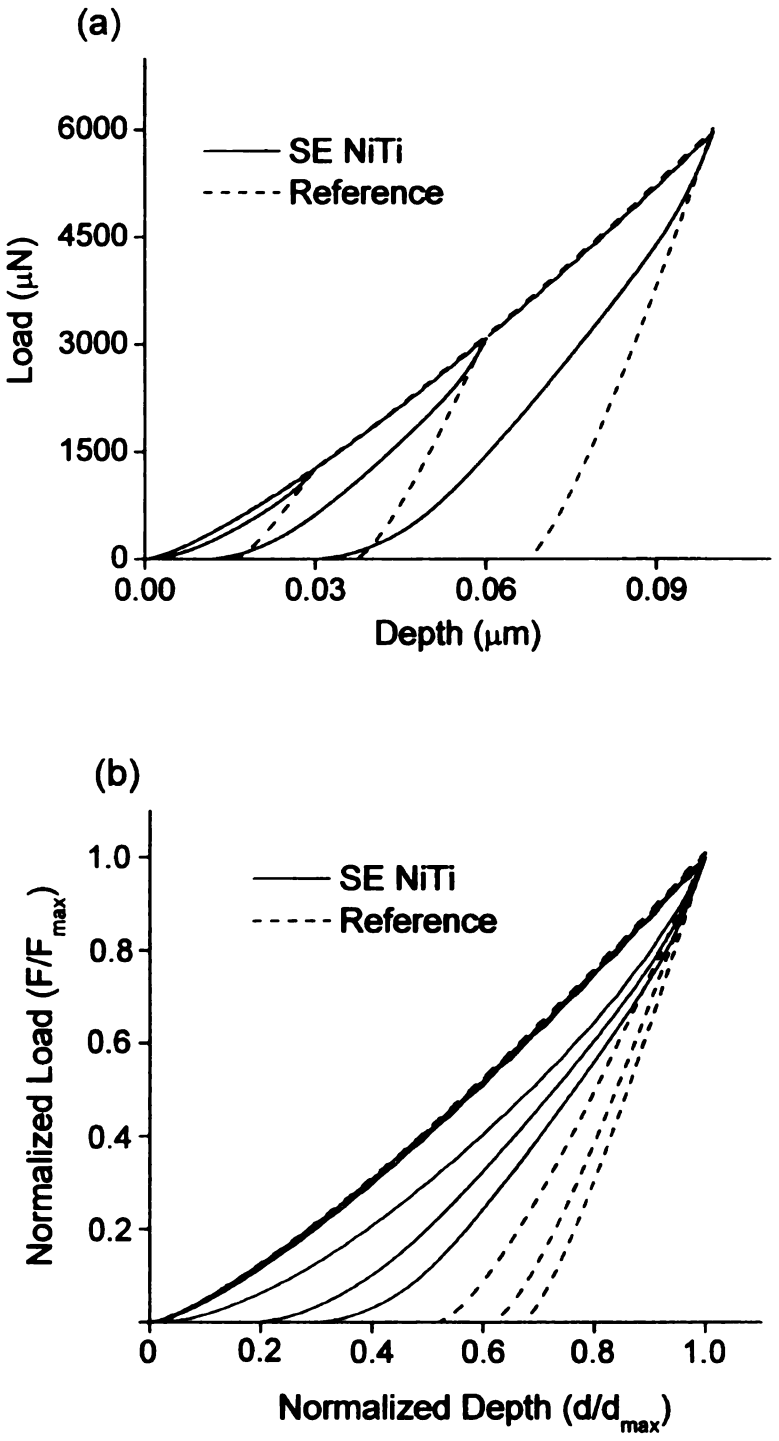

Figure 57. Absolute (a) and normalized (b) load-displacement curves of SE NiTi and reference materials from finite element modeling. Indentation-induced superelasticity enables large or 100% indent depth recovery.

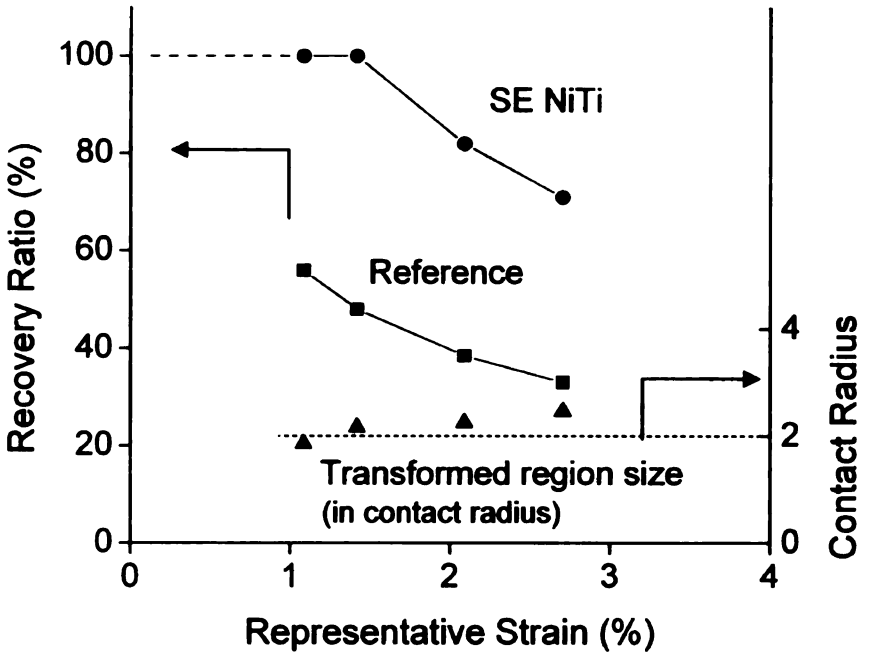

Figure 58. Recovery ratios vs. representative strains at different indentation depths, and the size of indentation-induced phase transformation region at different indentation depths, measured in contact radius.

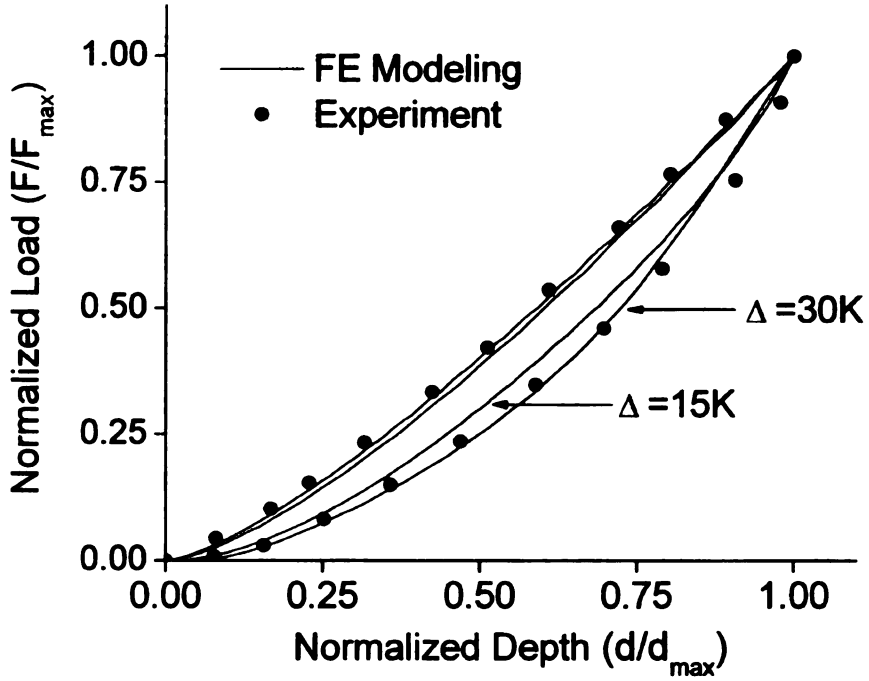

Figure 59. Comparison of experimental and calculated load-displacement curves. The experimental results are adapted from Ni *et al.*[6] Modeling SE NiTi has a phase transformation hysteresis Δ (Δ= $(A_f - A_s)/2-(M_s - M_f)/2$) 15K and 30K for the two computed curves.

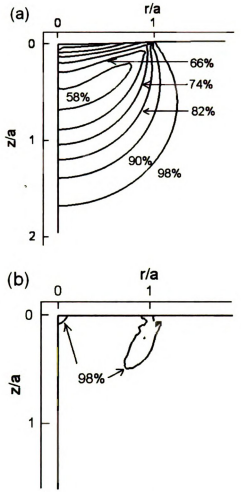

Figure 60. Contours of the austenite phase volume fraction at indentation depth of 0.018μm (a), and complete indent recovery after unloading (b), where few residual martensites are present after unloading.

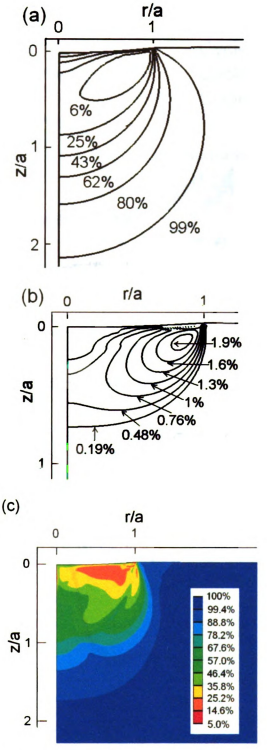

Figure 61. Contours of the austenite phase volume fraction (a) and plastic strains (b) at indentation depth of 0.10μm. (c) Contours of the austenite volume fraction after unloading. For the partially recovered indent (recovery ratio 71%), there were much more residual martensites than in FIG. 5(b).

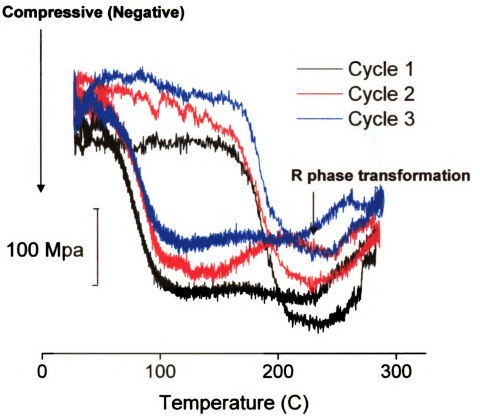

Figure 62. Residual stress evolution of NiTi thin film on Al substrates with temperature, for three heating-cooling cycles.

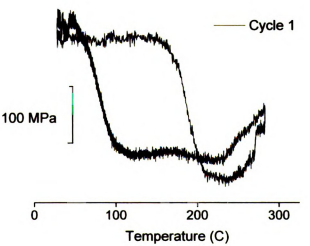

Figure 63. First cycle residual stress evolution of NiTi thin film on Al substrates with temperature.

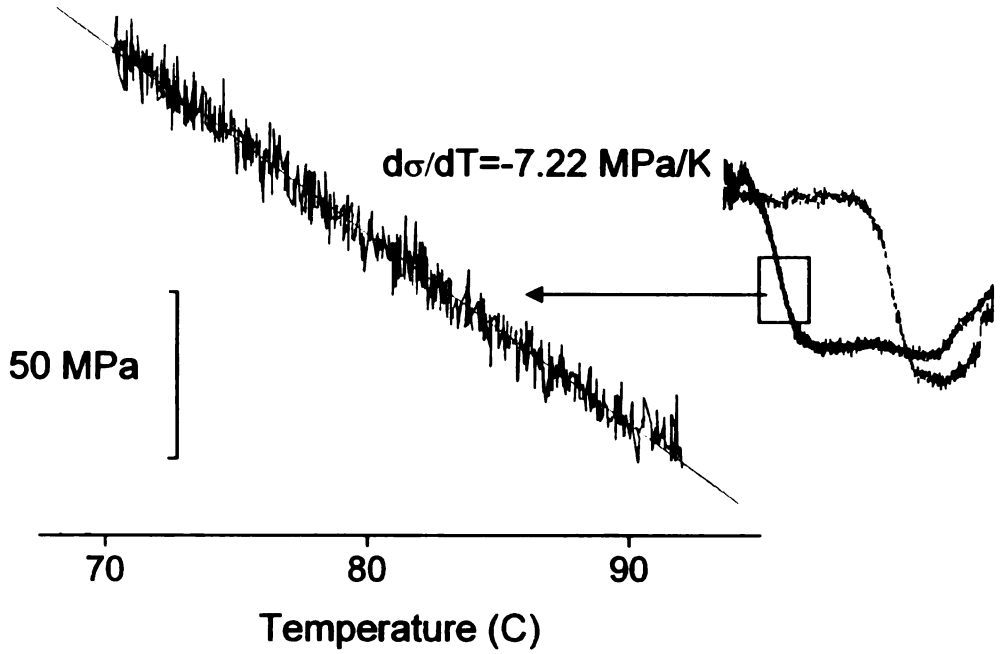

Figure 64. The stress/temperature rate of NiTi thin film on Al substrates during martensite phase transformation.

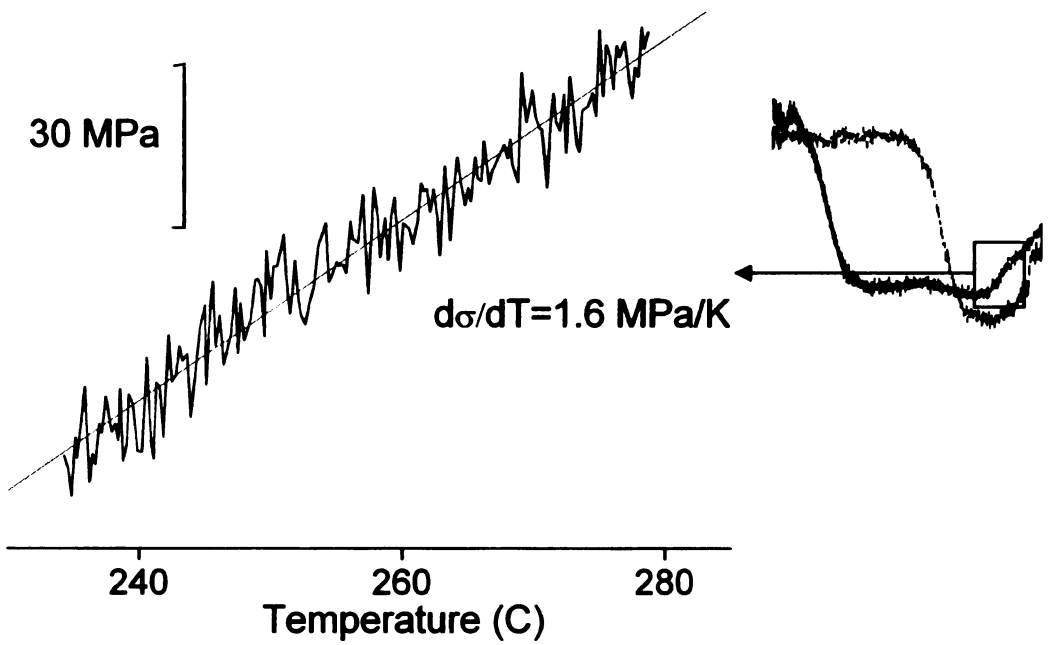

Figure 65. The stress/temperature rate of NiTi thin film on Al substrates from CTE mismatch between thin film and substrates, without the influence of phase transformation,

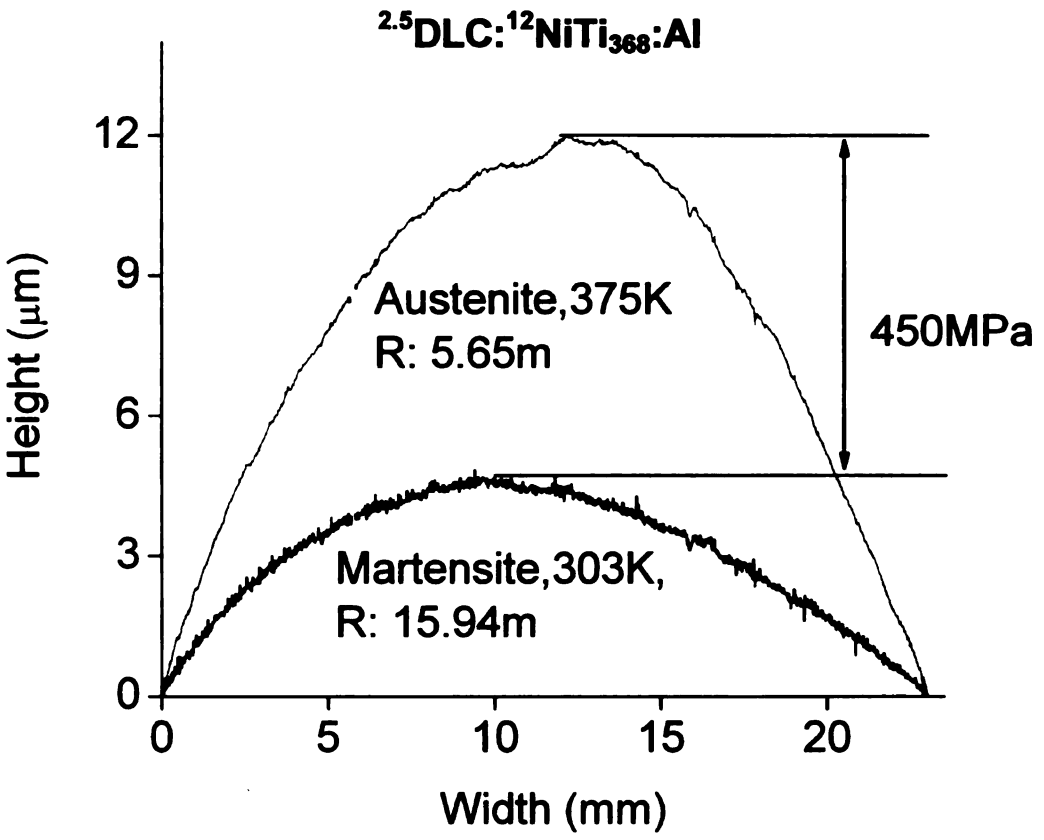

Figure 66. Curvature change of $^{2.5}$DLC:^{12}NiTi$_{368}$:Al sample between room temperature around M_f and elevated temperature above A_f. The curvature change mainly resulted from residual stress change in NiTi interlayer.

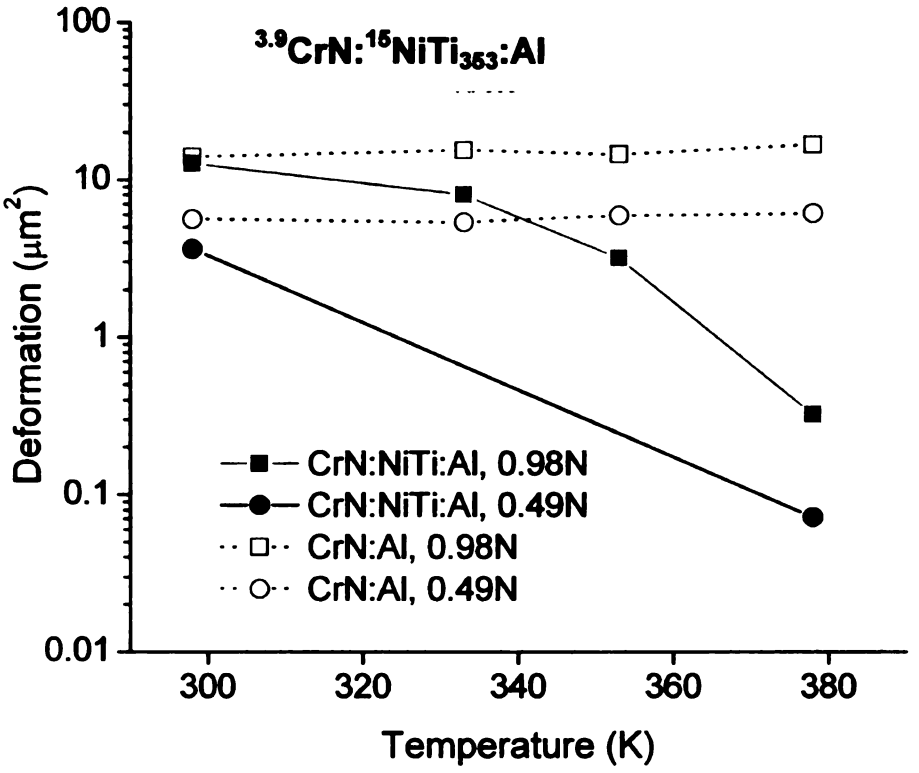

Figure 67. Temperature scanning wear deformation of CrN:NiTi:Al and CrN:Al samples, under 0.49 and 0.98 N load, using a 200 μm tip radius spherical indenter. Superelastic NiTi improves the wear resistance by limiting plastic deformation to the soft aluminum substrates.

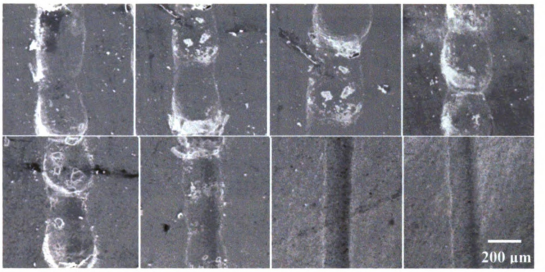

Figure 68. SEM images of temperature wear tracks of $^{3.9}$CrN:Al samples (top row) and $^{3.9}$CrN:^{15}NiTi$_{353}$:Al sample (bottom row), under 0.98N load. The wear data was presented in Figure 67

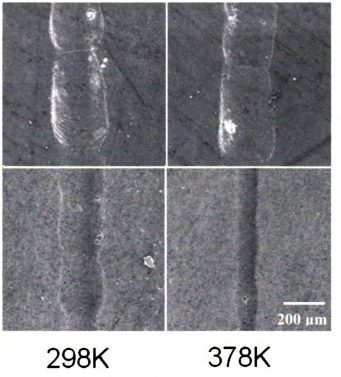

Figure 69. SEM images of temperature scanning wear tracks of $^{3.9}$CrN:Al samples (first row) and $^{3.9}$CrN:^{15}NiTi$_{353}$:Al sample (second row), under 0.49N. The wear data was presented in Figure 67.

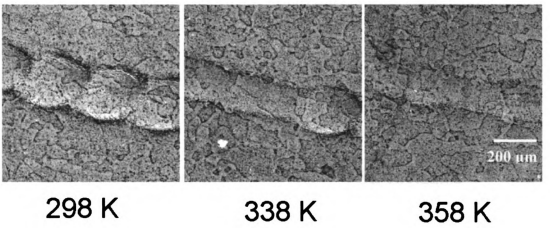

Figure 70. SEM images of temperature scanning wear tracks of $^{1.7}$CrN:^{9}NiTiCu$_{343}$:Al samples. The wear data was presented in Figure 71.

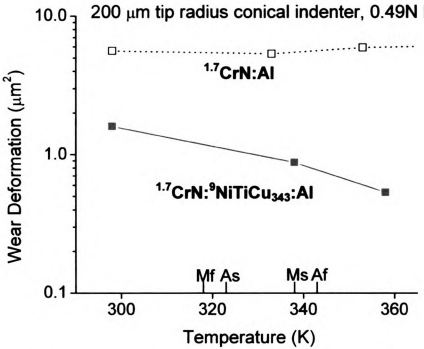

Figure 71. Temperature scanning wear deformation of $^{1.7}$CrN:^{9}NiTiCu$_{343}$:Al and $^{1.7}$CrN:Al samples, under 0.49 and 0.98 N load.

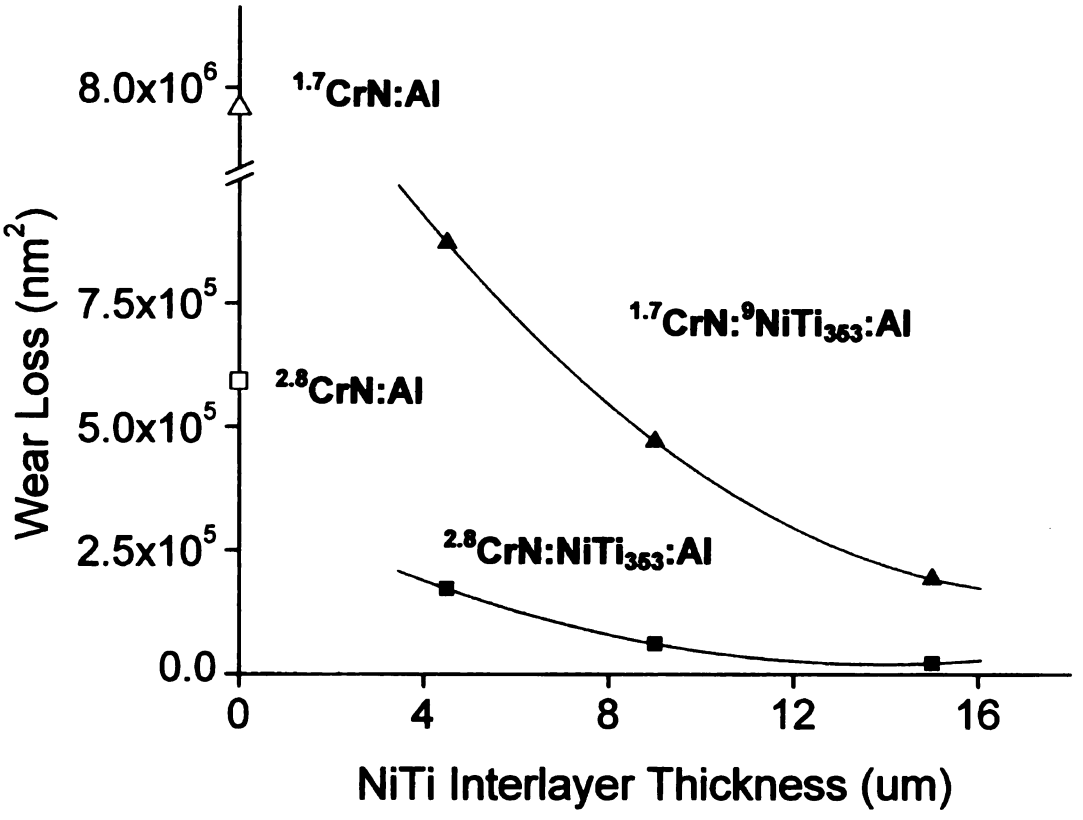

Figure 72. The effect of interlayer and CrN coating thickness on wear resistance at room temperature. The wear test was done using 6.35mm diameter WC under 5N load. Thicker coating and interlayer gave better wear resistance.

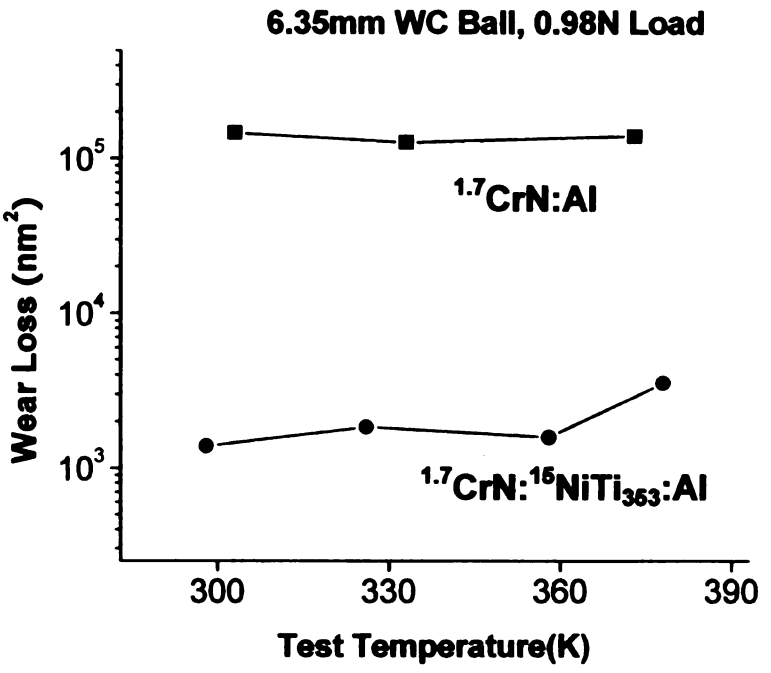

Figure 73. Wear loss vs. temperature using a different loading condition (6.35mm ball, 0.98N load). Wear resistance was not improved at temperature above

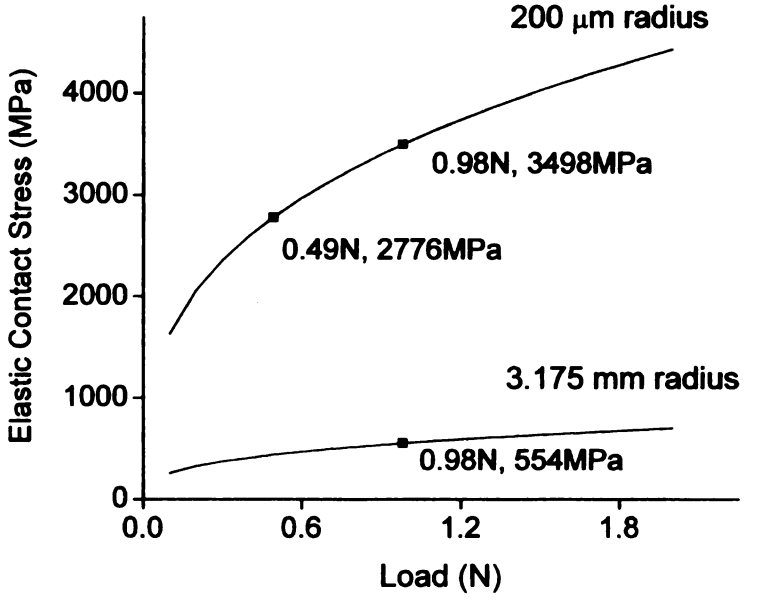

Figure 74. Elastic contact stress in elastic halfspace from 3.175mm radius and 200um radius sphere under different loads.

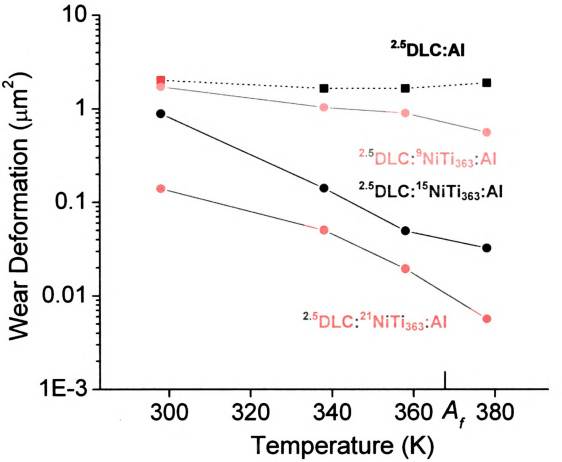

Figure 75. Temperature scanning wear tests of $^{2.5}$DLC:NiTi$_{363}$:Al samples, using 200um tip radius diamond indenter under 0.49N load. Thick NiTi interlayer and SE NiTi interlayer at temperature above A_f showed better wear.

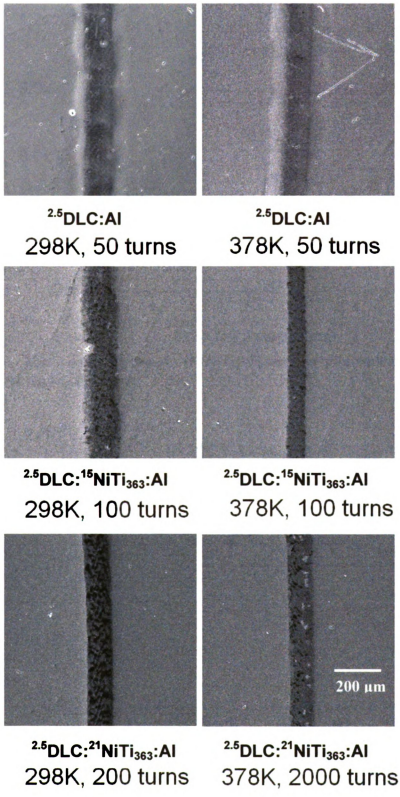

Figure 76. SEM images of temperature scanning wear tracks of $^{2.5}$DLC:NiTi$_{363}$:Al and $^{2.5}$DLC:Al samples. The wear data was presented in Figure 88.

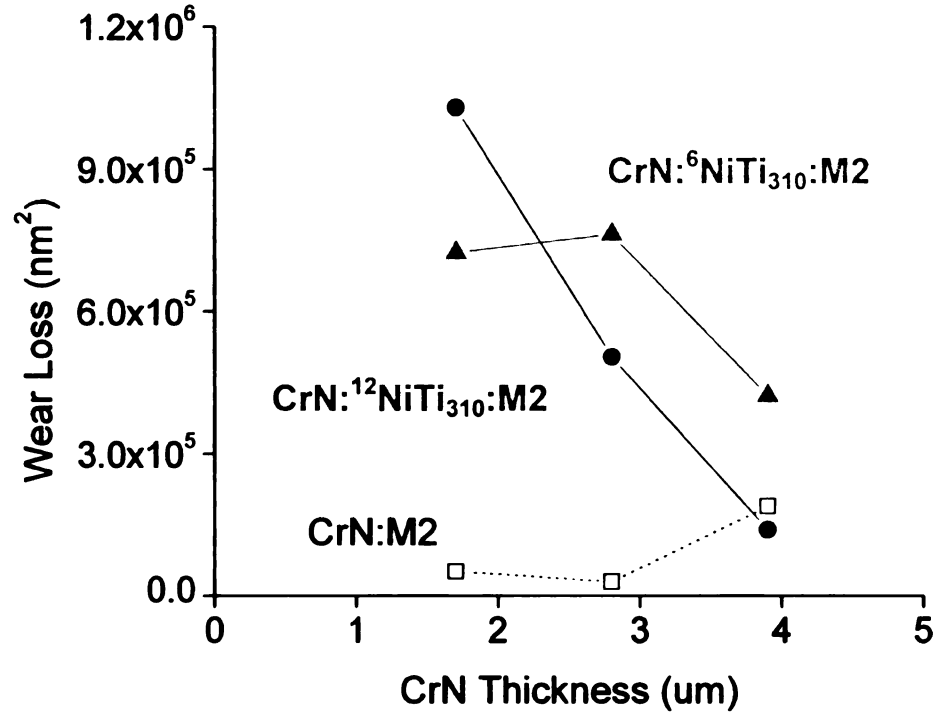

Figure 77. The wear resistance of CrN:NiTi:M2 samples at room temperature as a function of CrN coating thickness.

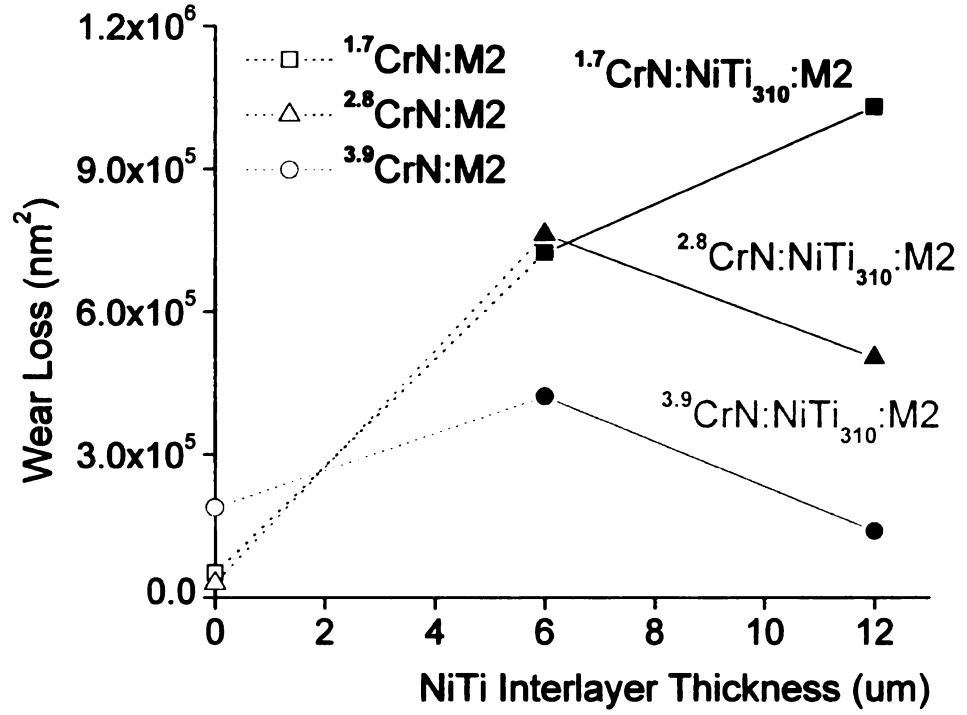

Figure 78. The wear resistance of CrN:NiTi:M2 samples at room temperature as a function of interlayer thickness.

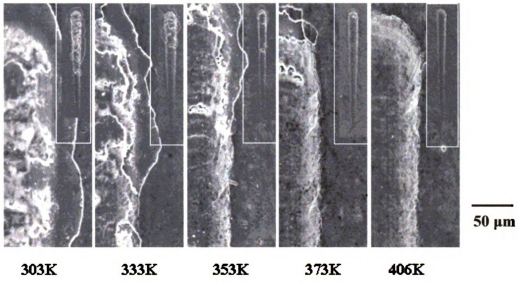

Figure 79. SEM images of temperature scanning scratch tracks on $^{3.9}$CrN:^{9}NiTi$_{353}$:Al. Images of the whole scratch tracks (1 mm in length)are placed at the upper right corner.

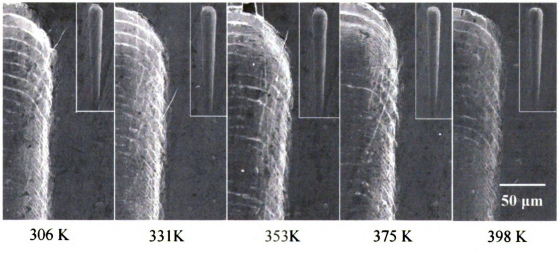

Figure 80. SEM images of temperature scanning scratches tracks on $^{3.9}$CrN:Al. Images of the whole scratch tracks (1 mm in length)are placed at the upper right corner.

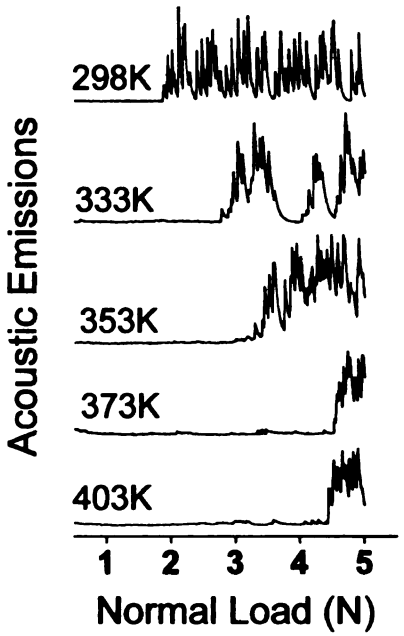

Figure 81. Acoustic emission of scratch tests on $^{3.9}$CrN:^{9}NiTi$_{353}$:Al. It showed strong temperature dependence that matched phase transformation temperatures of NiTi interlayers

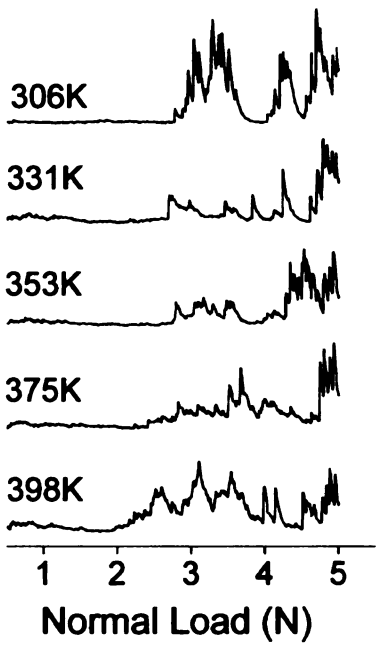

Figure 82. Acoustic emission of scratch tests on $^{3.9}$CrN:Al. There is no significant temperature dependence.

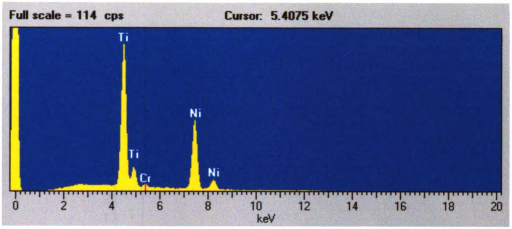

Figure 83. EDS spectrum of the delaminated area in scratch tracks on $^{3.9}$CrN:^{9}NiTi$_{353}$:Al, showing that delamination occurred at the interface between CrN and NiTi interlayer.

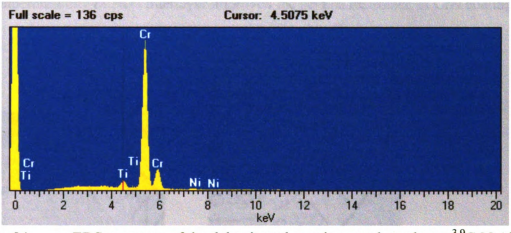

Figure 84. EDS spectrum of the delaminated area in scratch tracks on $^{3.9}$CrN:Al, showing the delamination occurred at the interface between CrN and the Cr interlayer. The Cr interlayer (<μm) was deposited before CrN as a precursor layer. It is an indispensable process of making CrN.

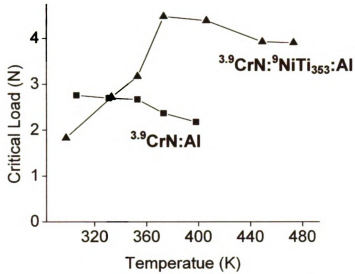

Figure 85. Critical load of CrN coating in scratch tests as a function of temperature. The superelasticity of NiTi interlayer improved the scratch resistance of CrN coating.

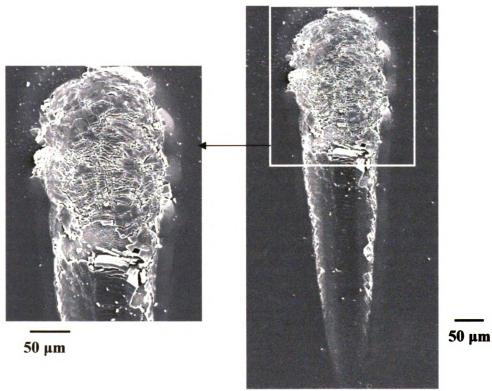

Figure 86. SEM images of scratch track on $^{2.5}$DLC:Al sample, showing severe DLC coating failure and delamination. 7N progressive load was used.

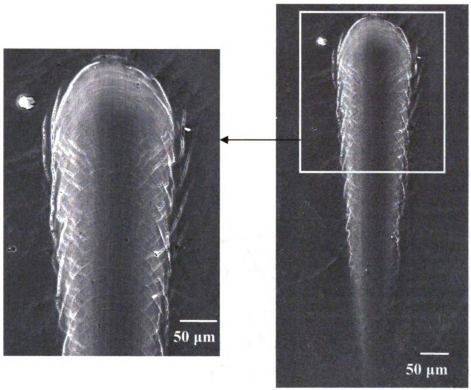

Figure 87. SEM images of scratch track on $^{2.5}$DLC:^{15}NiTi$_{368}$:Al sample, showing much less coating failure compared to the previous figure without NiTi interlayer. 7N progressive load.

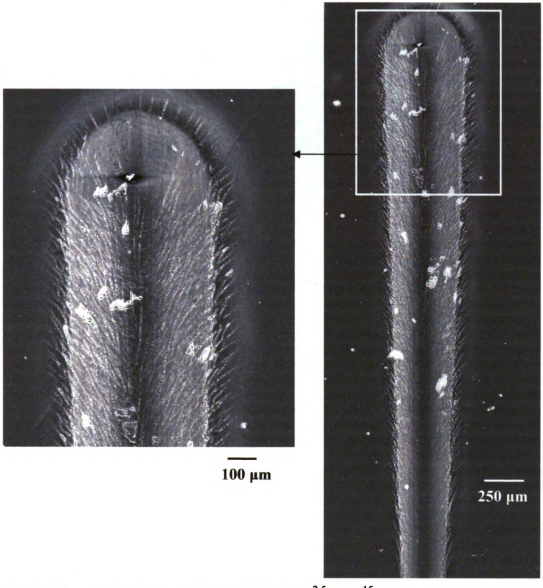

Figure 88. SEM images of scratch track on $^{2.5}$DLC:^{15}NiTi$_{368}$:Al sample, under high 30N progressive load. Although there was coating failure, no dramatic delamination occurred, proving the strong interface between DLC coating and NiTi interlayer.

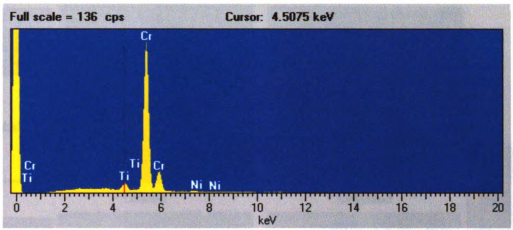

Figure 89. EDS of delaminated region in scratch tracks on $^{2.5}$DLC:^{15}NiTi$_{368}$:Al sample, shows the delamination occurred at DLC and (Cr)NiTi interface. The extra Cr layer on NiTi is represented by the high Cr peak here, compared to the weak Cr peak in Figure 83.

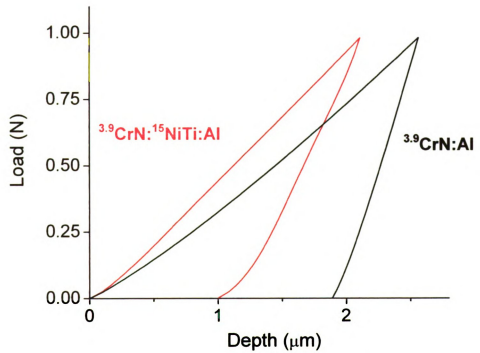

Figure 90. Computational load-displacement curves from finite element modeling of spherical indentation on $^{3.9}$CrN:^{15}NiTi:Al and $^{3.9}$CrN:Al, using 200 μm tip radius spherical diamond indenter.

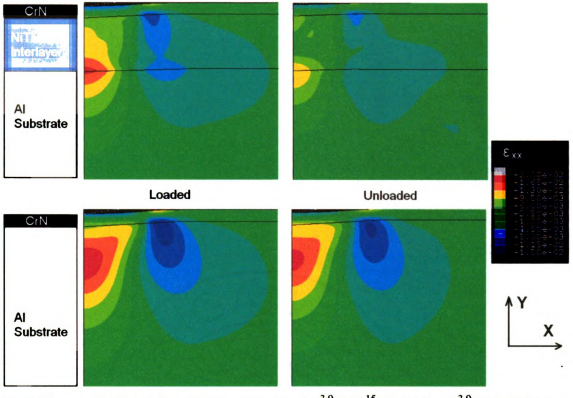

Figure 91. Horizontal strain component ε_{xx} in $^{3.9}$CrN:^{15}NiTi:Al and $^{3.9}$CrN:Al from FEA

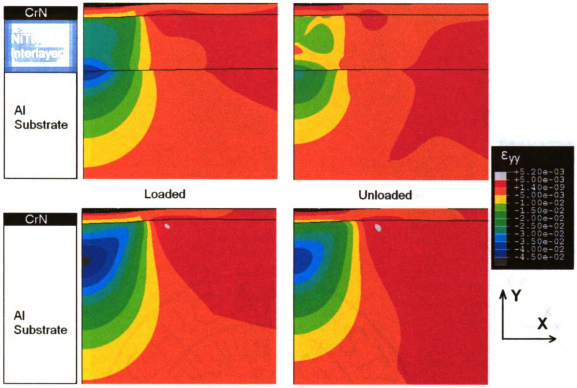

Figure 92. Vertical strain component ε_{yy} in $^{3.9}$CrN:^{15}NiTi:Al and $^{3.9}$CrN:Al from FEA

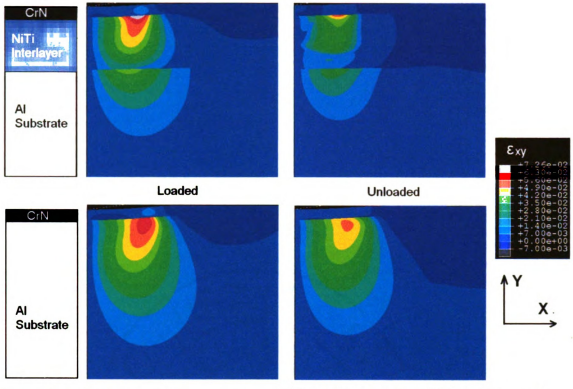

Figure 93. Shear strain component ε_{xy} in $^{3.9}$CrN:^{15}NiTi:Al and $^{3.9}$CrN:Al from FEA

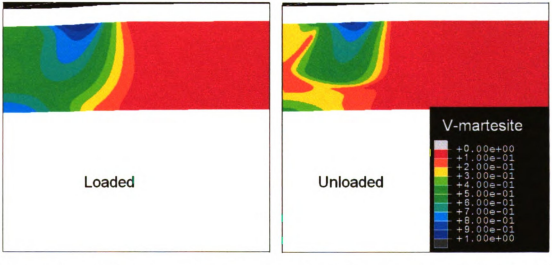

Figure 94. Martensite volume fraction in NiTi interlayer from FEA. The blank region represent the coating and substrate because there is no martensitic phase.

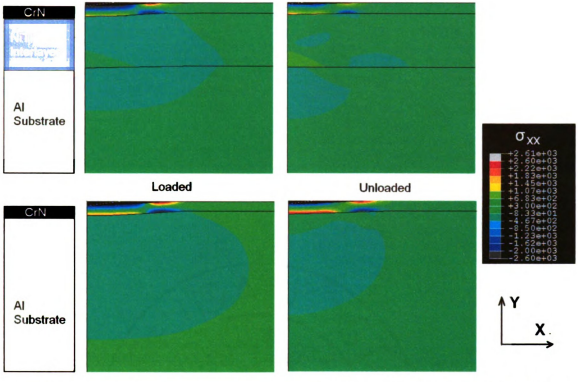

Figure 95. Horizontal stress component σ_{xx} in $^{3.9}$CrN:^{15}NiTi:Al and $^{3.9}$CrN:Al from FEA

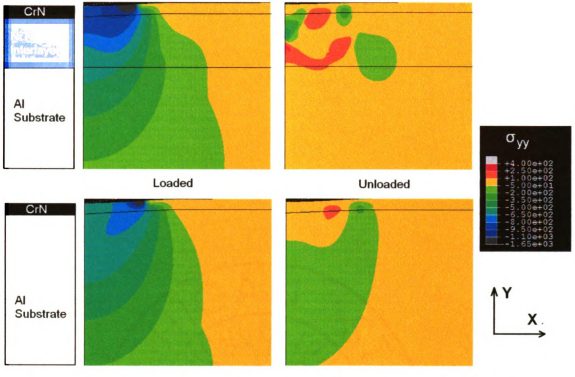

Figure 96. Vertical stress component σ_{yy} in $^{3.9}$CrN:^{15}NiTi:Al and $^{3.9}$CrN:Al from FEA

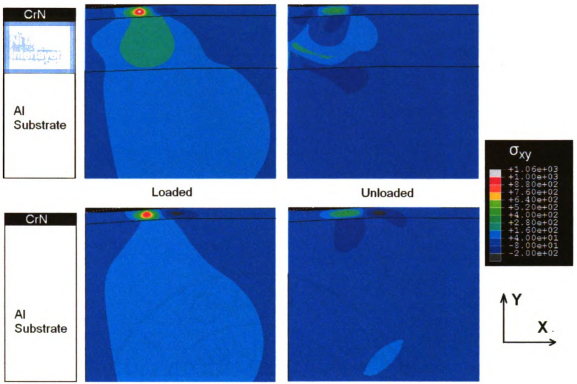

Figure 97. Shear stress component σ_{xy} in CrN:NiTi:Al and CrN:Al from FEA

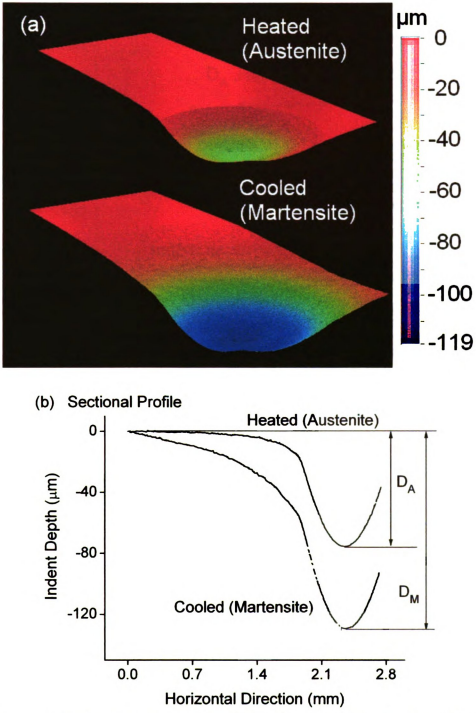

Figure 98. (a) 3D profile of a heated and cooled indent, (b) Sectional profile of the heated and cooled indent.

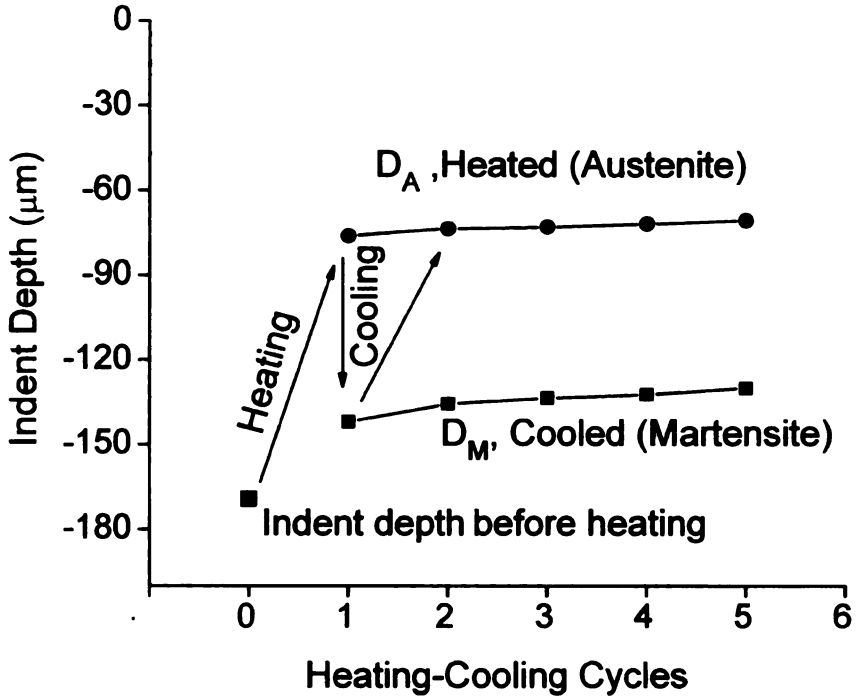

Figure 99. Two-way indent depth change over several thermal cycles.

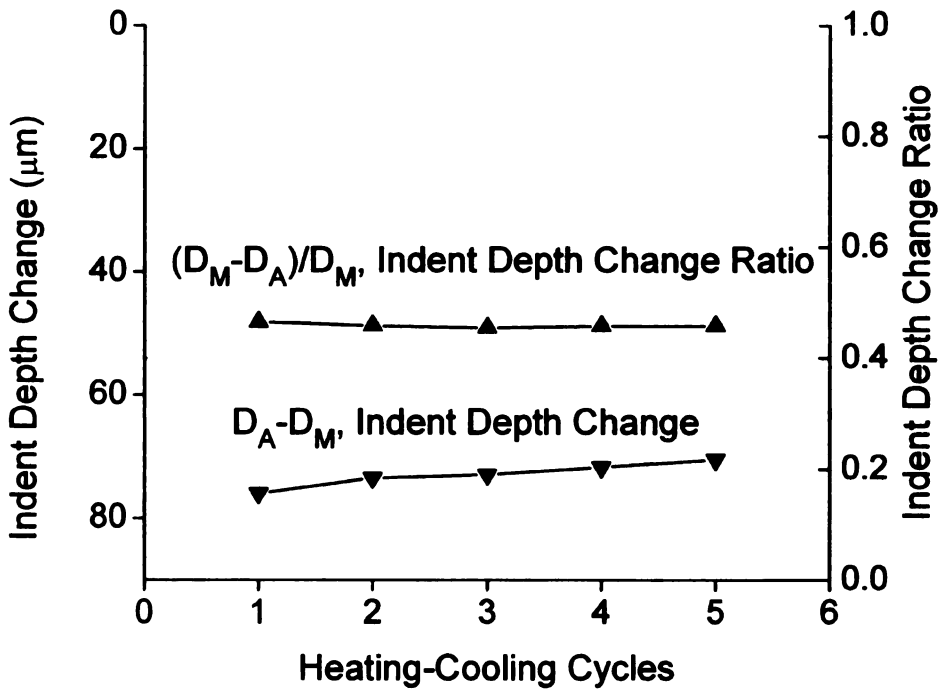

Figure 100. Indent depth change ratio and absolute indent depth change.

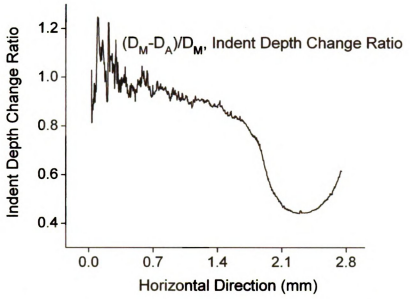

Figure 101. Indent depth change ratio $(D_M-D_A)/D_M$ vs. horizontal direction, referred to center. The center of indent had smallest ratio of depth change. Further away from the indent, both D_M and D_A become small and dominant by the surface roughness, causing the fluctuation in the ratio. Ideally the $(D_M-D_A)/D_M$ should approach zero for surfaces far away from indents because (D_M-D_A) should equal zero. But D_M-D_A is not zero because: 1) small surface roughness change in NiTi between martensitic and austenitic phase, 2) measurement error between two measurements.

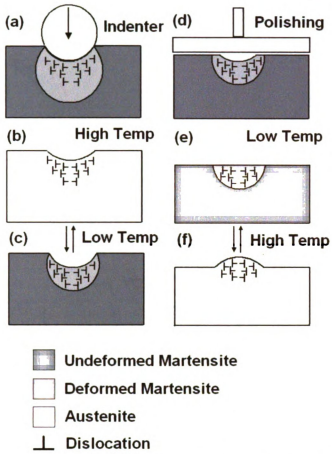

Figure 102. Schematic diagrams of experimental procedures and mechanisms for achieving RSP. (a), indentation is accommodated by the deformed martensite and slip-plasticity. (b), When heated to the austenite phase, the indent is partially recovered. (c), when cooled down to martensite phase, the residual indent became deeper. The indent depth change is reversible with heating and cooling temperatures (Figure 2). The dislocation structure and its associated stress field can facilitate the growth of oriented martensite variants during austenite-to-martensite transformation, leading to two-way indent depth change. (d), The residual indents are removed by polishing. (e), The oriented martensite region and dislocations can still exist after the indent is removed. (f), A reversible surface protrusion is formed upon heating.

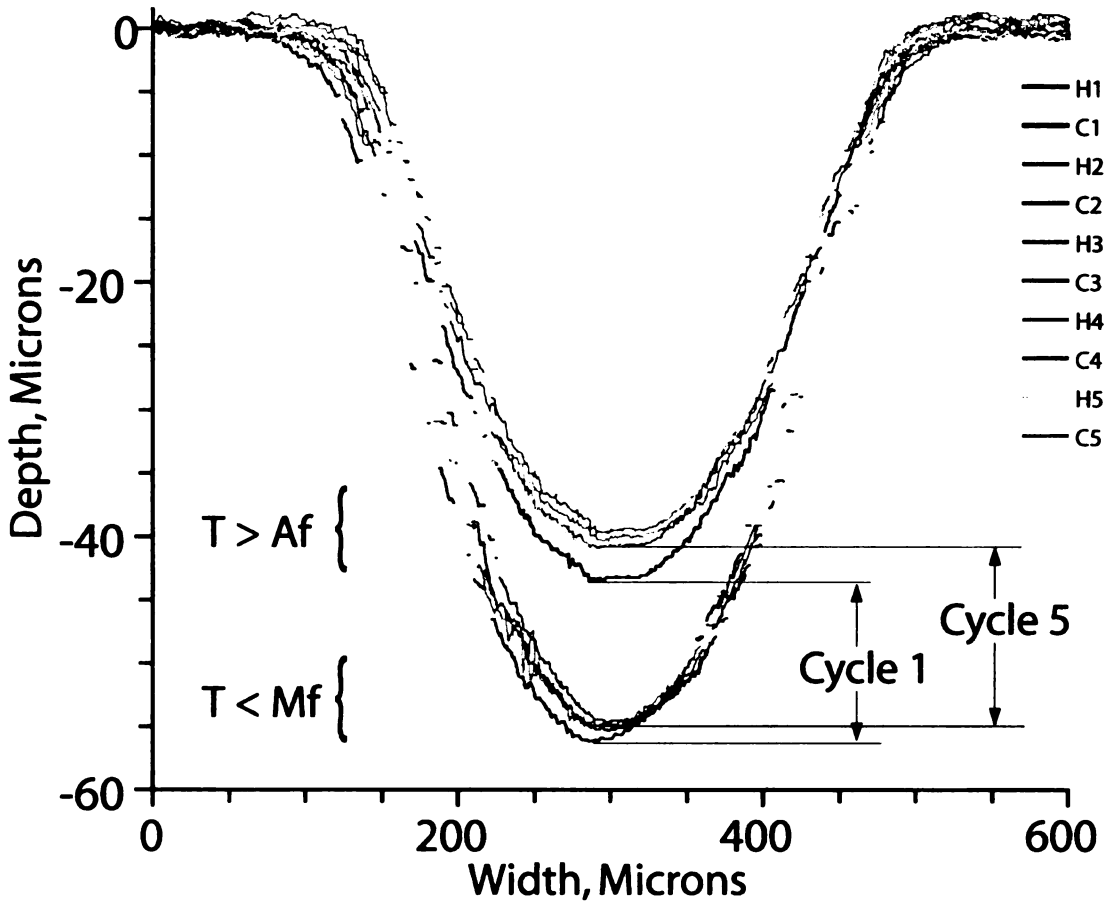

Figure 103. Reversible indent depth change. A spherical indent made with a steel ball pressed relatively deeply into a martensitic sample of NiTi not only recovers a substantial percentage of the indent depth when heated above the A_f temperature, but also subsequently displays cyclic displacement behavior as the temperature is cycled from below M_f to above A_f.

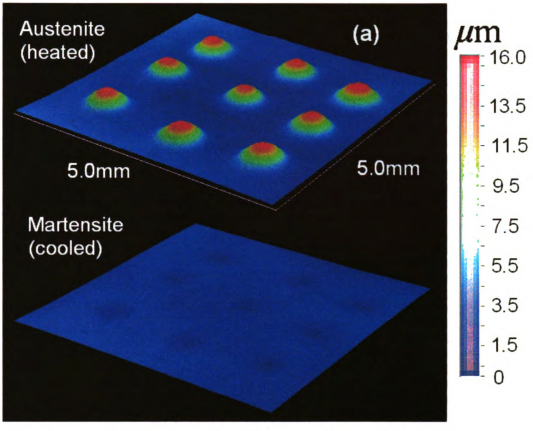

Figure 104. Thermally-reversible surface protrusions. A 3x3 matrix of thermally-reversible protrusions produced in a $Ni_{50.3}Ti_{49.7}$ alloy by first creating deep spherical indentations and then planarizing the specimen while it was still in the martensitic condition. The protrusions appear and disappear as the specimen is heated from below M_f to above the A_f temperature.

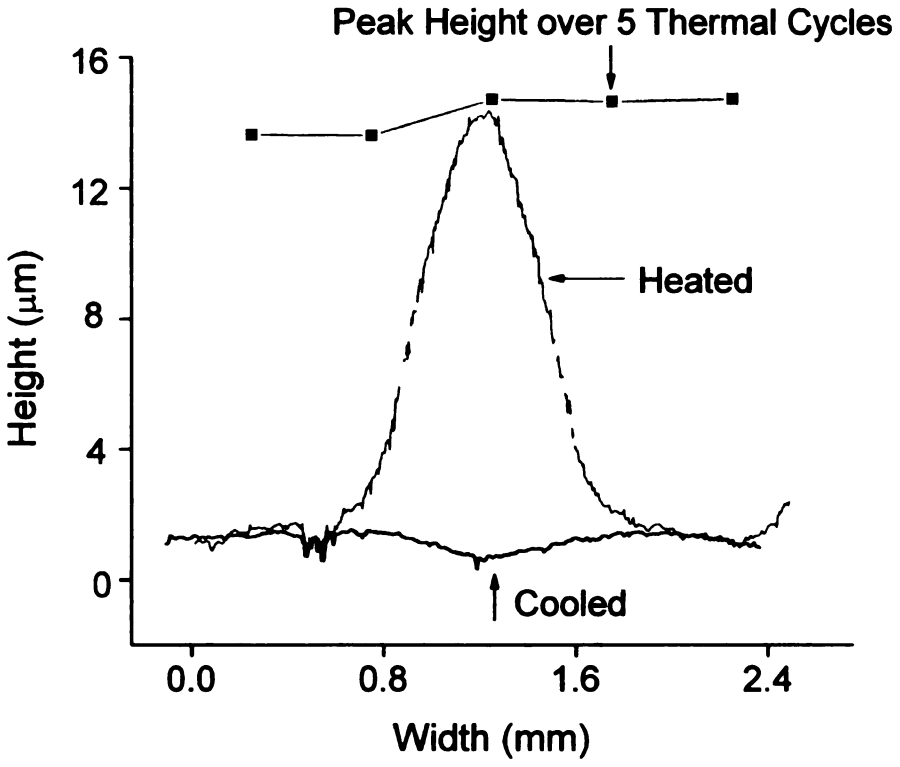

Figure 105. Sectional profiles of reversible circular surface protrusions and peak height over five thermal cycles.

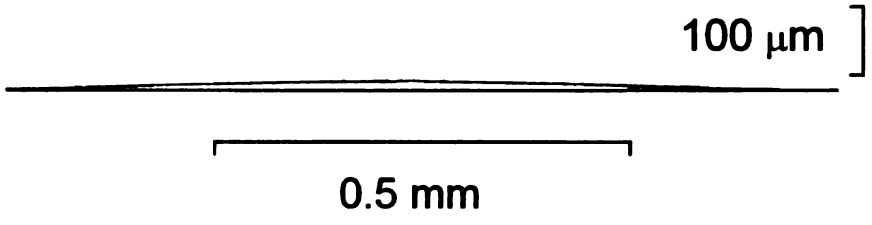

Figure 106. Actual shape of the circular surface protrusion

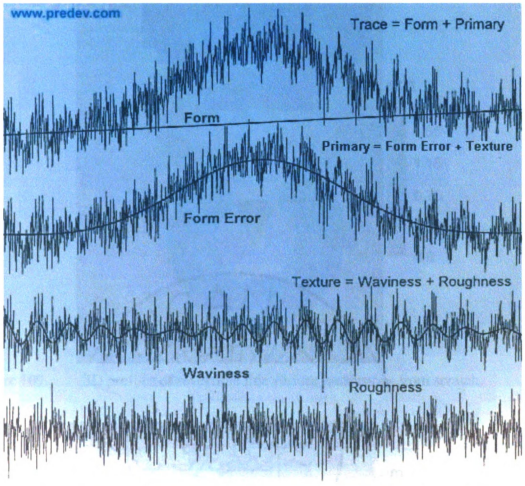

Figure 107. Schematic of different kind of surface fluctuations. Image from http://www.predev.com/smg/intro.htm. More detail in reference [246].

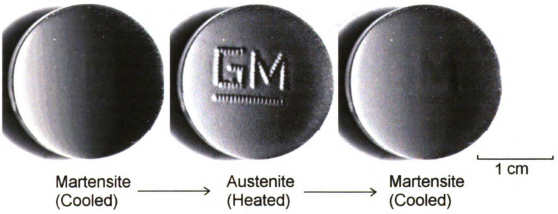

Figure 108. Reversible GM logo made from adjoining reversible surface protrusions. Imaged in normal bright field optical microscopy.

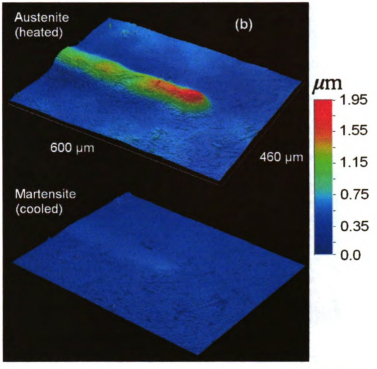

Figure 109. 3D profiles of reversible line surface protrusions from scratch.

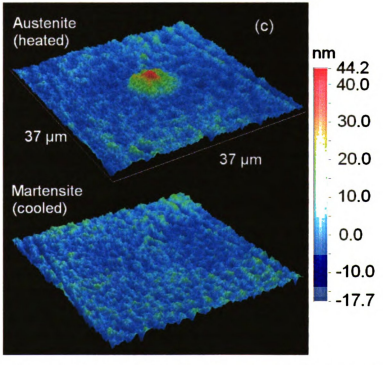

Figure 110. 3D profiles of nanoscale circular surface protrusions on NiTi thin film/Silicon substrate.

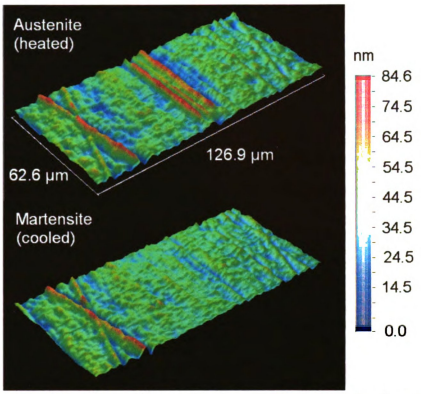

Figure 111. 3D profiles of reversible nano scale line protrusion on NiTi thin film/Silicon substrate

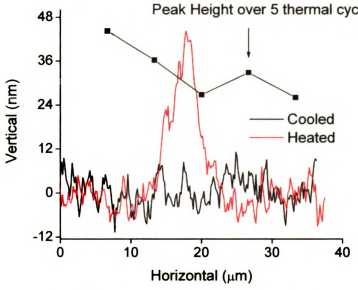

Figure 112. Sectional profiles of the nano circular surface protrusions and peak height over five thermal cycles.

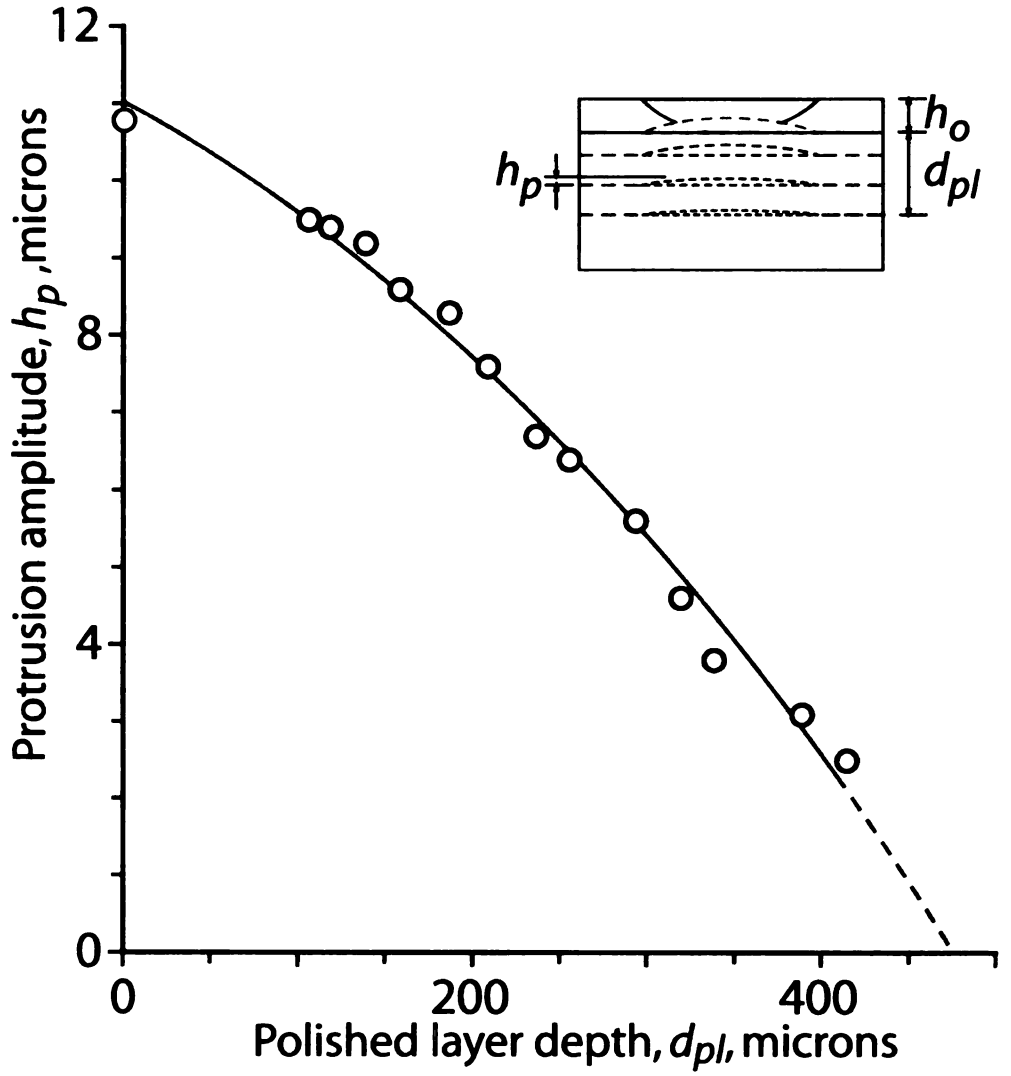

Figure 113. Decay of protrusion amplitude with surface-removal. When successive surface layers of thickness d_{pl} are removed after initial planarization to a depth h_o, the amplitude of protrusion appearance and disappearance, h_p, diminishes and approaches zero when material has been removed to a depth roughly equal to the radius of the initial indent contact.

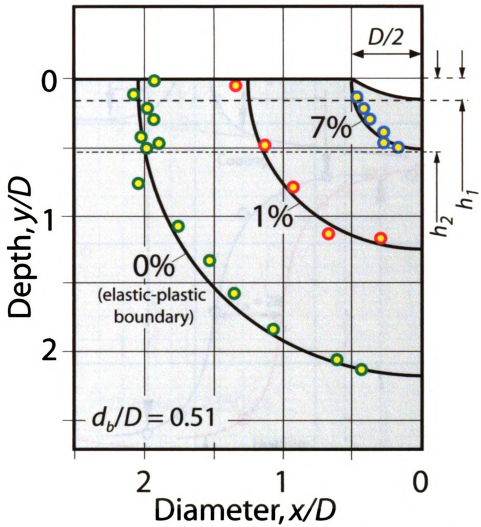

Figure 114. Plastic strain distribution under an indent. Theoretical and experimental results , adapted from Samuel and Mulhearn [232] showing the expected magnitude of plastic strain under an indent in a ductile metal.

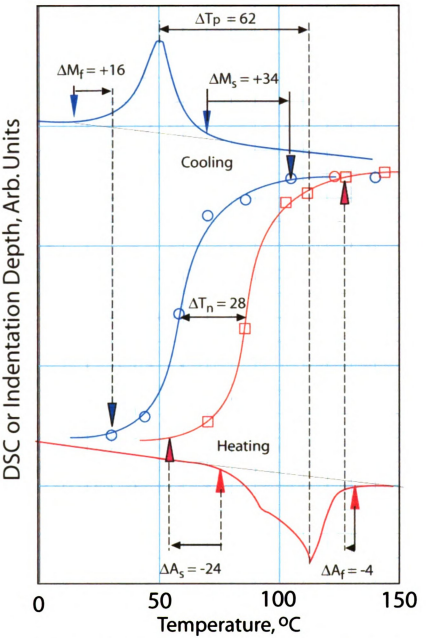

Figure 115. Height of reversible circular protrusions vs. temperature. The phase transformation temperature of NiTi sample is also marked. The hysteresis of the reversible protrusion is much narrower.

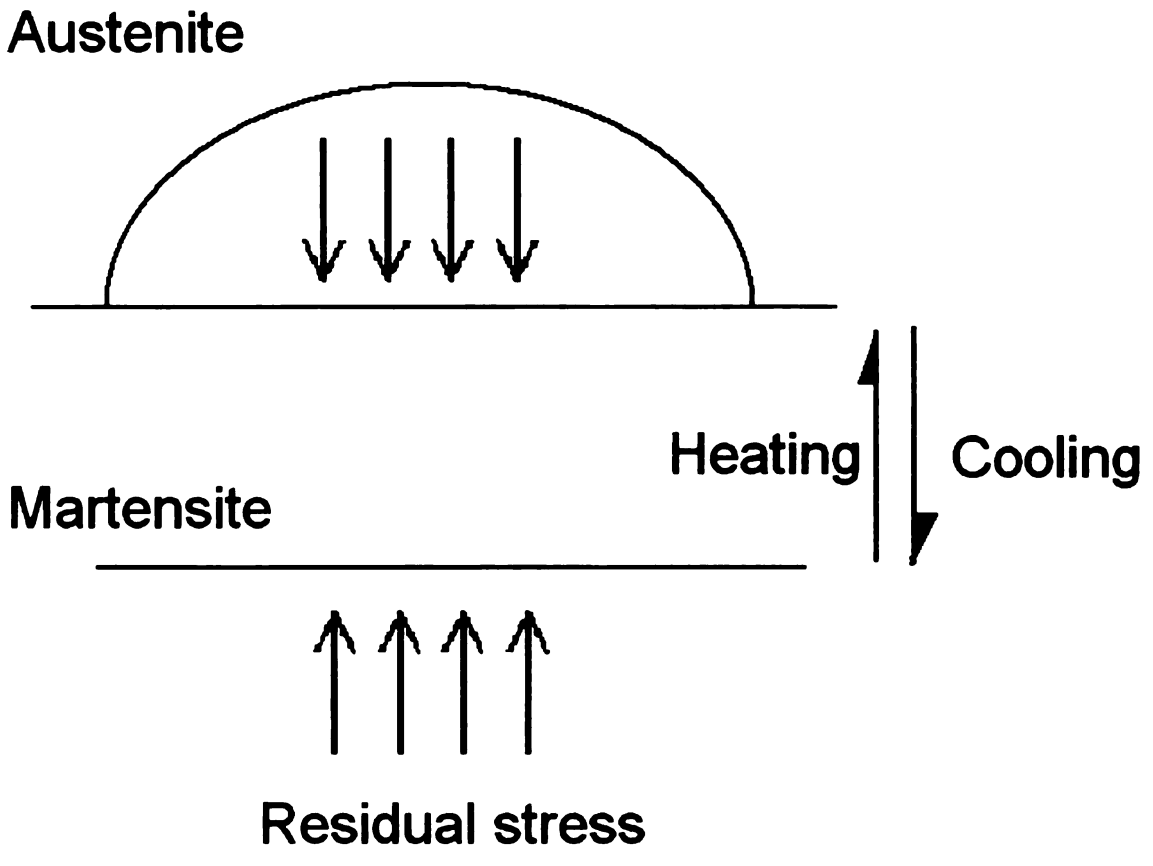

Figure 116. Schematic of Residual Stress in Reversible Surface Protrusion. The residual stress is in the opposite direction of TWSME during heating from martensite to austenite phase, and not in the opposite direction during cooling, narrowing hysteresis. The residual stress also stabilizes the TWSME.

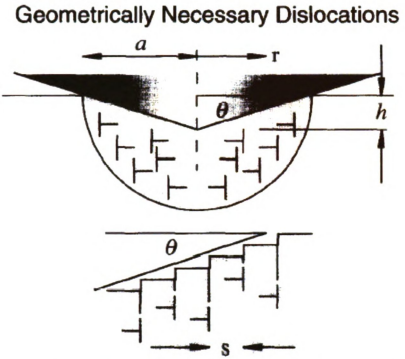

Figure 117. Geometrically necessary dislocations. It is assumed that the indentation is accommodated by circular loops of geometrically necessary dislocations with Burgers vectors normal to the plane of the surface. As the indenter is forced into the surface of a single crystal, geometrically necessary dislocations are required to account for the permanent shape change at the surface.

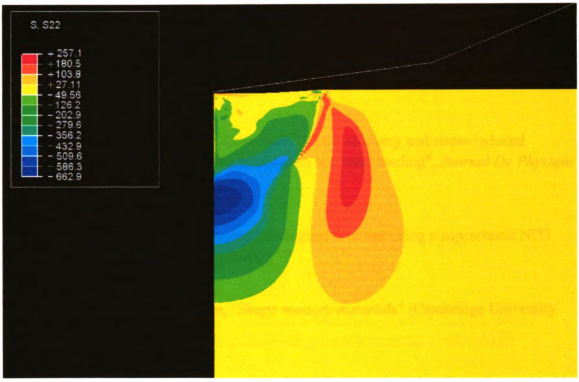

Figure 118. Residual stress in y direction (σ_{yy}) after spherical indentation in austenitic NiTi alloy, by finite element analysis. The negative sign is compressive direction.

References

1. W. Y. Ni *et al.*, "Effects of the ratio of hardness to Young's modulus on the friction and wear behavior of bilayer coatings", *Applied Physics Letters* **85**, 18, 4028 (2004).

2. W. Ni, Y. T. Cheng, D. S. Grummon, "Shape recovery and stress-induced martensite in TiNi following indentation and wear loading", *Journal De Physique Iv* **112**, 1147 (2003).

3. W. Y. Ni *et al.*, "Novel layered tribological coatings using a superelastic NiTi interlayer", *Wear* **259**, 842 (2005).

4. K. Otsuka, C. M. Wayman, *"Shape memory materials"* (Cambridge University Press, New York, 1998)

5. A. Olander, "The crystal structure of AuCd", *Zeitschrift Fur Kristallographie* **83**, 1/2, 145 (1932).

6. A. B. Greninger, V. G. Mooradian, "Strain transformation in metastable beta copper-zinc and beta copper-tin alloys", *Transactions Of The American Institute Of Mining And Metallurgical Engineers* **128**, 337 (1938).

7. G. V. Kurdyumov, L. G. Khandros, "O Termouprugom Ravnovesii Pri Martensitnykh Prevrashcheniyakh", *Doklady Akademii Nauk Sssr* **66**, 2, 211 (1949).

8. L. C. Chang, T. A. Read, "Plastic Deformation And Diffusionless Phase Changes In Metals - The Gold-Cadmium Beta-Phase", *Transactions Of The American Institute Of Mining And Metallurgical Engineers* **191**, 1, 47 (1951).

9. Y. Q. Fu, H. J. Du, W. M. Huang, S. Zhang, M. Hu, "TiNi-based thin films in MEMS applications: a review", *Sensors and Actuators a-Physical* **112**, 2-3, 395 (2004).

10. M. I. Frecker, "Recent advances in optimization of smart structures and actuators",

Journal of Intelligent Material Systems and Structures **14**, 4-5, 207 (2003).

11. C. Mavroidis, "Development of advanced actuators using shape memory alloys and electrorheological fluids", *Research in Nondestructive Evaluation* **14**, 1, 1 (2002).

12. Y. Luo, M. Salvia, "SMA actuators in medical applications", *Annales De Chimie-Science Des Materiaux* **29**, 6, 33 (2004).

13. N. B. Morgan, "Medical shape memory alloy applications - the market and its products", *Materials Science and Engineering a-Structural Materials Properties Microstructure and Processing* **378**, 1-2, 16 (2004).

14. L. G. Machado, M. A. Savi, "Medical applications of shape memory alloys", *Brazilian Journal of Medical and Biological Research* **36**, 6, 683 (2003).

15. A. R. Pelton, S. M. Russell, J. DiCello, "The physical metallurgy of Nitinol for medical applications", *Jom-Journal of the Minerals Metals & Materials Society* **55**, 5, 33 (2003).

16. S. A. Shabalovskaya, "Surface, corrosion and biocompatibility aspects of Nitinol as an implant material", *Bio-Medical Materials and Engineering* **12**, 1, 69 (2002).

17. F. J. Gil, J. A. Planell, "Shape memory alloys for medical applications", *Proceedings of the Institution of Mechanical Engineers Part H-Journal of Engineering in Medicine* **212**, H6, 473 (1998).

18. S. A. Shabalovskaya, "On the nature of the biocompatibility and on medical applications of NiTi shape memory and superelastic alloys", *Bio-Medical Materials and Engineering* **6**, 4, 267 (1996).

19. B. P. Philip TV, *Trans AIME* **209**, 1269 (1958).

20. K. Otsuka, T. Sawamura, K. Shimizu, "Crystal Structure and Internal Defects of Equiatomic Tini Martensite", *Physica Status Solidi a-Applied Research* **5**, 2, 457 (1971).

21. G. M. Michal, R. Sinclair, "The Structure of Tini Martensite", *Acta Crystallographica Section B-Structural Science* **37**, Oct, 1803 (1981).

22. Y. Kudoh, M. Tokonami, S. Miyazaki, K. Otsuka, "Crystal-Structure of the Martensite in Ti-49.2 at-Percent-Ni Alloy Analyzed by the Single-Crystal X-Ray-Diffraction Method", *Acta Metallurgica* **33**, 11, 2049 (1985).

23. V. N. Khachin, Y. I. Paskal, V. E. Gunter, A. A. Monasevich, V. P. Sivokha, "Structure Transformation, Physical-Properties and Memory Effects in Titanium Nickelide and Its Alloys", *Fizika Metallov I Metallovedenie* **46**, 3, 511 (1978).

24. M. B. Salamon, M. E. Meichle, C. M. Wayman, "Premartensitic Phases of Ti50Ni47Fe3", *Physical Review B* **31**, 11, 7306 (1985).

25. T. Tadaki, C. M. Wayman, "Electron-Microscopy Studies of Martensitic Transformations in Ti50Ni50-Xcux Alloys.1. Compositional Dependence of 1/3 Reflections from the Matrix Phase", *Metallography* **15**, 3, 233 (1982).

26. T. Tadaki, C. M. Wayman, "Electron-Microscopy Studies of Martensitic Transformations in Ti50Ni50-Xcux Alloys.2. Morphology and Crystal-Structure of Martensites", *Metallography* **15**, 3, 247 (1982).

27. T. H. Nam, T. Saburi, Y. Kawamura, K. Shimizu, "Shape Memory Characteristics Associated with the B2-Reversible-B19 and B19-Reversible-B19' Transformations in a Ti-40Ni-10Cu (at-Percent) Alloy", *Materials Transactions Jim* **31**, 4, 262 (1990).

28. M. Nishida, C. M. Wayman, T. Honma, "Precipitation Processes in near-Equiatomic Tini Shape Memory Alloys", *Metallurgical Transactions a-Physical Metallurgy and Materials Science* **17**, 9, 1505 (1986).

29. K. Otsuka, K. Shimizu, "Memory Effect and Thermoelastic Martensite Transformation in Cu-Al-Ni Alloy", *Scripta Metallurgica* **4**, 6, 469 (1970).

30. J. W. Christian, "*The theory of transformations in metals and alloys*" (Pergamon Press, Oxford, 1965)

31. D. S. Lieberman, M. S. Wechsler, T. A. Read, "Cubic To Orthorhombic Diffusionless Phase Change - Experimental And Theoretical Studies Of Aucd", *Journal of Applied Physics* **26**, 4, 473 (1955).

32. M. S. Wechsler, D. S. Lieberman, T. A. Read, "On The Theory Of The Formation Of Martensite", *Transactions Of The American Institute Of Mining And Metallurgical Engineers* **197**, 11, 1503 (1953).

33. T. Saburi, C. M. Wayman, "Crystallographic Similarities In Shape Memory Martensites", *Acta Metallurgica* **27**, 6, 979 (1979).

34. W. J. Tang, "Thermodynamic study of the low-temperature phase B19' and the martensitic transformation in near-equiatomic Ti-Ni shape memory alloys", *Metallurgical and Materials Transactions a-Physical Metallurgy and Materials Science* **28**, 3, 537 (1997).

35. H. S. Wu, Q. C. Tian, "The superelasticity of TiPdNi high temperature shape memory alloy", *Intermetallics* **11**, 8, 773 (2003).

36. T. Inamura *et al.*, "Martensitic transformation behavior and shape memory properties of Ti-Ni-Pt melt spun ribbon", *Journal of the Japan Institute of Metals* **69**, 8, 628 (2005).

37. S. F. Hsieh, S. K. Wu, "A study on ternary Ti-rich TiNiZr shape memory alloys", *Materials Characterization* **41**, 4, 151 (1998).

38. P. Olier, J. C. Brachet, J. L. Bechade, C. Foucher, G. Guenin, "Investigation of transformation temperatures, microstructure and shape memory properties of NiTi, NiTiZr and NiTiHf alloys", *Journal De Physique Iv* **5**, C8, 741 (1995).

39. X. L. Meng, Y. Wu, W. Cai, L. C. Zhao, "Two-way shape memory effect and its stability in Ti-Ni-Hf high temperature shape memory alloy", *Transactions of Nonferrous Metals Society of China* **15**, 2, 340 (2005).

40. L. W. Chang, D. S. Grummon, "Phase transformations in sputtered thin films of Ti-x(Ni,Cu)(1-x).2. Displacive transformations", *Philosophical Magazine*

a-Physics of Condensed Matter Structure Defects and Mechanical Properties **76**, 1, 191 (1997).

41. X. D. Han *et al.*, "The martensite structure and aging precipitates of a TiNiHf high temperature shape memory alloy", *Journal De Physique Iv* **5**, C8, 753 (1995).

42. L. W. Chang, D. S. Grummon, "Structure evolution in sputtered thin films of Ti-x(Ni,Cu)(1-x).1. Diffusive transformations", *Philosophical Magazine a-Physics of Condensed Matter Structure Defects and Mechanical Properties* **76**, 1, 163 (1997).

43. J. S. Zhang, W. Cai, X. B. Ren, K. Otsuka, M. Asai, "The nature of reversible change in M-s temperatures of Ti-Ni alloys with alternating aging", *Materials Transactions Jim* **40**, 12, 1367 (1999).

44. T. Fukuda, T. Saburi, T. Kakeshita, M. Kitayama, "Shape memory behavior of Ti-40.5Ni-10Cu alloy affected by C11(b)-type precipitates", *Materials Transactions Jim* **38**, 2, 107 (1997).

45. T. Fukuda, M. Kitayama, T. Kakeshita, T. Saburi, "Martensitic transformation behavior of a shape memory Ti-40.5Ni-10Cu alloy affected by the C11(b)-type precipitates", *Materials Transactions Jim* **37**, 10, 1540 (1996).

46. H. C. Lin, S. K. Wu, J. C. Lin, "The Martensitic-Transformation in Ti-Rich Tini Shape-Memory Alloys", *Materials Chemistry and Physics* **37**, 2, 184 (1994).

47. H. D. Gu *et al.*, "Growth of TiNiHf shape memory alloy thin films by laser ablation of composite targets", *Applied Surface Science* **129**, 579 (1998).

48. A. Ishida, A. Takei, S. Miyazaki, "Shape-Memory Thin-Film of Ti-Ni Formed by Sputtering", *Thin Solid Films* **228**, 1-2, 210 (1993).

49. J. A. Walker, K. J. Gabriel, M. Mehregany, "Thin-Film Processing of Tini Shape Memory Alloy", *Sensors and Actuators a-Physical* **21**, 1-3, 243 (1990).

50. D. S. Grummon, L. Hou, Z. Zhao, T. J. Pence, "Progress on sputter-deposited thermotractive titanium-nickel films", *Journal De Physique Iv* **5**, C8, 665 (1995).

51. S. Miyazaki, A. Ishida, "Martensitic transformation and shape memory behavior in sputter-deposited TiNi-base thin films", *Materials Science and Engineering a-Structural Materials Properties Microstructure and Processing* **275**, 106 (1999).

52. L. Hou, D. S. Grummon, "Transformational Superelasticity in Sputtered Titanium-Nickel Thin-Films", *Scripta Metallurgica Et Materialia* **33**, 6, 989 (1995).

53. Y. H. Li *et al.*, "Grain size and its distribution in NiTi thin films sputter-deposited on heated substrates", *Chinese Physics* **13**, 8, 1315 (2004).

54. P. Wollants, J. R. Roos, L. Delaey, "Thermally-Induced and Stress-Induced Thermoelastic Martensitic Transformations in the Reference Frame of Equilibrium Thermodynamics", *Progress in Materials Science* **37**, 3, 227 (1993).

55. P. Wollants, M. Debonte, L. Delaey, J. R. Roos, "Thermodynamic Analysis of the Work Performance of a Martensitic-Transformation under Stressed Conditions.2. Numerical-Analysis", *Zeitschrift Fur Metallkunde* **70**, 5, 298 (1979).

56. P. Wollants, M. Debonte, L. Delaey, J. R. Roos, "Thermodynamic Analysis of the Work Performance of a Martensitic-Transformation under Stressed Conditions.1. Theoretical Considerations", *Zeitschrift Fur Metallkunde* **70**, 3, 146 (1979).

57. T. M. Adams, S. R. Kirkpatrick, Z. Wang, A. Siahmakoun, "NiTi shape memory alloy thin films deposited by co-evaporation", *Materials Letters* **59**, 10, 1161 (2005).

58. D. S. Grummon, J. P. Zhang, "Stress in sputtered films of near-equiatomic TiNiX on (100) Si: Intrinsic and extrinsic stresses and their modification by thermally activated mechanisms", *Physica Status Solidi a-Applied Research* **186**, 1, 17 (2001).

59. D. S. Grummon, "Fabrication, microstructure and stress effects in sputtered TiNi thin films", *Shape Memory Materials* **327-3**, 295 (2000).

60. D. S. Grummon, J. P. Zhang, T. J. Pence, "Relaxation and recovery of extrinsic stress in sputtered titanium-nickel thin films on (100)-Si", *Materials Science and Engineering a-Structural Materials Properties Microstructure and Processing* **275**, 722 (1999).

61. R. X. Wang, Y. Zohar, M. Wong, "Residual stress-loaded titanium-nickel shape-memory alloy thin-film micro-actuators", *Journal of Micromechanics and Microengineering* **12**, 3, 323 (2002).

62. Y. Q. Fu, H. J. Du, "Relaxation and recovery of stress during martensite transformation for sputtered shape memory TiNi film", *Surface & Coatings Technology* **153**, 1, 100 (2002).

63. R. W. Hoffman, "*The Use of Thin Films in Physical Investigations*" (Academic Press, New York, 1966)

64. M. Ohring, "*Materials Science of Thin Films*" (Academic Press, New York, 1992)

65. A. P. Lee *et al.*, "A practical microgripper by fine alignment, eutectic bonding and SMA actuation", *Sensors and Actuators a-Physical* **54**, 1-3, 755 (1996).

66. S. A. Mathews, M. Wuttig, Q. M. Su, "The effect of substrate constraint on the martensitic transformation of Ni-Ti thin films", *Metallurgical and Materials Transactions a-Physical Metallurgy and Materials Science* **27**, 9, 2859 (1996).

67. K. Otsuka, C. M. Wayman, K. Nakai, H. Sakamoto, K. Shimizu, "Superelasticity Effects And Stress-Induced Martensitic Transformations In Cu-Al-Ni Alloys", *Acta Metallurgica* **24**, 3, 207 (1976).

68. S. Miyazaki, K. Otsuka, Y. Suzuki, "Transformation Pseudo-Elasticity And Deformation-Behavior In A Ti-50.6at-Percent Ni-Alloy", *Scripta Metallurgica* **15**, 3, 287 (1981).

69. H. C. Ling, R. Kaplow, "Stress-Induced Shape Changes And Shape Memory In The R And Martensite Transformations In Equiatomic Niti", *Metallurgical Transactions a-Physical Metallurgy and Materials Science* **12**, 12, 2101 (1981).

70. H. C. Ling, R. Kaplow, "Phase-Transitions And Shape Memory In Niti", *Metallurgical Transactions a-Physical Metallurgy and Materials Science* **11**, 1, 77 (1980).

71. S. Miyazaki, K. Otsuka, "Mechanical-Behavior Associated With The Premartensitic Rhombohedral-Phase Transition In A Ti50ni47fe3 Alloy", *Philosophical Magazine a-Physics of Condensed Matter Structure Defects and Mechanical Properties* **50**, 3, 393 (1984).

72. S. Miyazaki, S. Kimura, K. Otsuka, "Shape-Memory Effect And Pseudoelasticity Associated With The R-Phase Transition In Ti-50.5 At-Percent-Ni Single-Crystals", *Philosophical Magazine a-Physics of Condensed Matter Structure Defects and Mechanical Properties* **57**, 3, 467 (1988).

73. T. H. Nam, T. Saburi, K. Shimizu, "Cu-Content Dependence Of Shape Memory Characteristics In Ti-Ni-Cu Alloys", *Materials Transactions Jim* **31**, 11, 959 (1990).

74. T. Hashinaga, S. Miyazaki, T. Ueki, H. Horikawa, "Transformation and deformation behavior in sputter-deposited Ti-Ni-Cu thin films", *Journal De Physique Iv* **5**, C8, 689 (1995).

75. H. Sehitoglu *et al.*, "Detwinning in NiTi alloys", *Metallurgical and Materials Transactions a-Physical Metallurgy and Materials Science* **34**, 1, 5 (2003).

76. K. Gall *et al.*, "On the mechanical behavior of single crystal NiTi shape memory alloys and related polycrystalline phenomenon", *Materials Science and Engineering a-Structural Materials Properties Microstructure and Processing* **317**, 1-2, 85 (2001).

77. K. Gall, H. Sehitoglu, Y. I. Chumlyakov, I. V. Kireeva, "Tension-compression asymmetry of the stress-strain response in aged single crystal and polycrystalline NiTi", *Acta Materialia* **47**, 4, 1203 (1999).

78. Y. Liu, Z. Xie, J. Van Humbeeck, L. Delaey, "Some results on the detwinning process in NiTi shape memory alloys", *Scripta Materialia* **41**, 12, 1273 (1999).

79. X. P. Jiang *et al.*, "In situ observation of stress-induced martensitic transformation and plastic deformation in TiNi alloy", *Materials Science and Engineering a-Structural Materials Properties Microstructure and Processing* **238**, 2, 303 (1997).

80. H. Sehitoglu *et al.*, "Compressive response of NiTi single crystals", *Acta Materialia* **48**, 13, 3311 (2000).

81. K. Gall, H. Sehitoglu, "The role of texture in tension-compression asymmetry in polycrystalline NiTi", *International Journal of Plasticity* **15**, 1, 69 (1999).

82. L. Orgeas, D. Favier, "Stress-induced martensitic transformation of a NiTi alloy in isothermal shear, tension and compression", *Acta Materialia* **46**, 15, 5579 (1998).

83. J. A. Shaw, S. Kyriakides, "Initiation and propagation of localized deformation in elasto-plastic strips under uniaxial tension", *International Journal of Plasticity* **13**, 10, 837 (1997).

84. S. Miyazaki, T. Imai, Y. Igo, K. Otsuka, "Effect Of Cyclic Deformation On The Pseudoelasticity Characteristics Of Ti-Ni Alloys", *Metallurgical Transactions a-Physical Metallurgy and Materials Science* **17**, 1, 115 (1986).

85. F. E. Wang, W. J. Buehler, S. J. Pickart, "Crystal Structure and a Unique Martensitic Transition of Tini", *Journal of Applied Physics* **36**, 10, 3232 (1965).

86. A. Nagasawa, K. Enami, Y. Ishino, Y. Abe, S. Nenno, "Reversible Shape Memory Effect", *Scripta Metallurgica* **8**, 9, 1055 (1974).

87. Z. G. Wang *et al.*, "Two-way shape memory effect of TiNi alloy coil extension springs", *Materials Science and Engineering a-Structural Materials Properties Microstructure and Processing* **360**, 1-2, 126 (2003).

88. A. Isalgue, F. C. Lovey, M. Sade, "Oriented Growth Of Gamma Precipitates And Twsme In Cu-Zn-Al", *Scripta Metallurgica Et Materialia* **28**, 10, 1183 (1993).

89. X. M. Zhang, J. Fernandez, J. M. Guilemany, "Origin of two way shape memory effect in Cu-based shape memory alloys", *Journal De Physique Iv* **112**, 487 (2003).

90. T. Fukuda, M. Takahata, T. Kakeshita, T. Saburi, "Two-way shape memory properties of a Ti-51Ni single crystal including Ti3Ni4 precipitates of a single variant", *Materials Transactions Jim* **42**, 2, 323 (2001).

91. C. Y. Chang, D. Vokoun, C. T. Hu, "Two-way shape memory effect of NiTi alloy induced by constraint aging treatment at room temperature", *Metallurgical And Materials Transactions A-Physical Metallurgy And Materials Science* **32**, 7, 1629 (2001).

92. R. Stalmans, J. Van Humbeeck, L. Delaey, "Thermomechanical Cycling, 2 Way Memory and Concomitant Effects in Cu-Zn-Al Alloys", *Acta Metallurgica Et Materialia* **40**, 3, 501 (1992).

93. W. Siegert, M. Mertmann, K. Neuking, G. Eggeler, "Influence of thermomechanical treatment on a NiTiNb shape memory alloy for coupling devices", *Materialwissenschaft Und Werkstofftechnik* **31**, 9, 822 (2000).

94. H. W. Kim, "A study of the two-way shape memory effect in Cu-Zn-Al alloys by the thermomechanical cycling method", *Journal of Materials Processing Technology* **146**, 3, 326 (2004).

95. J. M. Guilemany, J. Fernandez, "Mechanism of 2-Way Shape-Memory Effect Obtained by Stabilized Stress-Induced Martensite", *Journal De Physique Iv* **5**, C2, 355 (1995).

96. J. Pons, M. Masse, R. Portier, "Thermomechanical cycling and two-way memory effect induced in Cu-Zn-Al", *Materials Science and Engineering A* **273-275**, 610 (1999).

97. P. Y. Manach, D. Favier, "Origin Of The 2-Way Memory Effect In Niti Shape-Memory Alloys", *Scripta Metallurgica Et Materialia* **28**, 11, 1417 (1993).

98. X. L. Meng, Y. F. Zheng, W. Cai, L. C. Zhao, "Two-way shape memory effect of a TiNiHf high temperature shape memory alloy", *Journal of Alloys and Compounds* **372**, 1-2, 180 (2004).

99. T. Omori, Y. Sutou, J. J. Wang, R. Kainuma, K. Ishida, "Effect of microstructure on two-way shape memory effect in Cu-Al-Mn alloys", *Journal De Physique Iv* **112**, 507 (2003).

100. R. Lahoz, L. Gracia-Villa, J. A. Puertolas, "Training of the two-way shape memory effect by bending in NiTi alloys", *Journal of Engineering Materials and Technology-Transactions of the Asme* **124**, 4, 397 (2002).

101. H. Scherngell, A. C. Kneissl, "Generation, development and degradation of the intrinsic two-way shape memory effect in different alloy systems", *Acta Materialia* **50**, 2, 327 (2002).

102. Y. Liu, Y. Liu, J. Van Humbeeck, "Two-way shape memory effect developed by martensite deformation in NiTi", *Acta Materialia* **47**, 1, 199 (1998).

103. D. A. Miller, D. C. Lagoudas, "Influence of cold work and heat treatment on the shape memory effect and plastic strain development of NiTi", *Materials Science and Engineering a-Structural Materials Properties Microstructure and Processing* **308**, 1-2, 161 (2001).

104. X. B. Ren, K. Otsuka, "Universal symmetry property of point defects in crystals", *Physical Review Letters* **85**, 5, 1016 (2000).

105. P. Prader, A. C. Kneissl, "Deformation behaviour and two-way shape memory effect of NiTi alloys", *Zeitschrift Fur Metallkunde* **88**, 5, 410 (1997).

106. R. Stalmans, J. Van Humbeeck, L. Delaey, "The 2 Way Memory Effect in Copper-Based Shape Memory Alloys - Thermodynamics and Mechanisms", *Acta Metallurgica Et Materialia* **40**, 11, 2921 (1992).

107. H. Hertz, "*On the contact of rigid elastic solids and on hardness*". J. a. Schott, Ed., Miscellaneous Papers by H. Hertz (Macmillan, London, 1896)

108. K. L. Johnson, "*Contact mechanics*" (Cambridge University Press, New York, NY, 1985)pp. 174-176.

109. M. F. Doerner, W. D. Nix, "A method for interpreting the data from depth-sensing indentation instruments", *Journal of Materials Research* **1**, 4, 601 (1986).

110. W. C. Oliver, G. M. Pharr, "An Improved Technique For Determining Hardness And Elastic-Modulus Using Load And Displacement Sensing Indentation Experiments", *Journal of Materials Research* **7**, 6, 1564 (1992).

111. D. Tabor, "Indentation hardness: Fifty years on - A personal view", *Philosophical Magazine a-Physics of Condensed Matter Structure Defects and Mechanical Properties* **74**, 5, 1207 (1996).

112. D. Tabor, "A Simple Theory Of Static And Dynamic Hardness", *Proceedings Of The Royal Society Of London Series A-Mathematical And Physical Sciences* **192**, 1029, 247 (1948).

113. J. Mackerle, "Finite element modelling and simulation of indentation testing: a bibliography (1990-2002)", *Engineering Computations* **21**, 1, 23 (2004).

114. C. Hardy, G. V. Tordion, C. N. Baronet, "Indentation Of An Elastic-Perfectly-Plastic Half-Space By A Hard-Sphere", *Journal Of Basic Engineering* **94**, 1, 251 (1972).

115. G. B. Sinclair, P. S. Follansbee, K. L. Johnson, "Quasi-Static Normal Indentation Of An Elasto-Plastic Half-Space By A Rigid Sphere.2. Results", *International Journal of Solids and Structures* **21**, 8, 865 (1985).

116. W. Y. Ni, Y. T. Cheng, D. S. Grummon, "Microscopic shape memory and superelastic effects under complex loading conditions", *Surface & Coatings Technology* **177**, 512 (2004).

117. W. Y. Ni, Y. T. Cheng, D. S. Grummon, "Microscopic superelastic behavior of a nickel-titanium alloy under complex loading conditions", *Applied Physics Letters* **82**, 17, 2811 (2003).

118. K. Gall, K. Juntunen, H. J. Maier, H. Sehitoglu, Y. I. Chumlyakov, "Instrumented micro-indentation of NiTi shape-memory alloys", *Acta Materialia* **49**, 16, 3205 (2001).

119. K. Gall *et al.*, "Micro and macro deformation of single crystal NiTi", *Journal of Engineering Materials and Technology-Transactions of the Asme* **124**, 2, 238 (2002).

120. C. Liu, Q. P. Sun, Y. P. Zhao, T. X. Yu, "Depth dependence of nanohardness in a CuAlNi single crystal shape memory alloy", *International Journal of Nonlinear Sciences and Numerical Simulation* **3**, 3-4, 535 (2002).

121. C. Liu, Y. P. Zhao, T. X. Yu, "Measurement of microscopic deformation in a CuAlNi single crystal alloy by nanoindentation with a heating stage", *Materials & Design* **26**, 5, 465 (2005).

122. E. Rabinowicz, "The Least Wear", *Wear* **100**, 1-3, 533 (1984).

123. J. T. Burwell, C. D. Strang, "On The Empirical Law Of Adhesive Wear", *Journal of Applied Physics* **23**, 1, 18 (1952).

124. J. F. Archard, "Contact And Rubbing Of Flat Surfaces", *Journal of Applied Physics* **24**, 8, 981 (1953).

125. R. Liu, D. Y. Li, "Modification of Archard's equation by taking account of elastic/pseudoelastic properties of materials", *Wear* **250**, 956 (2001).

126. A. Leyland, A. Matthews, "On the significance of the H/E ratio in wear control: a nanocomposite coating approach to optimised tribological behaviour", *Wear* **246**, 1-2, 1 (2000).

127. E. Rabinowicz, "*Friction and Wear of Materials* " (Wiley-Interscience, New York,

ed. 2 nd, 1995)

128. *"Compilation of ASTM Standard Definitions"* (ASTM, Philadelphia, PA, 1994)

129. *"Standard Test Method for Wear Testing with a Pin-on-Disk Apparatus"*, Compilation of ASTM Standard Definitions (ASTM, Philadelphia, PA, 1994)

130. R. Jacobs *et al.*, "A certified reference material for the scratch test", *Surface & Coatings Technology* **174**, 1008 (2003).

131. N. I. Tymiak, A. Daugela, T. J. Wyrobek, O. L. Warren, "Highly localized acoustic emission monitoring of nanoscale indentation contacts", *Journal of Materials Research* **18**, 4, 784 (2003).

132. S. J. Bull, E. G. Berasetegui, "An overview of the potential of quantitative coating adhesion measurement by scratch", *Tribology International* **39**, 2, 99 (2006).

133. S. J. Bull, "Failure mode maps in the thin film scratch adhesion test", *Tribology International* **30**, 7, 491 (1997).

134. H. C. Lin, H. M. Liao, J. L. He, K. C. Chen, K. M. Lin, "Wear characteristics of TiNi shape memory alloys", *Metallurgical and Materials Transactions a-Physical Metallurgy and Materials Science* **28**, 9, 1871 (1997).

135. H. C. Lin, H. M. Liao, J. L. He, K. M. Lin, K. C. Chen, "Wear characteristics of ion-nitrided Ti50Ni50 shape memory alloys", *Surface & Coatings Technology* **92**, 3, 178 (1997).

136. Y. N. Liang, S. Z. Li, Y. B. Jin, W. Jin, S. Li, "Wear behavior of a TiNi alloy", *Wear* **198**, 1-2, 236 (1996).

137. D. Y. Li, "Wear behaviour of TiNi shape memory alloys", *Scripta Materialia* **34**, 2, 195 (1996).

138. J. Singh, A. T. Alpas, "Dry Sliding Wear Mechanisms In A Ti50ni47fe3

Intermetallic Alloy", *Wear* **181**, 302 (1995).

139. C. A. Zimmerly, O. T. Inal, R. H. Richman, "Explosive Welding Of A Near-Equiatomic Nickel-Titanium Alloy To Low-Carbon Steel", *Materials Science and Engineering a-Structural Materials Properties Microstructure and Processing* **188**, 1-2, 251 (1994).

140. P. Clayton, "Tribological Behavior Of A Titanium Nickel-Alloy", *Wear* **162**, 202 (1993).

141. R. H. Richman, A. S. Rao, D. E. Hodgson, "Cavitation Erosion Of 2 Niti Alloys", *Wear* **157**, 2, 401 (1992).

142. Y. Shida, Y. Sugimoto, "Water Jet Erosion Behavior Of Ti-Ni Binary-Alloys", *Wear* **146**, 2, 219 (1991).

143. F. T. Cheng, P. Shi, H. C. Man, "Cavitation erosion resistance of heat-treated NiTi", *Materials Science and Engineering a-Structural Materials Properties Microstructure and Processing* **339**, 1-2, 312 (2003).

144. L. M. Qian, X. D. Xiao, Q. P. Sun, T. X. Yu, "Anomalous relationship between hardness and wear properties of a superelastic nickel-titanium alloy", *Applied Physics Letters* **84**, 7, 1076 (2004).

145. J. Koskinen, E. Haimi, A. Mahiout, V. K. Lindroos, S. P. Hannula, "Superelastic NiTi coatings with good corrosive wear resistance", *Journal De Physique Iv* **112**, 1137 (2003).

146. I. M. Hutchings, "*Tribology Friction and Wear of Engineering Materials*" (Edward Arnold, London, 1992)

147. W. A. Glaeser, "*Materials for Tribology*" (Elsevier Science Publishers, Amsterdam, The Netherlands, 1992)

148. R. Liu, D. Y. Li, "Experimental studies on tribological properties of pseudoelastic TiNi alloy with comparison to stainless steel 304", *Metallurgical and Materials*

Transactions a-Physical Metallurgy and Materials Science **31**, 11, 2773 (2000).

149. D. Y. Li, "Exploration of TiNi shape memory alloy for potential application in a new area: tribological engineering", *Smart Materials & Structures* **9**, 5, 717 (2000).

150. H. Z. Ye, R. Liu, D. Y. Li, R. Eadie, "Development of a new wear-resistant material: TiC/TiNi composite", *Scripta Materialia* **41**, 10, 1039 (1999).

151. S. PalDey, S. C. Deevi, "Single layer and multilayer wear resistant coatings of (Ti,Al)N: a review", *Materials Science and Engineering a-Structural Materials Properties Microstructure and Processing* **342**, 1-2, 58 (2003).

152. M. O. Vasil'yev, V. Y. Panarin, A. A. Tkachuk, "Titanium-nitride coatings deposited by the method of a vacuum electric arc (review)", *Metallofizika I Noveishie Tekhnologii* **22**, 11, 58 (2000).

153. L. Hultman *et al.*, "Review of the thermal and mechanical stability of TiN-based thin films", *Zeitschrift Fur Metallkunde* **90**, 10, 803 (1999).

154. Z. B. Zhao, Z. U. Rek, S. M. Yalisove, J. C. Bilello, "Phase formation and structure of magnetron sputtered chromium nitride films: in-situ and ex-situ studies", *Surface & Coatings Technology* **185**, 2-3, 329 (2004).

155. X. M. He *et al.*, "Structure, hardness, and tribological properties of reactive magnetron sputtered chromium nitride films", *Journal of Vacuum Science & Technology A* **18**, 1, 30 (2000).

156. M. Nordin, M. Larsson, S. Hogmark, "Mechanical and tribological properties of multilayered PVD TiN/CrN, TiN/MoN, TiN/NbN and TiN/TaN coatings on cemented carbide", *Surface & Coatings Technology* **106**, 2-3, 234 (1998).

157. M. Nordin, M. Larsson, S. Hogmark, "Mechanical and tribological properties of multilayered PVD TiN/CrN", *Wear* **232**, 2, 221 (1999).

158. P. Arneodo Larochette, M. Ahlers, "Grain-size dependence of the two-way shape

memory effect obtained by stabilisation in Cu-Zn-Al crystals", *Materials Science and Engineering A* **361**, 1-2, 249 (2003).

159. J. Robertson, "Diamond-like amorphous carbon", *Materials Science & Engineering R-Reports* **37**, 4-6, 129 (2002).

160. M. Wang, K. Schmidt, K. Reichelt, H. Dimigen, H. Hubsch, "The Properties of Titanium-Containing Amorphous Hydrogenated Carbon-Films", *Surface & Coatings Technology* **47**, 1-3, 691 (1991).

161. F. M. Kimock, B. J. Knapp, "Commercial Applications of Ion-Beam Deposited Diamond-Like Carbon (Dlc) Coatings", *Surface & Coatings Technology* **56**, 3, 273 (1993).

162. A. Grill, V. Patel, "Tribological Properties of Diamond-Like Carbon and Related Materials", *Diamond and Related Materials* **2**, 5-7, 597 (1993).

163. J. Koskinen *et al.*, "Microstructural changes in DLC films due to tribological contact", *Surface & Coatings Technology* **109**, 1-3, 385 (1998).

164. A. K. Gangopadhyay, P. A. Willermet, M. A. Tamor, W. C. Vassell, "Amorphous hydrogenated carbon films for tribological applications.1. Development of moisture insensitive films having reduced compressive stress", *Tribology International* **30**, 1, 9 (1997).

165. A. K. Gangopadhyay, P. A. Willermet, W. C. Vassell, M. A. Tamor, "Amorphous hydrogenated carbon films for tribological applications.2. Films deposited on aluminium alloys and steel", *Tribology International* **30**, 1, 19 (1997).

166. A. Haseeb, J. P. Celis, J. R. Roos, "An Electrochemical Deposition Process For The Synthesis Of Laminated Nanocomposites", *Materials And Manufacturing Processes* **10**, 4, 707 (1995).

167. J. P. Celis, K. Vanacker, K. Callewaert, P. Vanhoutte, "Residual-Stress Measurements In Electrolytic Copper-Nickel Compositionally Modulated Multilayers", *Journal Of The Electrochemical Society* **142**, 1, 70 (1995).

168. A. Haseeb, J. P. Celis, J. R. Roos, "Dual-Bath Electrodeposition Of Cu/Ni Compositionally Modulated Multilayers", *Journal Of The Electrochemical Society* **141**, 1, 230 (1994).

169. K. L. Lin, W. H. Chao, C. D. Wu, "The performance and degradation behaviours of the TiAlN/interlayer coatings on drills", *Surface & Coatings Technology* **89**, 3, 279 (1997).

170. A. Leyland *et al.*, "Tin And Crn Pvd Coatings On Electroless Nickel-Coated Steel Substrates", *Surface & Coatings Technology* **60**, 1-3, 474 (1993).

171. J. L. He, M. H. Hon, "Sliding Wear-Resistance Of Tool Steel Coated With Electroless Ni-P And Cathodic Arc Plasma Tin", *Surface & Coatings Technology* **53**, 1, 87 (1992).

172. J. L. He, M. H. Hon, "Corrosion Protection Of Tin-Coated Low-Carbon Steel With Electroless Ni-P As An Interlayer", *Surface & Coatings Technology* **53**, 1, 93 (1992).

173. J. Xu, W. J. Liu, Y. D. Kan, M. L. Zhong, "Microstructure and wear properties of laser cladding Ti-Al-Fe-B coatings on AA2024 aluminum alloy", *Materials & Design* **27**, 5, 405 (2006).

174. R. Murakami, Y. H. Kim, K. Kimura, D. Yonekura, D. H. Shin, "Evaluation of adhesive behaviors of chromium nitride coating films produced by arc ion plating method", *Jsme International Journal Series A-Solid Mechanics And Material Engineering* **49**, 1, 123 (2006).

175. T. H. Le, Y. H. Chae, S. S. Kim, "Sliding wear behavior of plasma sprayed zirconia coating on cast aluminum against silicon carbide ceramic", *Journal Of Materials Science & Technology* **21**, 5, 666 (2005).

176. T. B. Wei, F. Y. Yan, J. Tian, "Characterization and wear- and corrosion-resistance of microarc oxidation ceramic coatings on aluminum alloy", *Journal Of Alloys And Compounds* **389**, 1-2, 169 (2005).

177. J. X. Liao *et al.*, "The tribological properties of a gradient layer prepared by plasma-based ion implantation on 2024 aluminum alloy", *Surface & Coatings Technology* **183**, 2-3, 157 (2004).

178. I. A. Podchernyaeva, A. D. Panasyuk, V. V. Shchepetov, D. V. Yurechko, V. U. Gromenko, "Surface modification of AL9 alloy by electric-spark alloying with materials of the AlN-Ti(Zr)B-2-Ti(Zr)Si-2 system", *Powder Metallurgy And Metal Ceramics* **43**, 3-4, 156 (2004).

179. E. A. R. Perez, R. M. Souza, "Numerical and experimental analyses on the contact stresses developed during single and successive indentations of coated systems", *Surface & Coatings Technology* **188-89**, 572 (2004).

180. L. F. Xia, Z. H. Yan, J. X. Liao, "Effects of intermediate layers on the tribological behavior of DLC coated 2024 aluminum alloy", *Wear* **257**, 5-6, 599 (2004).

181. H. A. Samir, H. C. Qian, B. C. Xia, S. M. Wu, "Comments on process of duplex coatings on aluminum alloys", *Journal Of Central South University Of Technology* **11**, 3, 239 (2004).

182. S. Uozato, K. Nakata, M. Ushio, "Corrosion and wear behaviors of ferrous powder thermal spray coatings on aluminum alloy", *Surface & Coatings Technology* **169**, 691 (2003).

183. F. Zhou, C. M. Suh, S. S. Kim, R. Murakami, "Sliding-wear behavior of TiN- and CrN-coated 2024 aluminum alloy against an Al2O3 ball", *Tribology Letters* **13**, 3, 173 (2002).

184. F. Zhou, C. M. Suh, S. S. Kim, R. Murakami, "Tribological behavior of CrN coating on aluminum alloys deposited by arc ion plating", *Journal Of Materials Research* **17**, 12, 3133 (2002).

185. J. Tian, Z. Z. Luo, S. K. Qi, X. J. Sun, "Structure and antiwear behavior of micro-arc oxidized coatings on aluminum alloy", *Surface & Coatings Technology* **154**, 1, 1 (2002).

186. J. X. Liao, L. F. Xia, Y. Sun, "Study of the structure of AlN/DLC layer of aluminum alloy implanted by PBII", *Acta Metallurgica Sinica* **37**, 9, 922 (2001).

187. K. Nakata, M. Ushio, "Wear resistance of plasma sprayed Al-Si binary alloy coatings on A6063 Al alloy substrate", *Surface & Coatings Technology* **142**, 277 (2001).

188. R. M. Souza, A. Sinatora, G. G. W. Mustoe, J. J. Moore, "Numerical and experimental study of the circular cracks observed at the contact edges of the indentations of coated systems with soft substrates", *Wear* **251**, 1337 (2001).

189. P. H. Chong, H. C. Man, T. M. Yue, "Microstructure and wear properties of laser surface-cladded Mo-WC MMC on AA6061 aluminum alloy", *Surface & Coatings Technology* **145**, 1-3, 51 (2001).

190. Y. Miki, T. Taniguchi, T. Hanabusa, K. Kusaka, T. Matsue, "X-ray stress measurement and mechanical properties of TiN films coated on aluminum and aluminum alloy substrates by arc ion plating and ion beam mixing", *Materials Science Research International* **6**, 4, 243 (2000).

191. S. K. Kim, T. H. Kim, J. Wohle, K. T. Rie, "TiCN coatings on aluminum alloy formed by MO-PACVD", *Surface & Coatings Technology* **131**, 1-3, 121 (2000).

192. Y. H. Chae, S. S. Kim, "Sliding wear behavior of ceramic, plasma sprayed on casting aluminum alloy against SiC ball", *Tribology Letters* **8**, 1, 35 (2000).

193. G. Y. Liang, T. T. Wong, J. Y. Su, C. H. Woo, "Amorphous structure in a laser clad Ni-Cr-Al coating on Al-Si alloy", *Transactions Of Nonferrous Metals Society Of China* **10**, 2, 220 (2000).

194. M. L. Kuruppu, G. Negrea, I. P. Ivanov, S. L. Rohde, "Monolithic and multilayer Cr/CrN, Cr/Cr2N, and Cr2N/CrN coatings on hard and soft substrates", *Journal Of Vacuum Science & Technology A-Vacuum Surfaces And Films* **16**, 3, 1949 (1998).

195. B. L. Cain, W. J. Croisant, "Electrical contact resistance of titanium nitride

coatings for electromagnetic shielding applications", *Surface & Coatings Technology* **82**, 1-2, 83 (1996).

196. J. Senf, E. Broszeit, "Wear and corrosion protection using Cr and CrN (PVD coating on Al and Mg)", *Materialwissenschaft Und Werkstofftechnik* **30**, 5, 262 (1999).

197. L. S. Zheng, S. Ramalingam, "Multi-layer and composite structures for advanced coatings", *Surface & Coatings Technology* **81**, 1, 52 (1996).

198. S. Ramalingam, L. S. Zheng, "Film-Substrate Interface Stresses And Their Role In The Tribological Performance Of Surface-Coatings", *Tribology International* **28**, 3, 145 (1995).

199. K. Tanaka, S. Nagaki, "A Thermomechanical Description of Materials with Internal Variables in the Process of Phase-Transitions", *Ingenieur Archiv* **51**, 5, 287 (1982).

200. C. Liang, C. A. Rogers, "One-dimensional thermomechanical constitutive relations for shape memory materials (Reprinted from Journal of Intelligent Material Systems and Structures, vol 1, pg 207-234, 1990)", *Journal of Intelligent Material Systems and Structures* **8**, 4, 285 (1997).

201. Y. Ivshin, T. J. Pence, "A Constitutive Model for Hysteretic Phase-Transition Behavior", *International Journal of Engineering Science* **32**, 4, 681 (1994).

202. Y. Ivshin, T. J. Pence, "A Thermomechanical Model for a One Variant Shape-Memory Material", *Journal of Intelligent Material Systems and Structures* **5**, 4, 455 (1994).

203. Y. W. Chi, T. J. Pence, H. Y. Tsai, "Axisymmetric plane stress states of an annulus subject to displacive shear transformation", *Journal of Applied Mechanics-Transactions of the Asme* **72**, 1, 44 (2005).

204. L. C. Brinson, M. S. Huang, "Simplifications and comparisons of shape memory alloy constitutive models", *Journal of Intelligent Material Systems and Structures*

7, 1, 108 (1996).

205. J. G. Boyd, D. C. Lagoudas, "A thermodynamical constitute model for shape memory materials.1. The monolithic shape memory alloy", *International Journal of Plasticity* **12**, 6, 805 (1996).

206. J. G. Boyd, D. C. Lagoudas, "A thermodynamical constitutive model for shape memory materials.2. The SMA composite material", *International Journal of Plasticity* **12**, 7, 843 (1996).

207. Q. P. Sun, K. C. Hwang, "Micromechanics Modeling for the Constitutive Behavior of Polycrystalline Shape Memory Alloys.1. Derivation of General Relations", *Journal of the Mechanics and Physics of Solids* **41**, 1, 1 (1993).

208. Q. P. Sun, K. C. Hwang, "Micromechanics Modeling for the Constitutive Behavior of Polycrystalline Shape Memory Alloys.2. Study of the Individual Phenomena", *Journal of the Mechanics and Physics of Solids* **41**, 1, 19 (1993).

209. E. Patoor, M. O. Bensalah, A. Eberhardt, M. Berveiller, "Thermomechanical Behavior Determining of Shape-Memory Alloys Using a Thermodynamical Potential Optimizing", *Revue De Metallurgie-Cahiers D Informations Techniques* **90**, 12, 1587 (1993).

210. M. Huang, L. C. Brinson, "Multivariant model for single crystal shape memory alloy behavior", *Journal of the Mechanics and Physics of Solids* **46**, 8, 1379 (1998).

211. B. C. Goo, C. Lexcellent, "Micromechanics-based modeling of two-way memory effect of a single crystalline shape-memory alloy", *Acta Materialia* **45**, 2, 727 (1997).

212. F. Auricchio, L. Petrini, "A three-dimensional model describing stress-temperature induced solid phase transformations: solution algorithm and boundary value problems", *International Journal for Numerical Methods in Engineering* **61**, 6, 807 (2004).

213. F. Auricchio, U. Stefanelli, "Numerical analysis of a three-dimensional super-elastic constitutive model", *International Journal for Numerical Methods in Engineering* **61**, 1, 142 (2004).

214. D. C. Lagoudas, P. B. Entchev, "Modeling of transformation-induced plasticity and its effect on the behavior of porous shape memory alloys. Part I: constitutive model for fully dense SMAs", *Mechanics of Materials* **36**, 9, 865 (2004).

215. Y. H. Wang, D. N. Fang, "A three-dimensional constitutive model for shape memory alloys", *International Journal of Nonlinear Sciences and Numerical Simulation* **4**, 1, 81 (2003).

216. M. Brocca, L. C. Brinson, Z. Bazant, "Three-dimensional constitutive model for shape memory alloys based on microplane model", *Journal of the Mechanics and Physics of Solids* **50**, 5, 1051 (2002).

217. J. Lubliner, F. Auricchio, "Generalized plasticity and shape-memory alloys", *International Journal of Solids and Structures* **33**, 7, 991 (1996).

218. W. Y. Ni, Ph.D Dissertation, Michigan State University (2003).

219. Z. B. Zhao, Master Thesis, Michigan State University (2000).

220. A. C. o. Terminology, "*Compilation of ASTM Standard Definitions*" (ASTM, Philadelphia, PA, 1994)

221. T. Kakeshita *et al.*, "Effect Of Hydrostatic Pressures On Thermoelastic Martensitic Transformations In Aged Ti-Ni And Ausaged Fe-Ni-Co-Ti Shape Memory Alloys", *Materials Transactions Jim* **33**, 1, 1 (1992).

222. Y. J. Zhang, Y. T. Cheng, D. S. Grummon, "Indentation stress dependence of the temperature range of microscopic superelastic behavior of nickel-titanium thin films", *Journal of Applied Physics* **98**, 3, (2005).

223. M. Gelfi, G. M. La Vecchia, N. Lecis, S. Troglio, "Relationship between through-thickness residual stress of CrN-PVD coatings and fatigue nucleation

sites", *Surface & Coatings Technology* **192**, 2-3, 263 (2005).

224. W. J. Chou, G. P. Yu, J. H. Huang, "Mechanical properties of TiN thin film coatings on 304 stainless steel substrates", *Surface & Coatings Technology* **149**, 1, 7 (2002).

225. T. W. Kim, S. W. Park, in *Fracture And Strength Of Solids, Pts 1 And 2.* (2000), vol. 183-1, pp. 1279-1284.

226. U. Pettersson, S. Jacobson, "Influence of surface texture on boundary lubricated sliding contacts", *Tribology International* **36**, 11, 857 (2003).

227. G. Ryk, Y. Kligerman, I. Etsion, "Experimental investigation of laser surface texturing for reciprocating automotive components", *Tribology Transactions* **45**, 4, 444 (2002).

228. I. Etsion, G. Halperin, "A laser surface textured hydrostatic mechanical seal", *Tribology Transactions* **45**, 3, 430 (2002).

229. A. Ronen, I. Etsion, Y. Kligerman, "Friction-reducing surface-texturing in reciprocating automotive components", *Tribology Transactions* **44**, 3, 359 (2001).

230. P. Baumgart, D. J. Krajnovich, T. A. Nguyen, A. C. Tam, "A New Laser Texturing Technique For High-Performance Magnetic Disk Drives", *Ieee Transactions On Magnetics* **31**, 6, 2946 (1995).

231. W. Y. Ni, Y. T. Cheng, D. S. Grummon, "Recovery of microindents in a nickel-titanium shape-memory alloy: A "self-healing" effect", *Applied Physics Letters* **80**, 18, 3310 (2002).

232. L. E. Samuels, T. O. Mulhearn, "An Experimental Investigation of the Deformed Zone Associated with Indentation Hardness Impressions", *Journal of the Mechanics and Physics of Solids* **5**, 2, 125 (1957).

233. J. G. Swadener, E. P. George, G. M. Pharr, "The correlation of the indentation size effect measured with indenters of various shapes", *Journal of the Mechanics*

and Physics of Solids **50**, 4, 681 (2002).

234. W. D. Nix, H. J. Gao, "Indentation size effects in crystalline materials: A law for strain gradient plasticity", *Journal of the Mechanics and Physics of Solids* **46**, 3, 411 (1998).

235. R. F. Hehemann, G. D. Sandrock, "Relations between Premartensitic Instability and Martensite Structure in Tini", *Scripta Metallurgica* **5**, 9, 801 (1971).

236. M. Nishida, C. M. Wayman, R. Kainuma, T. Honma, "Further Electron-Microscopy Studies of the Ti11Ni14 Phase in an Aged Ti-52at-Percent-Ni Shape Memory Alloy", *Scripta Metallurgica* **20**, 6, 899 (1986).

237. T. Saburi, S. Nenno, T. Fukuda, "Crystal-Structure and Morphology of the Metastable X-Phase in Shape Memory Ti-Ni Alloys", *Journal of the Less-Common Metals* **125**, 157 (1986).

238. T. Hara, T. Ohba, K. Otsuka, M. Nishida, "Phase transformation and crystal structures of Ti2Ni3 precipitates in Ti-Ni alloys", *Materials Transactions Jim* **38**, 4, 277 (1997).

239. A. Taylor, R. W. Floyd, "Precision Measurements of Lattice Parameters of Non-Cubic Crystals", *Acta Crystallographica* **3**, 4, 285 (1950).

240. M. H. Mueller, H. W. Knott, "Crystal Structures of Ti2Cu, Ti2Ni, Ti4Ni2O, and Ti4Cu2O", *Transactions of the Metallurgical Society of Aime* **227**, 3, 674 (1963).

241. O. H. Massalski TB, et al., "Binary Alloy Phase Diagrams", *Binary Alloy Phase Diagrams, ASM Internaltional* **3**, (1990).

242. K. Otsuka, T. Kakeshita, "Science and technology of shape-memory alloys. New developments", *Mrs Bulletin* **27**, 2, 91 (2002).

243. S. Miyazaki *et al.*, "Shape Memory Effect And Pseudoelasticity In A Ti-Ni Single-Crystal", *Scripta Metallurgica* **17**, 9, 1057 (1983).

244. S. Miyazaki, Y. Ohmi, K. Otsuka, Y. Suzuki, "Characteristics Of Deformation And Transformation Pseudoelasticity In Ti-Ni Alloys", *Journal De Physique* **43**, NC-4, 255 (1982).

245. K. Otsuka, X. Ren, "Physical metallurgy of Ti-Ni-based shape memory alloys", *Progress in Materials Science* **50**, 5, 511 (2005).

246. *"Surface Texture, Surface Roughness, Waviness and Lay:ASME B46.1-2002"* (ASME, 2003)